Development and testing of quasi-optical devices for Photon Orbital Angular Momentum manipulation at millimetre wavelengths

A thesis submitted to The University of Manchester for the degree of
Doctor of Philosophy
Faculty of Engineering and Physical Sciences

2014

Stefania Maccalli
School of Physics and Astronomy

Contents

List of Tables

List of Figures

Development and testing of quasi-optical devices for photon orbital angular momentum manipulation at millimetre wavelengths

A thesis submitted for the degree of Doctor of Philosophy,
The University of Manchester, Faculty of Engineering and Physical Sciences

Stefania Maccalli
School of Physics and Astronomy, 21 March 2014

Abstract

It is well known that light can carry two different kind of angular momentum that together form the *total angular momentum* of photons. These two forms are the *spin orbital angular momentum*, associated with the circular polarisation of light, and the *orbital angular momentum of light* associated with a wavefront tilted with respect to the propagation axis. Any tilted wavefront generates an orbital component of the angular momentum but there are some special cases in which this property becomes particularly interesting. It is the case of *optical vortices* which form when the waveform is continuously and uniformly tilted to the propagation axis forming a spiral structure. It was found that such structured wavefronts have the characteristics that the cumulative phase change on a closed circle around the propagation axis is always a multiple l of 2π. Moreover, it was found that each photon carries a quantised orbital angular momentum $l\hbar$. Optical vortices are also identified by an annular structure of the intensity pattern which scales with the l value. All these peculiarities represent a huge potential in many research fields as the phase and intensity characteristics can improve the performance of coronagraphs, encryption protocols, optical tweezers to name the most important. Most of the research has been focused on optical frequencies but the field of radio vortices seems to be promising both for the telecommunications applications and for potential astronomical observations. This thesis summarises the work that has been done toward the development and testing of devices for the manipulation of light's orbital angular momentum at millimetre wavelengths, specifically at 100 GHz. A mode |2| *q-plate* was tested and four *spiral phase plates* were designed, manufactured and tested. Specifically a mode |1| smooth surface plate, a mode |1| and mode |2| wedges plates and a mode |2| wedges plate with a symmetrical split ramp. The main testing techniques used are beam cuts measurements and 2D and 3D near field scans performed in the RF lab of the JBCA department at the University of Manchester. All the results are reported in this thesis and constitute the first stage of a bigger project for the development of radio orbital angular momentum technologies for telecommunications and astronomy. All the images in this thesis, unless differently stated, are originally made by the author.

Declaration

No portion of the work referred to in this dissertation has been submitted in support of an application for another degree or qualification of this or any other university or other institute of learning.

Copyright

To You, to my family and to those who work for the pursuit of knowledge.

Acknowledgements

The moment has finally arrived. It is time to say thanks. These last four years have been incredibly intense and meaningful and the list of people that contributed to making this experience amazing is long. I'll try to express my gratitude the best way on this page, but there is much more than this.

The first thanks goes to my family. Thanks for letting me chose who I wanted to be in total freedom and with all of your support and for always being there for me. Thanks to my dad Pietro, for feeding me with Asimov's books and science documentaries since I was a kid. You taught me curiosity and intellectual honesty. To my mum Ivana, for always looking at the little things of the world with the eyes of a child. You taught me wonder and enthusiasm. To my sister Nadia, for being the sweet one and for always believing in me. It's been very helpful knowing that there was you at home. Thanks to my aunt Noemi for being such an irreplaceable figures throughout my life and to my grandparents. I owe you so much.

My acknowledgement to the people that made my PhD possible, to my supervisor Dr.Giampaolo Pisano, for giving me the possibility to dedicate part of my life to this fascinating research topic and for always trusting me, to Dr.Bruno Maffei, for putting so much love in his job and for always being available and kind. Thanks to Dr.Malcolm Gray, for our fruitful discussions on Masers and vortices and for always talking to me as we were peers. Thanks to "Richard" Dr.Ng, for taking so much care of our lab. Thank you for the singing sessions and for your great integrity. To Vic Haynes, for the enthusiastic and knowledgeable lectures. Thanks for showing me that you can keep all the possibilities open if you have an open mind (and that a good archive is everything). Good luck with your PhD! To Dr.Andrew Markwick, for giving me the very first "welcome aboard" and to Rebecca Shaw, for taking care of

all the administrative issues with such efficiency and kindness.

My very special thank you to all the amazing people that welcomed me at the JBCA and in the crazy 50 Kingsway house and opened a window for me on so many different cultures. I know now I have a real good friend almost at any spot on Earth's surface. To Matias Vidal, Lizette Guzman, Rashmi Verma, Peter Gordon, Richard Taylor, Hayden Rampadarath, Cristina Romero, Cristobal Espinoza, Nikoleta Moutsiou, Adelaide Ladu, Sergio Morales, Sarah Bryan, Claire Wanyama, Adam Von Stanier, Kévin Dalmasse, my beloved little and brave brother Masashi Nozaki and all the others. You are truly beautiful guys!

In these years I also met people that will constantly be part of my life and my thoughts. To "magic" Sotiris Sanidas, for our nice and deep chats in front of a pint (or two). To my favourite pilot Rieul Gendron, for having such a special and peculiar way to look at things. To Melis Irfan, for being such a great friend and always have a smile on her face despite any PhD related suffering we would be going through. To Mareike (Marike) Haberichter, for being my centre of gravity for so long. Thanks for the laughter, for being the "goliarda" of the group (yes, it was her), for the late working nights and the texts at midnight stating"Good news! A new baby Skyrmion was born!". To my precious Claire who-de-pope-I-de-pope Lykou. You know. You just know. Right? Thanks for always being there. To one of the most important persons in my life, princess Gülay Gürkan. I will never be able to say how much you mean to me and how thankful I am to the Universe for making us meet. To my VIP office buddies Fahri öztürk, Ho Ting Fung. Especially my friend Imran Mohamed, for sharing thoughts, feelings and hopes with me and for always being true to himself, that I consider a big virtue. To future-Nobel-prize-winner Peter Schemmel. Thank you for being my buddy, for all what we experienced together, for the fun, the enthusiasm and for all the help and friendship you gave me. Mostly for the pistachios...and for Apple Martinis too. A sweet thought to my dear friend Sharon Bukokhe Tindi. Thanks for the colours, the english lessons, the night chats, our memorable "International Dinners" and for making me change for the better when you left. A huge thank you to The Italians! We are family guys and you are very important to me. Thanks Tommaso Biancalani, Emanuele Spinosa, Ruggero Poletto, Daniele Teresi, Carolina Uggenti, Francesca Oltrabella, Elena Tuccori, Alessandro

Fregoso, Eleonora Balloi, for all the solidarity and the love we shared as friend and as expatriates. Francesca you're a sister to me and we'll keep having our breakfasts together wherever we will be on the planet. Thanks Alessandro, for keeping me sane and for making me laugh in the darkest times. And again Elena, Tommaso...I love you all. Thanks to Alessio Traficante, for your advice and for our chats walking home or anywhere it's allowed to talk. To Anna Bonaldi, for our "corridor" meetings, for the precious help with IDL and for experimentally demonstrating to us that one can be a woman, a mum, a wife, an expatriate and a good scientist all at the same time.

I am especially grateful to Laura P. Fusco, to my childhood buddy Emanuela Montani, my red-wire friend Paolo Glorioso and to my accidental soulmate Simona Righini for sending me love and support even if I was never there. Laura, how could I ever live without you? Thanks for existing and for proving that madness and sanity are just a matter of perspective. To my tutees for showing me that teaching is the best way for learning. I cannot avoid saying thanks to the Corner House and to the Sandbar for being the desperate's refuge and most important for selling beer.

Support from the UK Science and Technology Facilities Council (STFC) Doctoral Training Grant and an EU Bursary are gratefully acknowledged. Thanks to the IT guys Dr.Anthony Holloway and Dr.Robert Dickson ,for keeping everything running, to Paul Wigglesworth and his colleagues. To The University of Manchester for providing the best working environment ever possible and to the UK for making me feel at home since the first day.

A Lui. I kept my last and very special thanks for my love Paolo. We did it! I would have never achieved this without you. Thank you for being such a great and loyal man. Thanks for waiting for me for so long, always making me feel your presence and your support. You never made me feel alone in this, not even for a second. Thanks for always believing in me and pushing me forward to realise my dreams. I love you immensely. You are my strength and my future.

The Author

The author gained her BA degree in Physics and Computer Science for Telecommunication in 2005 at Universita' Cattolica del Sacro Cuore in Brescia, Italy. Her BA thesis work focused on measurements of the electronic temperature dynamics induced by short Laser pulses on a thin film of Py by means of pump-probe experiments. After a few years working as a Maths and Physics secondary school teacher and as an employee, in 2010, she moved to the UK to do a PhD. The work reported in this thesis was performed at the Jodrell Bank Center for Astrophysics of The University of Manchester.

Peer-reviewed Publications

A q-plate for millimetre-wave orbital angular momentum manipulation,
S. Maccalli, G. Pisano, S. Colafrancesco, B. Maffei, M. W. R. Ng and M. Gray,
Applied Optics, Vol. 52, Issue 4, pp. 635-639 (2013)

Three Dimensional Measurements of a Millimetre Wave Orbital Angular Momentum Vortex,
P. Schemmel, S. Maccalli, G. Pisano, B. Maffei and M. W. Ng,
Optics Letters Vol. 39, Issue 3, pp. 626-629 (2014)

List of Abbreviations

HWP Half Wave Plate

L-G Laguerre-Gaussian

LHCP Left-Handed Circular Polarization

OAM Orbital Angular Momentum

PMD Phase Modulating Device

QWR Quarter Wave Retarder

RF Radio Frequency

RHCP Right-Handed Circular Polarization

SAM Spin Angular Momentum

SLM Spatial Light Modulators

SPP Spiral Phase Plate

TAM Total Angular Momentum

VNA Vector Network Analyzer

Chapter 1

Introduction

"The most exciting phrase to hear in science, the one that heralds new discoveries, is not "Eureka!" but "That's funny..."."
Isaac Asimov

Twisted radiation

As often happens in science, researchers find something very new and interesting whilst looking for something else. This was certainly true for *optical vortices*. Phase dislocations were first discovered in radio waves and further studied in ultrasonic waves. Of course vortices and the mathematics associated with them were well know in fluid dynamics but discovering that superpositions of sound or light waves could lead to the generation of vortices associated with field singularities opened up a whole new field of research, mainly in optics. More importantly, it brought new doubts and curiosity about something that scientists thought they understood.

Outline

In this chapter, a general overview on the topic of optical vortices is given, starting from their discovery (Section 1.1). An introduction on the topic is given in Section 1.2, followed by information on the different devices currently used to generate (Section 1.3)

and detect (Section 1.4) optical vortices. The main research fields in which their peculiar properties find applications are listed in Section 1.5. The chapter ends with Section 1.9 where it is summarised why, as a Technology Group within an Astrophysics department, we are interested in optical vortices and what our aims are.

1.1 Discoveries

In 1974 Nye and Berry published a paper [49] where they made the first attempts to interpret and explain phase data of the wavefronts generated by radio waves diffracted by the rough surfaces of the bottom of the Antarctic ice sheet. They could see in the data wavefronts containing dislocation lines. Surprisingly they found that a common property of such dislocations is that the phase changes by an integer multiple of 2π on a closed loop around the dislocation itself (Figure 1.1). They found, in fact, that at a fixed time

$$\left(\frac{\lambda}{2\pi}\right) \oint d\chi = N\lambda\,, \tag{1.1}$$

where λ is the radiation wavelength, χ is the field's phase and N is an integer.

Since this discovery in 1974 a new field of research developed under the name of *Singular Optics*. It has been shown that these *singularities* or *optical vortices* have peculiar properties. Such singularities can propagate and they carry a particular form of angular momentum. We are used to talking about the *spin angular momentum* (SAM) associated with circular polarisation of the field. Optical vortices carry *orbital angular momentum* (OAM), generated precisely by the fact that the phase front is no longer parallel to the transverse plane. Another milestone in this research field was reached in 1992 by Allen and his colleagues with another famous paper [5]. It was already known that Laguerre-Gaussian beam modes (L-G modes) have the same phase structure around the beam propagation axis as the one described in 1.1. In their paper, Allen and colleagues demonstrated that laser beams with the mentioned L-G distribution of the amplitude carry a well defined OAM. Specifically each photon carries $l\hbar$ OAM where l is the azimuthal mode number (corresponding to N in 1.1). Both in the case of radio echoes studied in the Nye and Berry paper and in the case

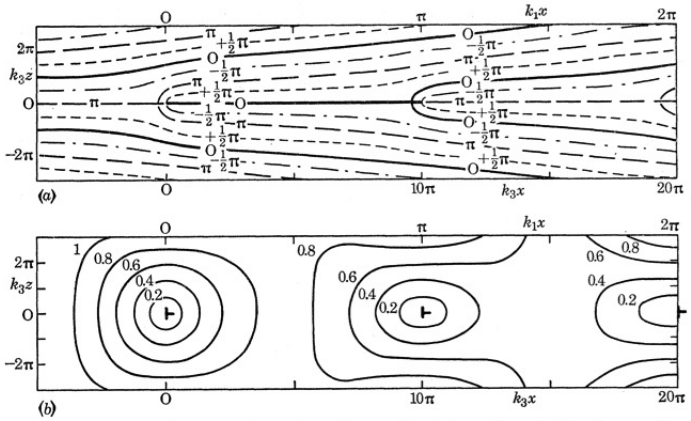

FIGURE 9. (*a*) A row of edge dislocations (tilt boundary) formed by the interference of two pulses of plane waves, each modulated linearly, $\tan\alpha = 0.1$ and $\beta_s = 0{\cdot}1$. The scales are arranged so that the pattern is a true-to-scale map in the (x, z) plane at $t = 0$. Lines of constant reduced phase χ_0 are shown; the dislocations are singularities of χ_0. Any arbitrary value of χ_0 may be chosen to represent crests. The whole pattern moves upwards with velocity $c \sec\alpha$, unchanged in form. (*b*) As (*a*) but showing contours of wave amplitude ρ. The numbers on the curves are values of $\rho/2a_0$. The dislocations are at places where $\rho = 0$.

Figure 1.1: Extract from 1974 Nye and Berry famous paper about dislocations in wave trains [49].

of L-G beams, optical singularities have always been there. L-G beams were not new to optics, but the consequences of their phase structure were not completely identified and understood. Using Nye and Berry's exact words, "We suspect that dislocations may often have been observed in phase sensitive experiments without their significance being appreciated" [49].

Following these breakthroughs in the last two decades there has been very intense production of publications and new results both on the theoretical understanding of optical vortices and on the study of new applications in many fields.

1.2 Topic overview

Here we give a very general overview on what the characteristics of a beam carrying OAM of the kind described in [5] are. A more detailed treatment will be reported in Chapter 2. In the case of an ideal plane wave, the parallel planes of the wavefront are perpendicular to the wave vector $\mathbf{k}$, and these planes are separated by a distance of one wavelength $\lambda = 2\pi/k$. When a wave has a vortex, the wave's equal-phase fronts are no longer parallel and separated but instead form a helical surface wrapped around

the axis of the vortex. The existence of an optical vortex influences the distribution of phase over the whole space despite the defect being located at a specific point. For the conservation of angular momentum singularities naturally form in pairs with opposite distributions of the phase around the singular point (Figure 1.2).

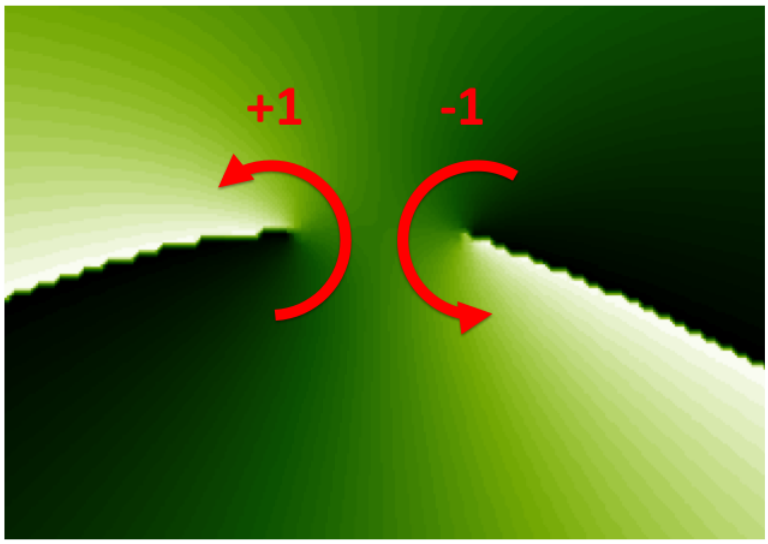

Figure 1.2: When vortices form naturally from interfering wavefronts they come in pairs of opposite sign and same charge (usually |1|) for the conservation of angular momentum.

As previously stated in 1.1, the integration of phase gradient along a closed loop around the axis of the vortex is $2l\pi$, where l is defined as the topological charge. A positive (negative) topological charge corresponds to clockwise (anticlockwise) circling of the ramps of the wavefront along the propagation direction of the z axis. Since the Poynting vector is defined to be perpendicular to the equiphase wave front, in waves with optical vortices this results in it being tilted to the propagation direction and spirals around the axis of propagation of the beam [5]. This leads to a component of the angular momentum not only in the z direction, as is usually the case with circularly polarised waves, but also in the transverse plane, which gives rise to an orbital angular momentum component. A photon can then carry OAM, whose

eigenstates have an azimuthal phase dependence of the form $\exp(il\phi)$, giving rise to the intertwined helical phase fronts. l can be any integer value and it corresponds to the number of times the phase changes by 2π in a closed circle around the beam's axis on the transverse plane. Photons of such a beam carry an OAM $l\hbar$ as found by Allen and colleagues [5]. Since l can take any integer value, there is an infinite number of possible states of OAM. It can be shown that the total angular momentum, TAM , carried by the beam. TAM is one of the key quantities that is conserved, together with energy and linear momentum. It is the isotropy of space that gives rise to the conservation of TAM. It is possible for two photons to have the same TAM, while having different values of OAM and SAM.

Typical characteristics of vortex beams are the annular intensity pattern in the far field and a distribution of the phase as shown in figures 1.3, 1.4 and 1.5. In figure 1.3 the instantaneous amplitude is shown. The profile would rotate along the propagation direction and would give rise to the intensity pattern in figure 1.4 when the square amplitude is averaged over time.

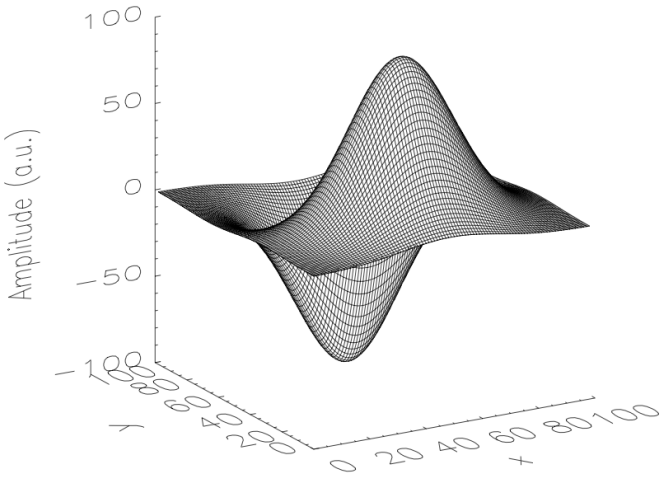

Figure 1.3: Instantaneous amplitude transverse profile of a mode |1| optical vortex (L-G distribution of the amplitude). This pattern will rotate around the propagation axis upon propagation. The time average of the square amplitude generates the intensity profile in figure 1.4.

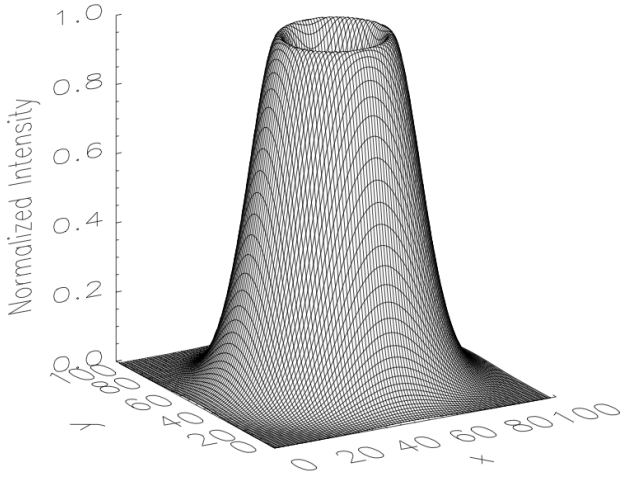

Figure 1.4: Intensity transverse profile of a mode |1| optical vortex (L-G distribution of the amplitude). The intensity value is normalised to the peak intensity.

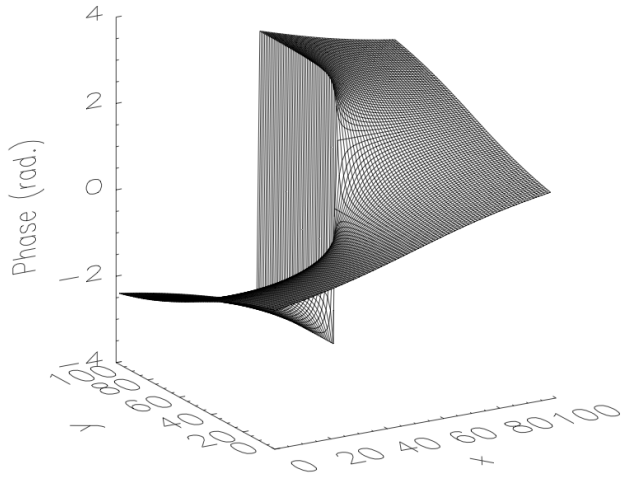

Figure 1.5: Phase transverse profile of a mode |1| optical vortex (L-G distribution of the amplitude).

The most used form to represent the field amplitude of these beams carrying OAM is given by the Laguerre polynomials as explained in the next chapter. The radius of maximum intensity increases with the OAM number as shown in figure 1.6.

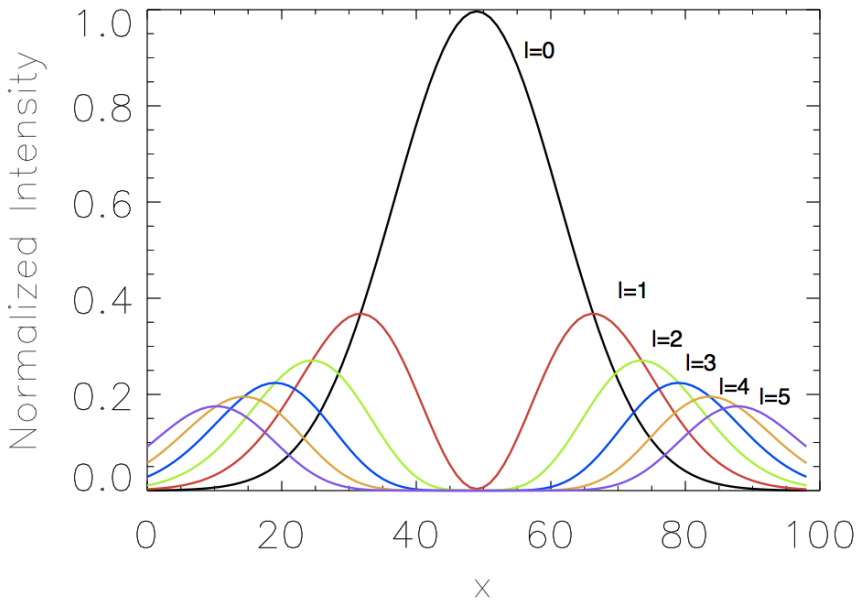

Figure 1.6: Intensity profile of the first six L-G modes that carry OAM. The lines represent a linear horizontal cuts (or vertical as they are symmetric) on the transverse plane perpendicular to the beam propagation axis. l is the azimuthal index of the L-G modes. It indicates the number of times there is a phase change of 2π around the propagation axis.

It has been shown that the angle of the wave vector to the optical axis is l/kr where l is the azimuthal index of the L-G modes, indicating the number of times the phase changes by 2π around the propagation axis, k is the wave vector and r is the azimuthal distance from the axis. It was also demonstrated that the angular momentum per photon is $l\hbar$ [5]. Vortices of charge $|l|>1$ are not stable to most perturbations, which split them in $|l|$ vortices of charge ± 1 [24]. Even a small azimuthal perturbation will grow upon propagation resulting in a number of new vortices flying off the intensity ring. Because of the conservation of the topological charge, the number and sign of the new vortices is defined [33].

The properties just described are very peculiar and find interesting and promising applications in many fields. In Section 1.5 I report the most important, knowing that this is only a general overview on a rapidly expanding field. Before that however, it is useful to look at how it is possible to generate and detect OAM light.

1.3 Phase Modulating Devices (PMDs) to generate light carrying OAM

A beam with a helical wavefront can be produced by a laser that operates in the Laguerre-Gaussian regime. This can be obtained by suppressing the on-axis modes inside the laser cavity by inserting small circular absorbers into the cavity. Using the right combination of absorbers and clear apertures along the propagation axis the modes generated can be made degenerate into a single mode and lock on a single frequency [26]. Alternatively, the distribution of amplitude and phase of a laser beam can be manipulated outside the cavity to obtain a spiral beam starting from Hermite-Gaussian modes and using different devices as cylindrical lenses [14], computer-generated holograms [29], spiral phase plates (SPPs) [13, 68], q-plates [41] or, in the radio domain, with special configurations of antennas [67]. Here we give a short description of some of these optics elements.

1.3.1 Astigmatic mode converters

Beijesbergen and his colleagues designed a mode converter to generate L-G beams which are known to carry OAM starting from Hermite-Gaussian (H-G) modes. They showed both theoretically and experimentally that it is possible to use H-G modes of arbitrarily high order to generate a specific L-G mode of the same order. The converter consists of two cylindrical lenses and is based on the manipulation of the Gouy phase, which is the difference in the phase compared to the one of the correspondent plane wave due to the fact that the beam has a finite waist [14]. Setting the right distance between the two cylindrical lenses and the right orientation of the incoming H-G mode it is possible to introduce a well-defined phase shift between the vertical and horizontal components of the H-G beam and generate the correspondent

L-G beam. A scheme of an astigmatic mode converter specifically designed to induce a $\pi/2$ phase difference is shown in figure 1.7. If the two lenses are placed where the two transverse radii of the astigmatic beams are equal the beam is astigmatic only between the two lenses (figure 1.8).

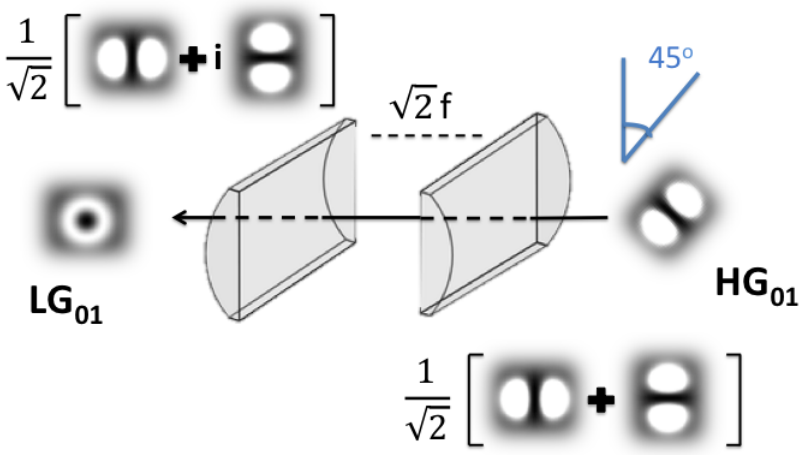

Figure 1.7: $\pi/2$-mode converter as reported by [31]. The incoming H-G beam is a superposition of the two components as indicated. The input is oriented at 45 degrees to the vertical axis of the first cylindrical lens. The outgoing beam is a superposition of the same components which are now phase shifted by a factor that depends on the distance between the two lenses.

This is possibly the most pure mode converter to generate L-G beams but there are some limitations. In order to produce a specific L-G mode the corresponding H-G mode is needed as input and this limits the usage of the converter depending on the H-G modes available. Moreover H-G modes are usually generated by lasers but they might not be the natural choice in other frequency ranges like in the W-band (75-110 GHz) on which this project is focused as explained in section 1.9.

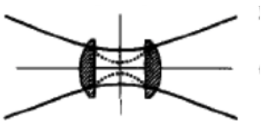

Figure 1.8: The beam is astigmatic, i.e. it is focused differently along the two axes of the lenses, only in the area between the lenses when the lenses are placed where the two components of the beam have the same beam waist. The image is taken from [14]

1.3.2 Computer-generated holograms

It is possible to generate phase singularities using computer generated holograms (or zone plate) [29, 8]. The hologram consists of a diffraction grid with a "fork" with some dislocations as in figure 1.9.

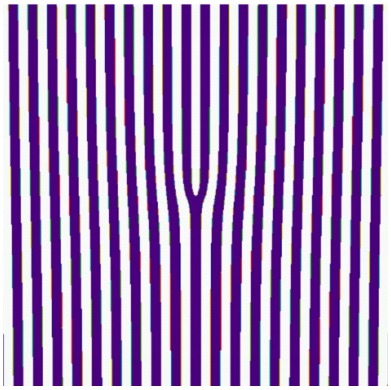

Figure 1.9: Example of a forked computer generated hologram. The binary pattern corresponds to the interference pattern the optical vortex it is designed for would generate with a plane wave.

The resulting helical phase dislocation produced on the diffracted beams axis give the phase structure $\exp(il\phi)$ and the characteristic circular intensity pattern in the far field generated by interference [8]. When holograms with this type of grating are illuminated with a fundamental Gaussian beam mode, the resulting beam is a

superposition of infinite L-G modes with the mode the hologram was designed to generate contributing around 80% of the intensity. The hologram, in fact, is not a pure mode converter and fractions of the power can be found on axis and on the order of diffraction opposite to the relevant one. The desired beam can be found at the first order of diffraction as shown in figure 1.10 [30].

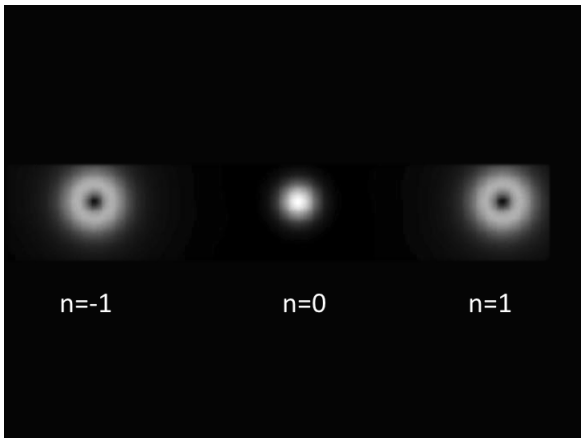

Figure 1.10: Intensity pattern corresponding to the 0,-1,+1 diffraction orders for a mode l=1 hologram illuminated on axis by a Fundamental Gaussian beam.

The precise shape of the forked hologram can be calculated by a simple formula [8]. The required hologram can also be designed by recording, on photographic film, the interference pattern between a plane wave and a beam carrying the OAM one wants to produce. Using pixelated liquid-crystal devices, such as Spatial Light Modulators (SLMs), instead of photographic film, allows one to configure the hologram many times per second [52]. The emerging wave's helicity can be changed by reversing the plate [29]. Combining holographic patterns also gives the possibility of realising devices able to sort a number of OAM states.

1.3.3 Spiral Phase Plates (SPPs)

A SPP is a dielectric plate whose thickness increases proportionally to the azimuthal angle ϕ around its optical axis (see Chapter 2). The total height of the step is h_s as shown in figure 1.11. When the beam passes through the plate, the helical character of the surface twists the beam. For collimated beams and when the SPP's step height

is sufficiently small, we remain within the paraxial regime, so that the plate can be considered as acting only on the phase. The SPP can change the helicity of a helical beam or add the helical structure to an initially non-vortex beam. In most cases, however, the resulting beam is no longer a pure mode, but a superposition of modes. The SPP therefore is not in general a pure mode converter [13]. These SPP can be used not only with laser light but also at millimetre and radio wavelengths [68].

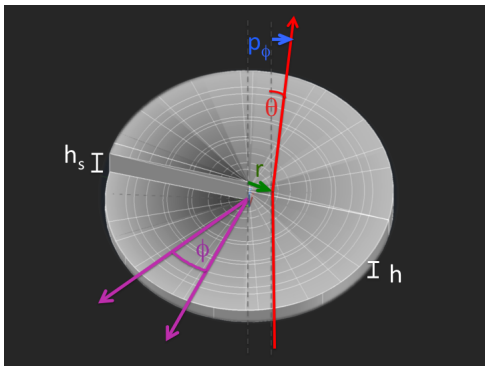

Figure 1.11: Example of a Spiral Phase Plate (SPP) structure.

As shown in figure 1.11 a ray exiting the SPP is refracted. This means the linear momentum of the light gains an azimuthal component. With respect to the radius vector the azimuthal component gives rise to angular momentum along the beam axis. Applying Snell's law at a point of the SPP surface it is possible to calculate the angular deviation of the output ray to the beam axis, which is

$$\frac{(n-1)l\lambda}{2(n-1)} = \frac{l}{k_0 r}\,. \tag{1.2}$$

If this quantity is then multiplied by the linear momentum and the radius vector the result gives an orbital angular momentum per photon of $l\hbar$, as required. More details about the SPP are reported in Chapter 2 as this is one of the devices we chose to design and manufacture.

1.3.4 q-plates

Another way to produce helical waves is using devices called q-plates [41]. When light travels in a vacuum or within a transparent homogeneous and isotropic medium,

both SAM and OAM are conserved. Under appropriate conditions these two forms of angular momentum can be transferred to matter [28, 61]. The transfer of spin to matter can take place within optically anisotropic media, such as birefringent wave plates [15]. An independent coupling of orbital angular momentum with matter is possible in inhomogeneous isotropic media [14, 13]. Therefore a simultaneous and independent coupling of both kinds of momentum with the material happens in a medium which is both inhomogeneous and anisotropic [55]. But as demonstrated by Marrucci and colleagues, they are not entirely independent, in particular conditions the exchange of momentum of spin with matter affects the direction (sign) of the exchange of orbital angular momentum [41]. Specifically the polarisation of the input light controls the sign of the helicity of the output's wavefront [47]. The value of l (number of twisted helices) is dictated by the geometry of the axis of birefringence on the surface of such devices. In figure 1.12 the three design proposed in [41] are shown.

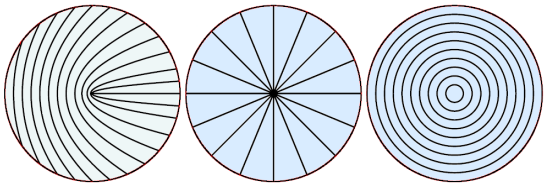

Figure 1.12: Example of a mode |1| (first on the left) and mode |2| (central and right) q-plates as presented in [41]. The lines represent the birefringence optical axis orientation.

In figures 1.13 and 1.14 are shown the expression for α which is the angle at which the optical axis of the birefringence is oriented at each point on the surface of the plate. For the mode |2| plate two different geometries are shown as proposed by Marrucci and colleagues in their paper. The parameter q corresponds to half the value the plate is designed to impart on incoming radiation.

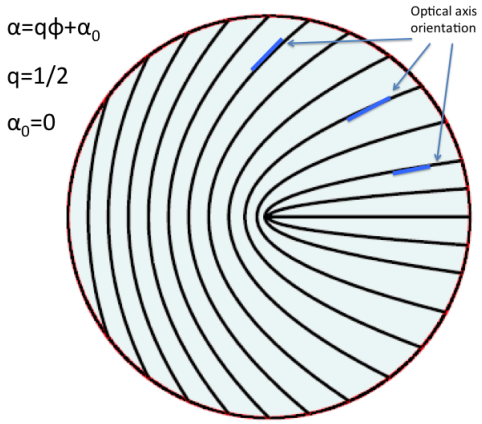

Figure 1.13: The mode |1| q-plate geometry is represented here. At each point the tangent to the lines represents the orientation of the optical axis of the birefringence. 2q is the OAM value that the plate imparts on incoming radiation and α_0 corresponds to a solid rotation.

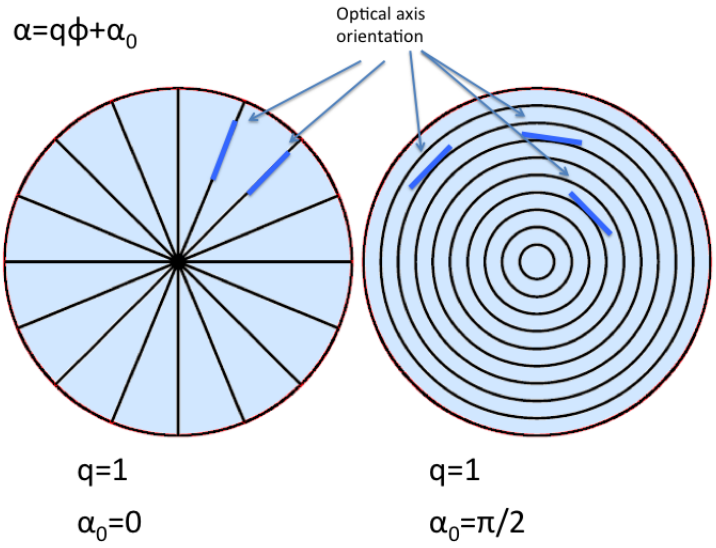

Figure 1.14: The mode |2| q-plate geometry is represented here in two possible versions. At each point the tangent to the lines represents the orientation of the optical axis of the birefringence. 2q is the OAM value that the plate imparts on incoming radiation and α_0 corresponds to a solid rotation. The two different patterns actually represent the same birefringence orientation as the lines of the two plates are perpendicular to each other.

q-plates will be explained in more details in the next chapter as they are the devices we chose to design and produce for this project together with SPPs.

1.3.5 Antenna arrays

It is possible to use antenna arrays to generate and detect both SAM and OAM radio beams [67]. In order to study the possibility of using the OAM in the radio regime (for telecommunication or astronomy) consider an array where, for simplicity, the antennas are positioned the same distance apart around concentric circumferences. Antennas are given the same signal, but each one systematically delayed by a certain amount so that after a full turn around the axis of the arrays, the phase has been increased by $2l\pi$ (figure 1.15).

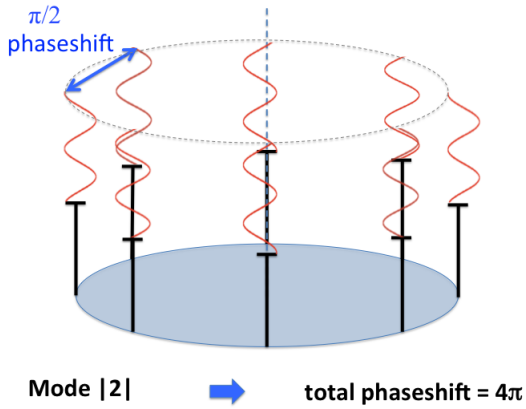

Figure 1.15: Scheme of an antenna configuration for the generation of a mode |2| vortex.

As one can have only a finite number of antennas along the path of integration, there's an upper limit to the number of OAM states that can be solved [44, 67]. Precisely,

$$N_{OAMstates} = \frac{|l|(N_{antennas})}{2}, \tag{1.3}$$

as reported in [67] where this setup was first proposed and studied.

1.4 How to detect OAM

There are different types of experimental setup presented in the literature to analyze beams carrying OAM and separate them into different states. The techniques to generate beams with OAM by using the previously described PMDs can also be used in reverse to detect OAM components of an incoming beam [67, 25, 69, 47, 8].

A hologram, for example, can be used to flatten the phase of an OAM beam that is then focused through a pin hole and detected or directed into an optical fibre. Another simple way, wherever feasible, to highlight the helical character of a beam characterised by a pure OAM state is to make the beam interfere with a reference beam that is approximately plane or with the same curvature of the beam under examination. In this way it is possible to detect the interference fringes whose structure shows the exact nature of the helical phase structure of the beam [19, 34]. As it can be seen in figure 1.16 the interference pattern generated by the optical vortex with a plane wave will show a central fork that would not exist if the beam was not a vortex. The interference fringes will present as many forks as the l value of the incoming beam vortex. This interference pattern, if recorded, is the pattern that a hologram should have in order to generate that particular vortex.

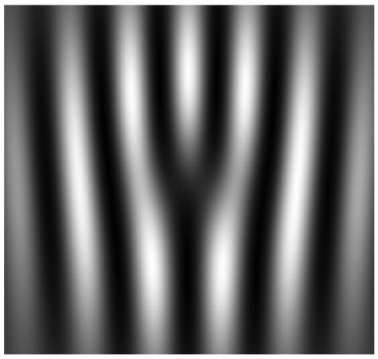

Figure 1.16: Interference pattern of a $l = |1|$ vortex with an inclined plane wave as reported in 1.16.

Sparse configurations of antennas can be used to sample the signal and reconstruct the phase structure with the same principle they are used to generate it.

Moreover, at millimetre wavelengths, detectors or antennas connected to field analysers have been used to scan the transverse plane of the beam through the transverse plane on the nodes of an ideal discrete grid as shown in figure 1.17 [68, 37].

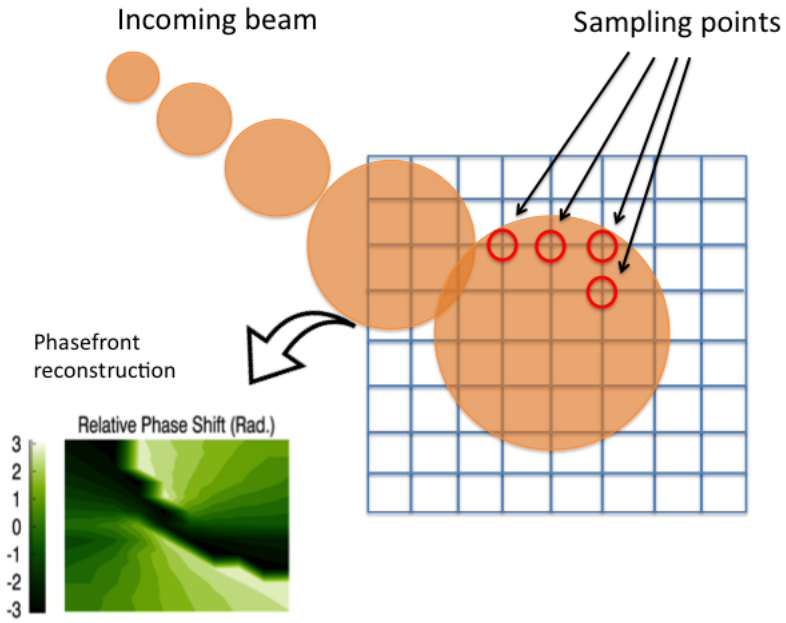

Figure 1.17: At millimetre wavelengths a receiving horn on a support that can move horizontally and vertically can be used to sample the field at the nodes of an imaginary grid. The data can then be used to reconstruct the beam intensity and phase pattern if the receiver is connected to a vector analyser [37].

Mode analysers that can also measure the radial mode index of the vortex beam have been presented in [3]. Specifically, the full angular and radial mode spectrum can be measured using an optical Mach-Zender interferometer that combines spatial rotators such as Dove prisms and a realisation of the fractional Hankel transform by means of spherical lenses. The Hankel transform consists of a 2D radially symmetric Fourier transform. In the previously mentioned work the fractional Hankel transform is realised using two spherical lenses and its order is controlled through the focal distance and the separation between the two lenses.

All these techniques require the analysis of the whole beam in order to determine

its OAM content. Methods that combine the use of holograms and pinholes work with single photons but can only distinguish a single OAM state.

The best method to date to sort photons with different l values in a theoretically 100 % efficient way and for an arbitrarily large number of l values is the interferometric method presented by Leach and colleagues in [36]. This technique exploits the rotational symmetry that characterises the phase of photons in OAM eigenstates. The symmetry comes from the azimuthal dependence of the phase given by $\exp(il\phi)$. If the beam is rotated by a certain angle α the phase dependence becomes $\exp(il(\phi+\alpha))$, corresponding to a phase shift of $l\alpha$. Given a value for α, there will be values for l for which the rotated beam is either in phase or out of phase with respect to the original non-rotated one (see figure 1.18).

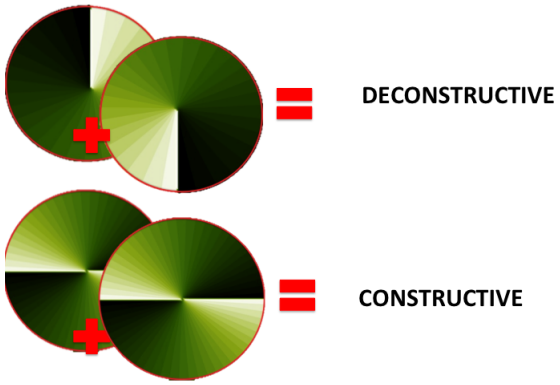

Figure 1.18: Superposition of an odd (top) and even (bottom) OAM mode phase profile for an equal rotation of the beam of π.

In a Mach-Zehnder interferometre like the one in figure 1.19, where Dove prisms are inserted in the two arms, the beams can be rotated with respect to each other by an angle α creating the above mentioned $l\alpha$ phase shift [35]. Dove prisms, specifically, are truncated prisms that exploit total internal reflection to flip an image as shown in figure 1.20. This way the phase-shift between the two arms becomes l dependent.

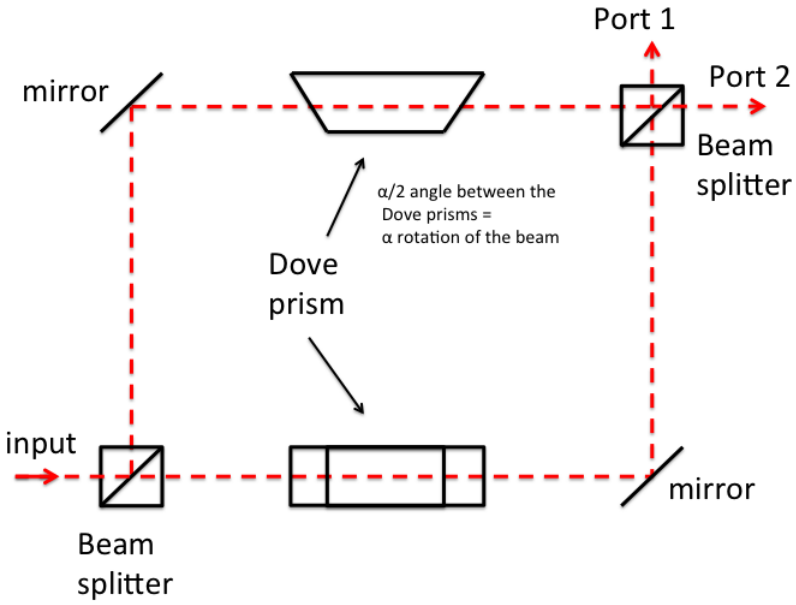

Figure 1.19: Scheme of the Mach-Zehnder interferometre for the OAM states sorting. The Dove prisms inserted in the arms allow us to rotate the beams by an angle α with respect to each other so that the phase shift between the beams in the two arms becomes l dependent. Choosing the appropriate path length makes the odd and even OAM charged photons end up in different output ports.

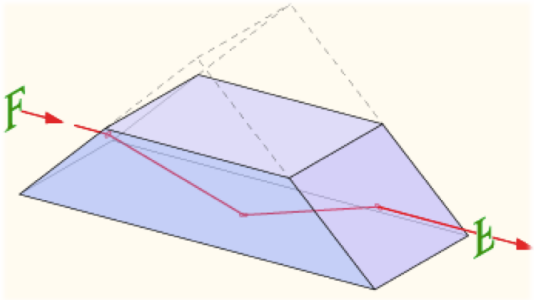

Figure 1.20: A Dove prism is an optical element obtained from a truncated right-angle prism. The light entering the prism undergoes total internal reflection. This results in an inversion of the image on the other side of the prism.

For instance, when a beam with an even topological charge undergoes a rotation of 180° about the axis, the phase at every point is the same as the non-rotated beam, while, if you make the same rotation on a beam with odd charge the field at any point is out of phase with the original beam [19, 18]. Adjusting correctly the path length of the interferometer photons of odd and even l can be made to appear at the two different output ports of the interferometer. It is in principle possible to sort an arbitrarily large number of OAM states cascading additional Mach-Zehnder interferometers where different rotation angles are applied. Using an interferometer where the rotation is not of 180° but other different angles, in fact, the beam can be further subdivided [36, 70, 71, 35, 51].

1.5 Applications

In the last few years, after the discovery of the first optical singularities [49], and the later discovery that L-G beams carry a defined and quantised OAM [5], optical vortices have become an important tool in different fields.

1.6 Telecommunication

Probably the most promising characteristic of optical vortices is that their OAM state can have any integer value that ranges from $-\infty$ to $+\infty$. This means that OAM photons can potentially carry much more information than non-OAM photons. Usually the two states $(+1, -1)$ of the SAM are used to transfer information through photons as they represent a single bit (qbit). Using OAM states, associated with the phase structure, instead of SAM states, associated with the circular polarisation, allows a lot more information to be embedded in a single photon. It could be assumed, for example, that the first 26 values of OAM the photon can carry represent the letters of the English alphabet. This is the reason why most of the research regarding optical vortices and light carrying OAM has been focused on quantum encryption and telecommunication, showing that these property of light could potentially improve how we transfer our data [46, 47, 45, 23, 25, 44, 63, 42]. This higher-dimensional quantum space encoded in a single photon (quNit) can be used to generate bound

states, for example through parametric down-conversion in the quantum teleportation [32, 39, 69]. In [39], in particular, for the first time it was presented an experiment where beams carrying OAM were used to create multi-dimensional entanglement. They started with beams carrying OAM values

Another area where optical vortices have been largely employed is that of optical trapping. The peculiar ring shaped intensity profile of a vortex beam and the forces within it make it particularly suitable as optical tweezers or spanner [60, 48, 61]. Making the parallel with SAM, as before, we can see that illuminating a small particle with circularly polarised light would impart spin momentum to it, making the particle rotate around its own axis, while illuminating it with an OAM beam would impart orbital momentum on it making the particle rotate around the beam's axis, trapped within the high intensity ring. For a particle sized the order of microns, a single focused laser beam can produce a force gradient which prevails over the scattering force and gravity [28].

The trap works because the particle is transparent and its refractive index is higher than that of its surroundings. When the particle is on axis and centred where the beam is focused the light just goes through. But if the particle is displaced this causes diffraction and consequently a force gradient that attracts the particle towards the field maximum (figure 1.21) because of the reaction force. Scattering force is also present so the final position of the particle is dictated by their resultant force. This applies in both the on axis and lateral directions as explained in [17]. The scattering of light by the particle from the inclined helical wavefront then imparts rotation to the particle.

The transferring of orbital angular momentum to particles could also be useful to storing information in atoms instead of photons, which are better performing. They have been shown, in fact, to be more manipulatable for conserving data for a long time [72].

Moreover the study of optical vortices properties brings the possibility of applications in the following fields: subwavelength resolution nanooptics, biological cell handling, microfluidics, nanofabrication, laser cooling and the control of Bose-Einstein condensates, to name the most relevant. But there is another research field where

a better understanding of light carrying OAM could lead to big improvements and maybe open totally new horizons. It is the case of Astrophysics.

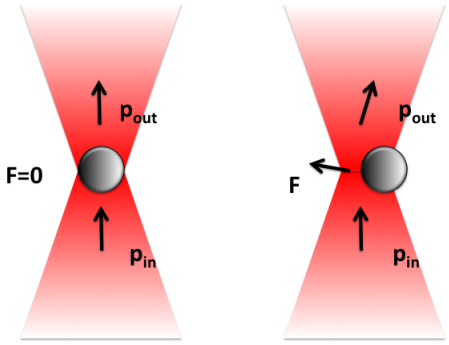

Figure 1.21: The gradient force keeps a particle with the refractive index higher than the surroundings in place because of the reaction force [17].

1.7 Astrophysics

The first and most significant paper concerning the study of OAM in astrophysics was written by Harwit in 2003 [27]. He proposed a range of applications to gain additional information about astrophysical environments. However, to our knowledge, the first and only on-sky direct measurement from astronomical sources has been made by Sanchez and colleagues [56]. The possibilities include the analysis of maser radiation (from interstellar and circumstellar masers) that, after passing through regions with density and refractive index discontinuities, has acquired OAM in the same way that it would with an SPP. In a similar way he considers other sources such as pulsars and quasars, or scattered radiation from Kerr black holes.

The latter case was theoretically confirmed in a notable paper by Tamburini et al.[66]. Kerr Black Holes are massive astrophysical objects that drag and bend the space-time around them as they rotate. Numerical modelling demonstrates that this environment deflects light emitted near them and modifies its phase structure. An asymptotic observer can, in principle, detect such effects and measure an OAM spectrum. This method could be used as an observational tool to identify rotating

massive objects such as black holes. In figure 1.22 some of the numerical results presented in [66] are reported. Highlighted here is the difference in the OAM spectrum between black holes with a higher and lower space-time dragging coefficient.

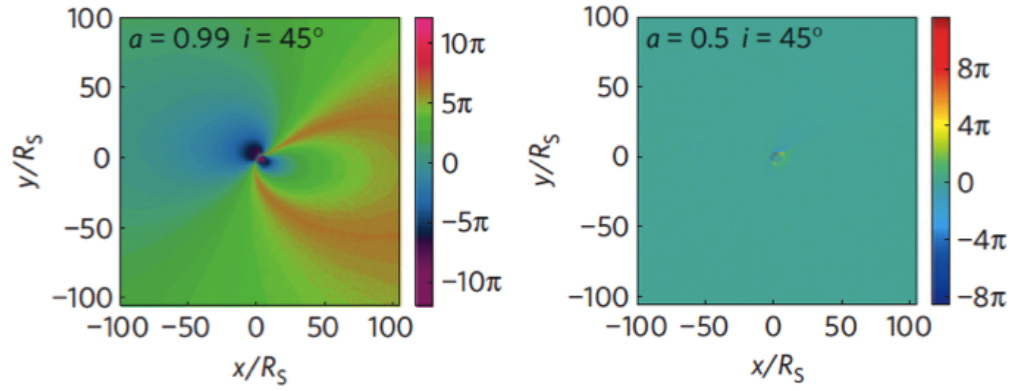

Figure 1.22: The results found by Tamburini and his team as reported in [66]. A wider bimodal OAM spectrum is found for a black hole with a higher space-time dragging coefficient a (left), while a narrower and localised OAM spectrum is calculated for a black hole with a lower coefficient a. Both the plots are normalised to the results for a quasi-static black hole.

Harwit also discussed the possibility of distinguishing discontinuities in density encountered by the radiation from the surface of last scattering. The Cosmic Microwave Background Radiation itself possesses $l = 0$. Other works show how the OAM can be used to overcome the Rayleigh imaging resolution limit as explained in a paper by Tamburini [40]. In this work it was demonstrated both experimentally and numerically that the separability of two independent and equally luminous light sources can be greatly improved by exploiting the properties of optical vortices.

Specifically, the diffraction pattern of the two sources cross a fork hologram but one of the two is not aligned with the centre of the hologram. The misalignment generates an asymmetric L-G pattern in the superposed output beams. The intensity asymmetry due to the misalignment of one of the beams on the hologram generates a non-zero intensity in correspondence of the position that would represent the first minimum in case of perfectly aligned beams. Tamburini and colleagues developed a criterion to separate the two sources looking at the intensity variation at this first minimum (figure 1.23). It was shown that the lower limit of the resolution using this method achieved using white sources is still an order of magnitude better than the Rayleigh Criterion.

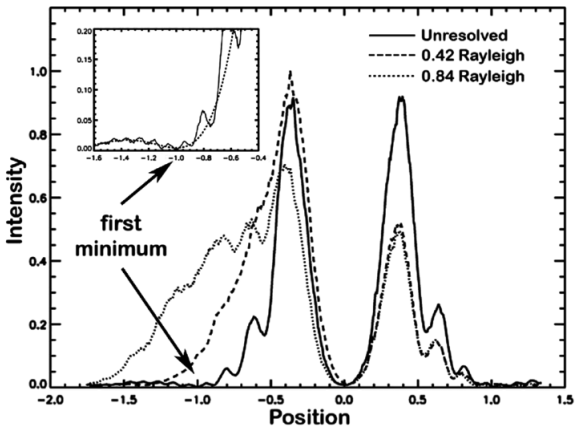

Figure 1.23: Intensity pattern of the superposition of the separate independent sources beams after passing through a hologram. Misaligning one of the sources beams with respect to the hologram centre results in an asymmetry in the intensity profile. A non-zero intensity value at the first minimum can be detected before the separation between the two sources reaches the Rayleigh limit. The plot is reproduced as reported in [40]

Moreover, it was demonstrated in 2009 [9] that the properties of optical vortices find application in astronomical coronagraphy. The conventional mask used in coronagraphs is replaced with a SPP. This way a star light beam directed toward the centre of the SPP will produce a symmetric annular intensity pattern with a minimum central intensity value. Instead, any source not centred with the SPP central point would produce an asymmetric pattern with a non-zero intensity on axis.

The simulations show that the intensity of the on-axis star can be reduced by 10 orders of magnitude. This technique is therefore suitable for the detection of faint sources around stars like extrasolar planets.

The OAM exchange between photons and plasma has also been theoretically studied in the case of plasma with a helical structure and with rotating vortices and the results are reported in [65]. Detecting and studying these effects will provide additional information both in the case of laboratory experiments and in space.

1.8 Atmospheric turbulences

The same principles can be used to detect aberrations caused by atmospheric turbulence, and the resulting changes in refractive index through the study of how these affect the OAM of a given radiation [54, 43]. It was also discovered that the so-called branch points found when using adaptive optics are actually indicators of the presence of photons carrying OAM, that they form in pairs which are persistent and that through their mapping it is possible to extract all the four terms needed for the layered atmospheric model: number, velocity, distance and strength [50].

This research was then extended to show that, as a parallel to Earth's atmosphere, any turbulent astrophysical region of atoms and molecules would imprint OAM on waves propagating through them. As such conditions can be found almost everywhere in space OAM is highly expected to be measured. Initial on-sky data seem to confirm fluxes up to 17% for the star HR1895 [56].

1.9 Our project

Our research group is part of the School of Physics and Astronomy. Its main research is oriented toward the development of new technology and the improvement of the existing technology. We are consequently very interested in the possibilities that a further study on the properties of OAM light would open in terms of direct astronomical measurements, telescope technology and telecommunications. Radiation carrying OAM is already being used to improve the resolution of telescopes or for coronagraphy, but the big goal would be to perform direct astronomical observations.

Finding that specific astrophysical environments actually generate light that carry OAM would open a whole new branch of research. Maps including OAM data would provide a lot more information to astronomers. This additional information would help understanding about the discontinuities and turbulences that light has gone through on its way from the source to us. It indeed is a big challenge and many steps have to be taken before starting development of a proper instrument. This work represents the very first step of this process and consists of the beginning of understanding the physics behind optical vortices, implementing new laboratory equipment and procedures in order to experiment such physical phenomena. Most importantly, we need to start producing devices for the generation and manipulation of OAM of light at the millimetre wavelengths we are interested in. The most efficient way to generate L-G beams at optical frequencies is by the use of astigmatic mode converters like the cylindrical lenses mentioned before. They are in fact pure converters as they generate a pure L-G mode and not a superposition of modes. It would be natural to think this would be the best choice for the millimetre wavelengths we are focusing on but in this range of the electromagnetic spectrum this method presents practical disadvantages. First, in order to generate a certain L-G mode, and consequently a specific OAM carried by the beam, a well defined H-G mode is needed as input. This limits the possibility of combining different PMDs to generate different states. With SPPs and q-plates instead we can easily position more than a plate on the optical path to modify the beam. Moreover, the higher H-G mode necessary as an input would be hard to create in an RF lab where the feed horn antennas used as sources naturally produce the fundamental Gaussian mode. Devices that can generate OAM beams starting from a fundamental Gaussian mode are the cheapest and most natural choice at millimetre wavelength and considering our existing equipment. We chose to produce and study only SPPs and q-plates for this project. In parallel to this work, colleagues are trying to recognise astrophysical environments or sources that could represent good targets for the first future observations. The results from the first phases of our project have been already presented in two papers [37, 58].

Chapter 2

OAM and PMDs theoretical overview

"Aye, I suppose I could stay up that late."
James Clerk Maxwell

Outline

In this chapter we look at how the orbital component of the angular momentum of light is defined (Section 2.1). The mathematical formulation we use for describing OAM carrying beam is, which, for our purposes is the L-G formulation (Section 2.2) is explained. In the same section, more information is given about the *Paraxial Approximation* that applies in most experimental cases. Some comments about the Poynting vector of the optical vortices are reported in Section 2.3. In Section 2.4 we look at how two of the devices mentioned in Chapter 1, normally used for the generation (or detection) of optical vortices, work. Their working principles are explained together with the equations that will be needed to design phase plates for any desired mode. The full description of the SPPs can be found in Section 2.4.1 while the q-plate behaviour is explained in Section 2.4.2.

2.1 OAM introduction

Light is a dynamic entity. In its motion, light transports energy and momentum. As with any other mechanical motion there are two forms of momentum, one associated with the translational motion, the *linear momentum*, and the other one associated with the rotational motion, the *angular momentum* (Fig. 2.1). In the case of electromagnetic fields, the former gives rise to *radiation pressure* and the latter to *optical torque*. As the linear momentum vector identifies the quantity of linear motion, the TAM represents the amount of "rotation" present in the electromagnetic field. The linear momentum and the TAM are separately conserved as a consequence of the homogeneity of space (shift symmetry) and isotropy of space (directional symmetry) respectively. The TAM can be further represented with two components associated with the two possible forms of rotation in a beam of light, spin and orbital, identified by σ and l respectively. In most cases, for instance when a beam is tightly focussed, the SAM and OAM are not totally independent and only the total angular momentum can be determined. A case where SAM and OAM are independent is when a beam satisfies the conditions for *paraxial approximation* (section 2.1.2). When this happens, the two components of the TAM can be determined and manipulated separately. The SAM depends on the polarisation of the field and its value, σ can be $+1$ or -1 for left and right circular polarisation. The OAM value l depends on the spatial distribution of the field, the phase planes structure, and can assume infinite integer values ranging between $-\infty$ to $+\infty$. The value l is generally called the *topological charge* of the beam. From the wave point of view these two forms of angular momentum identify with the circular polarisation of the radiation and with the local tilt of the wavefront to the propagation axis respectively. If the photon point of view is assumed, the SAM can be seen as the amount of rotation of the photon on its own axis, while the OAM is the amount of rotation due to the photon not moving in a straight line (Fig. 2.2). In the case of a perfectly spiral wavefront the photon would be "orbiting" around the z axis while propagating.

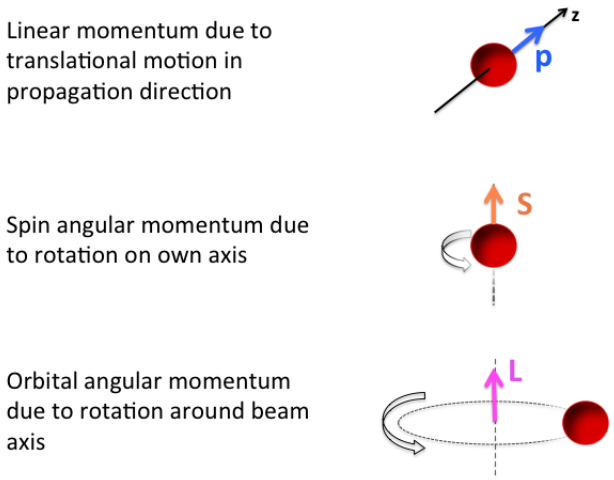

Figure 2.1: Representation of the linear momentum (top), spin (centre) and orbital (bottom) angular momentum vector of a photon.

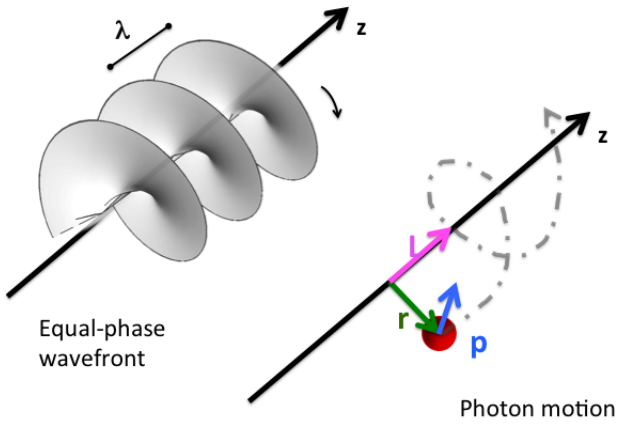

Figure 2.2: Wave and photon representation of the OAM of light. On the left the equal-phase front of a wave with OAM state |1|. On the right, the momentum vector scheme of a photon belonging to such a beam.

As we said above, in real optics applications and experiments, two general situa-

tions can be distinguished for a light beam; when the *paraxial approximation* applies and when it does not apply. In the paraxial approximation the "spreading" of the beam, with respect to the ratio between the wavelength and the increment along z, is much smaller than the rate at which the amplitude changes with z. In other words, the beam is collimated. In the case the approximation does not apply the beam is tightly focused and the diffraction effect due to the small size of the beam at the focus is much bigger.

In general, the total linear and angular momenta are defined by the integrals of the densities of linear and angular momenta for the field as functions of $\mathbf{E}$ and $\mathbf{B}$ as follows.

$$\text{Total linear momentum } \mathbf{P} = \int \epsilon_{\mathbf{0}} \mathbf{E} \times \mathbf{B}\, \mathbf{d^3 r}\,. \tag{2.1}$$

$$\text{Total angular momentum } \mathbf{J} = \int \epsilon_{\mathbf{0}} \mathbf{r} \times (\mathbf{E} \times \mathbf{B})\, \mathbf{d^3 r}\,. \tag{2.2}$$

As explained in the analysis by Barnett and Allen in [10], considering only monochromatic fields, introducing the complex notation and using the Maxwell equation $i\omega\mathbf{B} = \mathbf{E}$, the two momenta becomes:

$$\mathbf{P} = \frac{\epsilon_{\mathbf{0}}}{\mathbf{2i}\omega} \int \mathbf{\Sigma_{j=x,y,z}} \mathbf{E_j^*} \nabla \cdot \mathbf{E_j}\, \mathbf{d^3 r}\,. \tag{2.3}$$

$$\mathbf{J} = \frac{\epsilon_{\mathbf{0}}}{\mathbf{2i}\omega} \int \mathbf{\Sigma_{j=x,y,z}} \mathbf{E_j^*} (\mathbf{r} \times \nabla) \mathbf{E_j}\, \mathbf{d^3 r} + \frac{\epsilon_{\mathbf{0}}}{\mathbf{2i}\omega} \int \mathbf{E}^* \times \mathbf{E}\, \mathbf{d^3 r}\,. \tag{2.4}$$

If only beams propagating in the z direction are considered and the momenta are

evaluated per unit length and averaged over an optical period $2\pi/\omega$ they become

$$P = \int\int \mathbf{E} \times (\nabla \times \mathbf{E}) \mathbf{dx}\, \mathbf{dy}\,. \tag{2.5}$$

$$\mathbf{J_z} = \frac{\epsilon_\mathbf{0}}{\mathbf{2i}\omega} \int\int [\mathbf{r} \times (\mathbf{E} \times (\nabla \times \mathbf{E}))]_\mathbf{z}\, \mathbf{dx}\, \mathbf{dy}\,. \tag{2.6}$$

The expression within the integral in (2.6) can be written as follows

$$[\mathbf{r}\times(\mathbf{E}\times(\nabla\times\mathbf{E}))]_\mathbf{z} = \mathbf{\Sigma_{j=x,y,z}} \mathbf{E_j^*} \frac{\partial}{\partial\phi} \mathbf{E_j} + (\mathbf{E_x^*E_y} - \mathbf{E_y^*E_x}) - \mathbf{\Sigma_{j=x,y,z}} \mathbf{E_j^*} \frac{\partial}{\partial \mathbf{x_j}} (\mathbf{xE_y} - \mathbf{yE_x})\,. \tag{2.7}$$

The first and the second term can not be automatically associated with the OAM and SAM of the beam as under integration over ϕ and ρ they show an interconnection. While the second term, if integrated, depends only on σ_z, the first term, instead, if integrated across the transverse plane show a dependance from both l and σ_z. Therefore it is not possible to consider the first term as the contribution of OAM only.

However, in most experimental situations as well as in this work the paraxial approximation applies.

2.2 Paraxial Approximation and Laguerre-Gaussian modes

In beams where the paraxial approximation applies, that is when the size of the beam is much larger than the wavelength, the propagation directions make small angles

with the optical axis.

When this approximation applies, the second-order differential equation derived from Maxwell's equations

$$\frac{\partial^2 u}{\partial x^2} + \frac{\partial^2 u}{\partial y^2} + \frac{\partial^2 u}{\partial z^2} - 2ik\frac{\partial u}{\partial z} = 0\,, \tag{2.8}$$

becomes a simpler first-order equation. In equation (2.8) u is the field's complex amplitude, x, y, z the spatial coordinate, i is the imaginary unit and k is the wave vector that is equal to $2\pi/\lambda$. The paraxial approximation states that the field's amplitude varies slowly with z, or alternatively, the rays make small angles with the beam axis, as expressed in (2.9)

$$\left[\Delta\left(\frac{\partial u}{\partial z}\right)/\Delta z\right]\lambda \ll \frac{\partial u}{\partial z}\,, \tag{2.9}$$

Applying this condition allows us to neglect the third term in (2.8). That brings us to the *paraxial wave equation* in (2.10)

$$\frac{\partial^2 u}{\partial x^2} + \frac{\partial^2 u}{\partial y^2} - 2ik\frac{\partial u}{\partial z} = 0\,. \tag{2.10}$$

The paraxial approximation directly leads to the derivation of Gaussian optics as the Gaussian beam modes are solutions to this equation.

If we define the complex E field as

$$E(r,\phi,z) = u(r,\phi,z)\,\exp(-ikz)\,, \tag{2.11}$$

where $u(r,\phi,z)$ is the complex amplitude, then the simplest solution of the

paraxial wave equation is the fundamental Gaussian beam mode which corresponds to a complex amplitude $u(r, \phi, z)$ such as the one expressed in the following equation

$$u(r, \phi, z) = \frac{w_0}{w(z)} \exp\left(\frac{-r^2}{w(z)^2} - \frac{i\pi r^2}{\lambda R} + i\phi_0\right), \tag{2.12}$$

where r is the distance from the beam centre on the azimuthal plane, w_0 is the beam waist, the radius of the beam where the radius of curvature is infinite, λ is the wavelength and the other parameters (*beam radius*, *confocal distance*, *radius of curvature* and *Gouy phase*) are defined as following,

$$\text{beam radius}: \; w(z) = w_0\sqrt{1 + \left(\frac{z}{z_c}\right)^2}, \tag{2.13}$$

$$\text{confocal distance}: \; z_c = \frac{\pi w_0^2}{\lambda}, \tag{2.14}$$

$$\text{radius of curvature}: \; R(z) = z\left[1 + \left(\frac{z_c}{z}\right)^2\right], \tag{2.15}$$

$$\text{Gouy phase}: \; \phi_0 = \arctan\left(\frac{z}{z_c}\right). \tag{2.16}$$

Specifically the Gouy phase is the longitudinal phase delay with respect to the phase of the corresponding plane wave.

$$E(r,\phi,z) = \frac{w_0}{w}\,\exp\left(\frac{-r^2}{w^2} - ikz - \frac{i\pi r^2}{\lambda R} + i\phi_0\right)\,. \tag{2.17}$$

The higher order Gaussian beam modes are also solutions of the paraxial wave equation. They can describe beams with a more complex variation of the amplitude of the electric field on the transverse plane. Specifically they consist of the fundamental Gaussian profile modulated by the Laguerre polynomials. They also have a high degree of circular symmetry which is convenient for most practical situation. The Hermite-Gaussian modes are also solutions of this wave equation but they are more convenient to describe situations with a strong rectangular symmetry. Their indices n and m represent the number of nodes the field amplitude has on the x and y directions. They are usually used to describe laser modes. For the case of this project L-G modes are the natural choice as they describe the beams generated by the corrugated circular feed horns used in RF experiments well and already contain the phase factor that gives rise to the helical phase structure of OAM beams.

They can be described by the following equation:

$$\begin{aligned} E_{p,l}(r,\phi,z) = &\left[\frac{2p!}{\pi(p+l)!}\right]^{0.5}\frac{1}{w(z)}\left[\frac{\sqrt{2}r}{w(z)}\right]^{l} L_{p,l}\left(\frac{2r^2}{w^2(z)}\right) \\ &\exp\left[\frac{-r^2}{w^2(z)} - ikz - \frac{i\pi r^2}{\lambda R(z)} - i(2p+l+1)\,\phi_0(z)\right] \\ &\exp\left(il\phi\right), \end{aligned} \tag{2.18}$$

where L_p^l is the correspondent generalised Laguerre polynomials as expressed in equation (2.19), p being the radial index and l the azimuthal index [14].

$$L_p^l(u) = \frac{e^u u^{-l}}{p!}\frac{d^p}{du^p}(e^{-u}u^{p+l})\,. \tag{2.19}$$

The value of $p+1$ indicates how many times a node would be found in the field's amplitude moving out from the centre of the beam on a plane perpendicular to the propagation axis. The l value represents how many cycles of 2π the phase makes on a circle on the azimuthal plane closed around the propagation axis (Fig. 2.3).

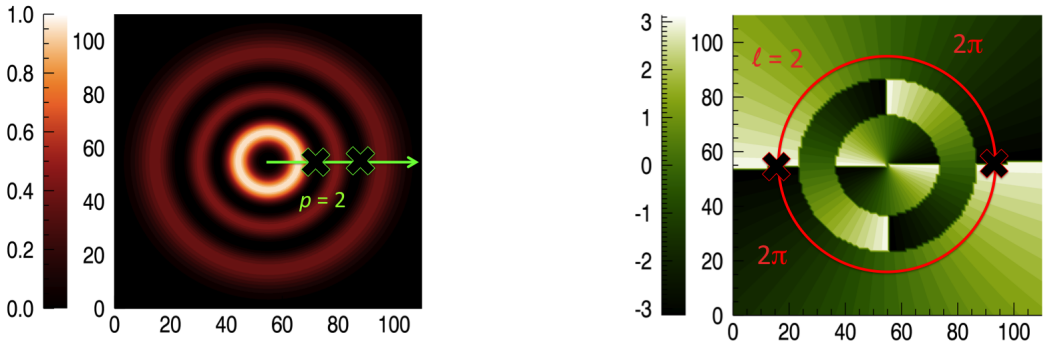

(a) *(b)*

Figure 2.3: p represents the radial index of the L-G modes in equation (2.18) (a). $p+1$ is the number of nodes found in the field's amplitude on the beam radius. In b) the azimuthal index l of the L-G modes is represented. l is the number of times the field's phase changes by 2π around the beam's axis.

If the time averaged angular momentum density, $\epsilon_0 \mathbf{r} \times \langle \mathbf{E} \times \mathbf{B} \rangle$ is now calculated for the paraxial case and evaluated along z as shown by Allen and colleagues in [5] the result is

$$M_z = \frac{l}{\omega}|u|^2 + \frac{\sigma_z r}{2\omega}\frac{\partial |u|^2}{\partial r}\,, \tag{2.20}$$

where ω is the angular frequency and u is the complex amplitude as defined in (2.11).

All the L-G solutions are normalised so that each represents unit power flow and they obey the orthogonality relationship

$$\int\int r dr d\phi \, E_{pl}(r,\phi,z) E^*_{qn}(r,\psi,z) = \delta_{pq}\delta_{ln} \, . \tag{2.21}$$

The orthogonality of the L-G modes implies that, in the ideal case in which we can use all of the infinite solutions, it is possible to describe any generic beam as a superposition of such modes with a unique set of coefficients. In such beams the equal-phase wave fronts are no longer parallel to each other as they would be in an ideal plane wave or in a fundamental Gaussian beam. Instead they have a helical structure with l intertwined ramps where l is the OAM number. That means that a hypothetical line parallel to the propagation axis would intercept a plane with the same value of the phase l times in the space of one wavelength.

Taking the derivative with respect to the radius coordinate r of the squared amplitude of the L-G set and setting it to be equal to zero, the maximum intensity radius for the different modes at $z = 0$ (figure 2.4) can be determined.

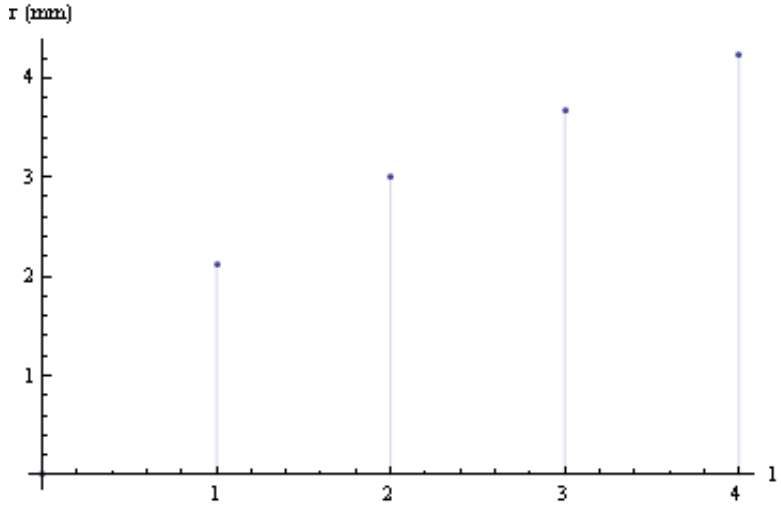

Figure 2.4: Maximum intensity radius for different modes at $z = 0$.

However, it was demonstrated [20] that for the case of a real optical system the radius of maximum intensity is not the one predicted by theory of a free space L-G beam. Curtis and Grier found that in an experimental set-up used to generate optical

vortice by the dynamic holographic technique such as the one reported in figure 2.5, the radius of maximum intensity, R_l, scales as l and not as $\sqrt{l}$ as expected.

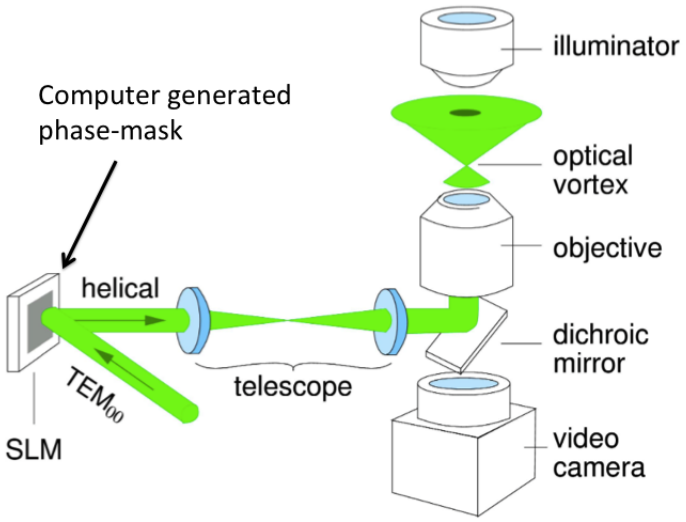

Figure 2.5: Optical system for the generation of optical vortices by the dynamic holographic technique as illustrated in [20]. A parallel-aligned nematic liquid crystal spatial light modulator (SLM) is used to imprint computer-generated patterns of phase shifts onto the wavefront of a linearly polarised TEM beam at $\lambda = 532$ nm. The generated vortex can be used to impart a torque on colloidal particles.

The discrepancy with the theoretical case is due to diffraction induced by the finite sizes of the real optical system. Specifically, they found

$$R_l = a\frac{\lambda f}{\pi\Sigma}\left(1+\frac{l}{l_0}\right), \tag{2.22}$$

The field in the focal plane of a lens of focal length f is related in scalar diffraction theory to the field at the input aperture through a Fourier transform. Σ is the optical train's effective aperture that is a parameter that indicates how much power of an ideal incoming plane wave the system can collect. a and l_0 are experimental parameters that depend on the beam's amplitude. In the case of the experiment reported in the mentioned paper they were found to be with a=2.585.

The wavelength λ and the beam waist w_0 chosen in the calculations correspond to the ones used in the laboratory, which corresponds to $\lambda = 3\,\text{mm}$ and $w_0 = 5\,\text{mm}$. In principle it does not make any difference as everything can be easily scaled. A change in the wavelength or in the beam waist means a change in the way the beam spreads out as it propagates, the smaller the beam waist for the same wavelength the faster the size of beam waist changes with z (Figure 2.6).

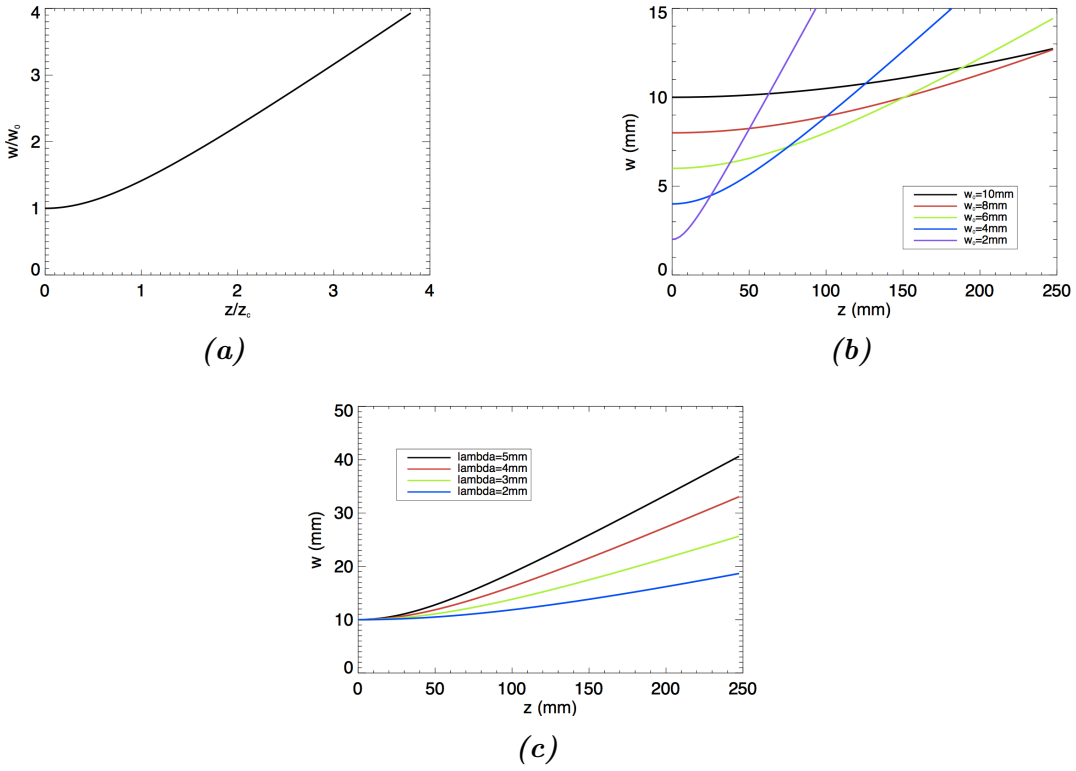

Figure 2.6: The beam-radius-to-beamwaist ratio as a function of the z-to-z_c ratio, where z_c is the confocal distance as defined above (a). The beam radius value along the propagation direction, z, for different values of the initial beam waist, w_0 at the fixed wavelength of 1 mm (b) and the beam radius value along the propagation direction, z, for different value of the wavelength, λ at the fixed beam waist of 5 mm (c).

Table 2.1 illustrates the field amplitude, intensity and phase at z = 0 for the first few positive values of the indexes l and p (for negative values of l the handedness of the phase front would be reversed).

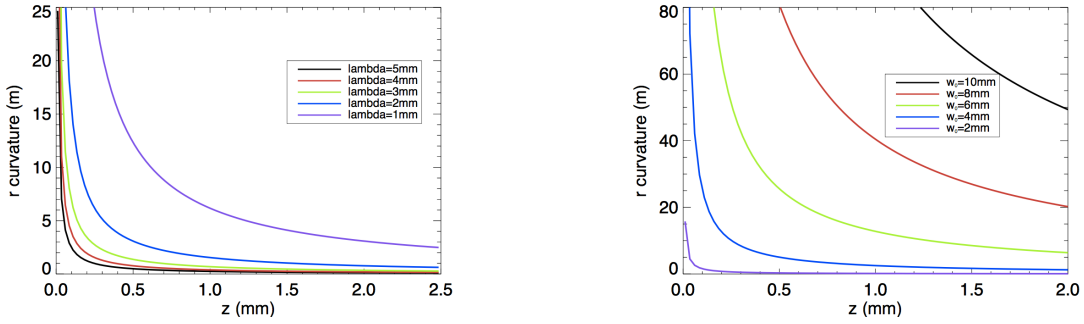

(a) *(b)*

Figure 2.7: Radius of curvature value along the propagation direction z for different values of the wavelength at a fixed value of the beam waist (a). Radius of curvature value along the propagation direction z for different values of the beam waist for a fixed wavelength (b).

In conclusion, it was known from ray optics that any tilted wavefront produces a non-zero orbital angular momentum component. It was not known until 1992, when Allen and his colleagues published their breakthrough paper [5], that in the particular case of Laguerre-Gaussian laser beams this momentum is found to be quantised. Specifically it assumes the value of $l\hbar$ per photon were l is the azimuthal index of the L-G mode (2.18) (as explained in detail in the following section). When the wavefront of a beam carrying OAM has a perfect spiral structure, i.e. when it is uniformly tilted around the propagation direction, a singularity is present on axis. In the aforementioned singularity the electromagnetic field intensity is zero and the phase is not defined. Light beams with the mentioned singularity are called *optical vortices* and are characterised by a central blind line along the propagation direction. Another peculiarity of pure OAM beams is the "doughnut" shaped intensity pattern. It can be seen in table 2.1 and 2.2 that the ring of maximum intensity is located at larger radii as the OAM number increases and that, for a certain mode, it becomes bigger along its propagation.

	Norm. Field Amplitude (a.u.)	Norm. Field Intensity (a.u.)	Field Phase (rad.)
LG_{00}	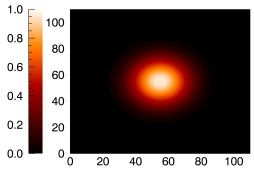	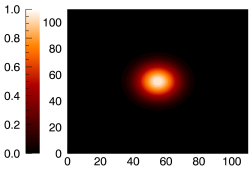	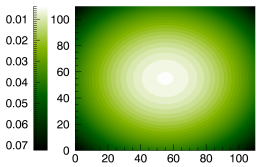
LG_{01}	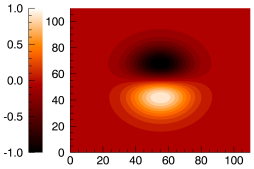	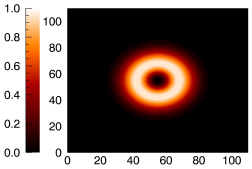	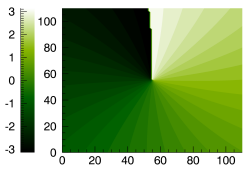
LG_{02}	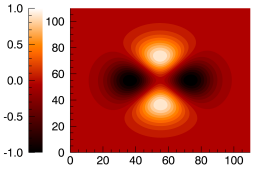	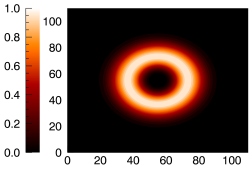	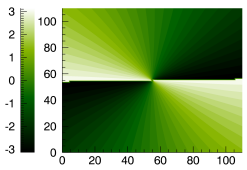
LG_{03}	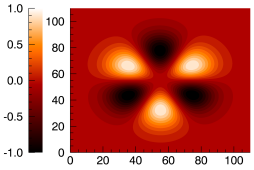	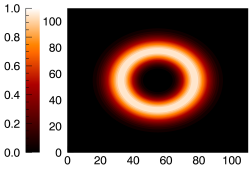	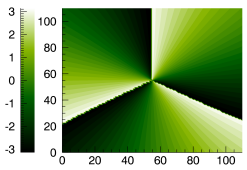
LG_{12}	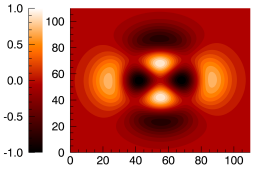	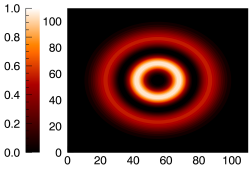	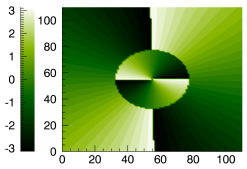
LG_{22}	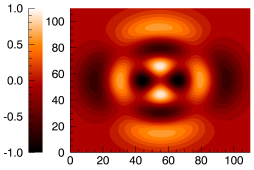	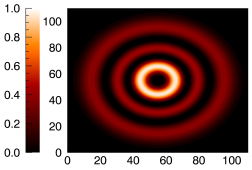	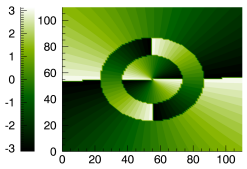

Table 2.1: Examples of L-G modes transverse amplitude, intensity and phase for different values of the indices p, l. The field distribution is calculated at $z = 0$ on the beam waist using the code described in Chapter 3.

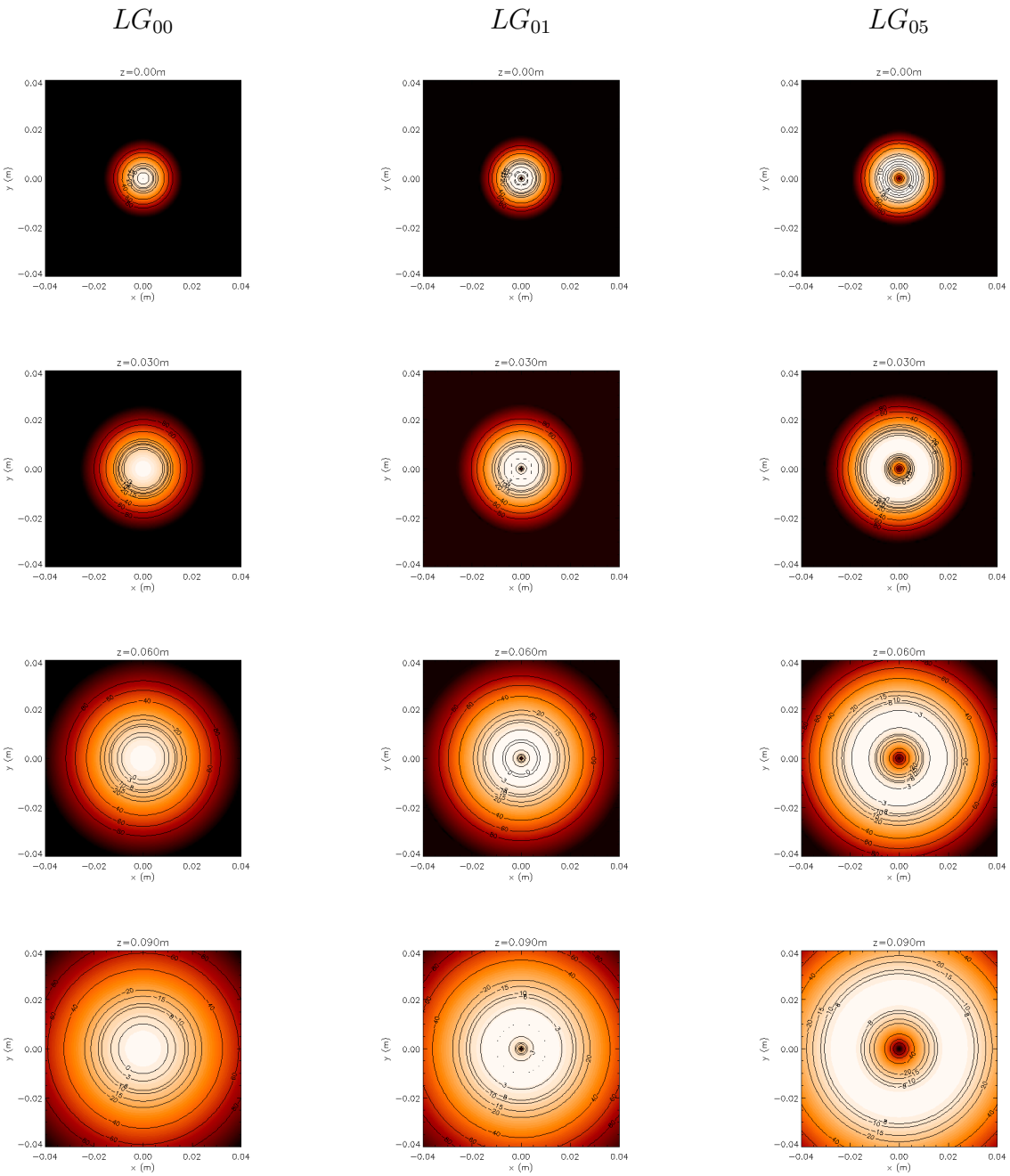

Table 2.2: Examples of L-G modes transverse normalised intensity through propagation along the z direction. The plots are generated using the code described in Chapter 3.

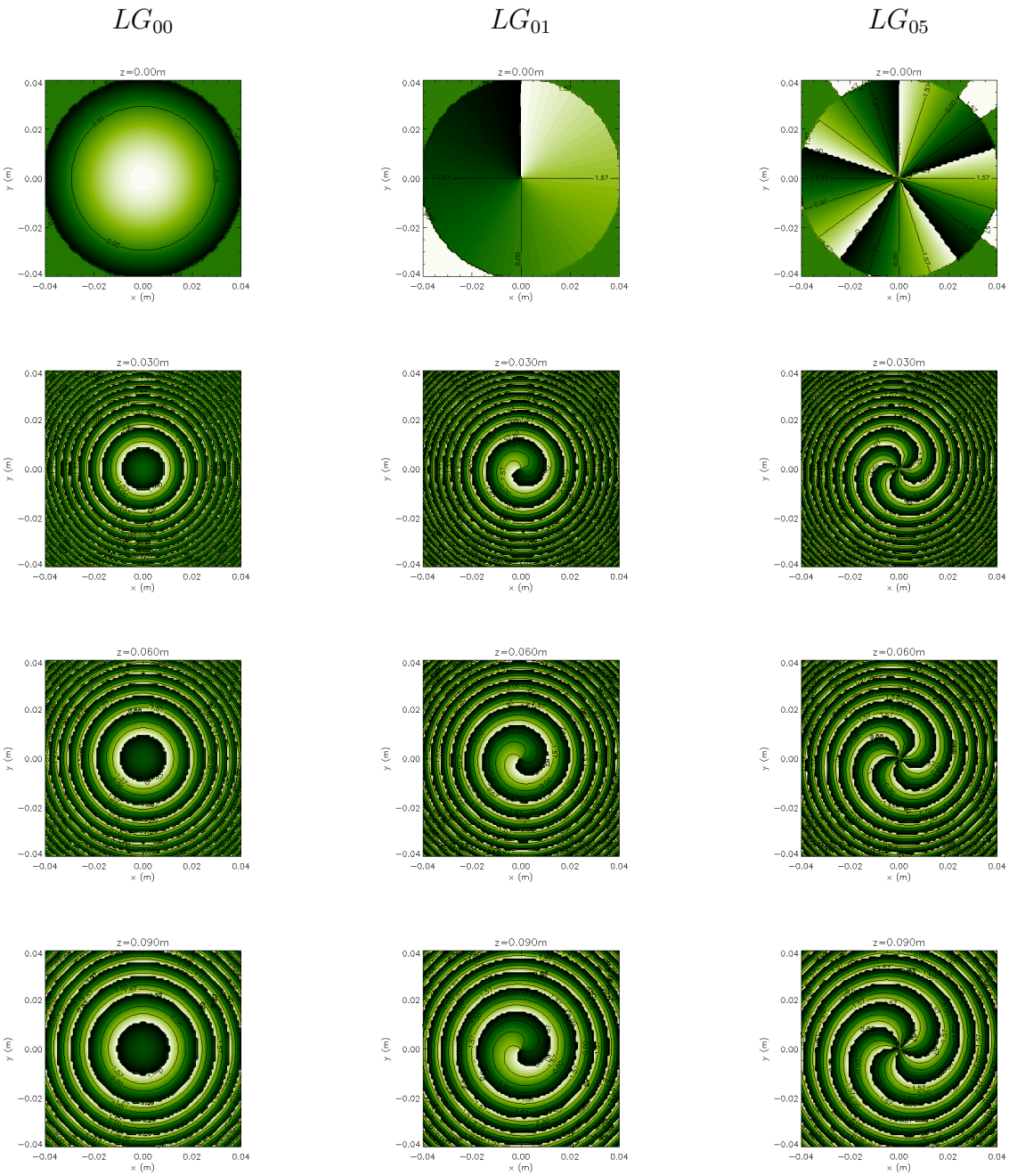

Table 2.3: Examples of L-G modes transverse phase through propagation along the z direction. The plots are generated using the code described in Chapter 3.

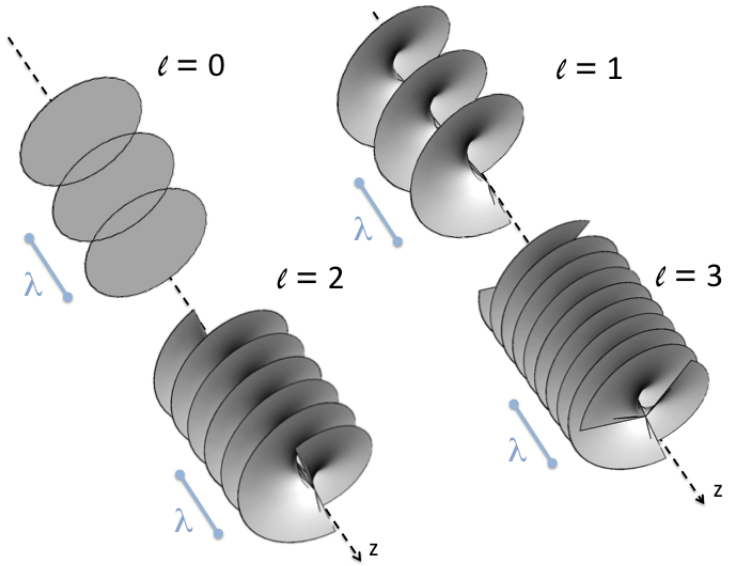

Figure 2.8: Equal-phase front of the first few positive OAM modes. As visible in the scheme, an imaginary straight line parallel to the propagation axis z would encounter the same phase value l times in the space of one wavelength.

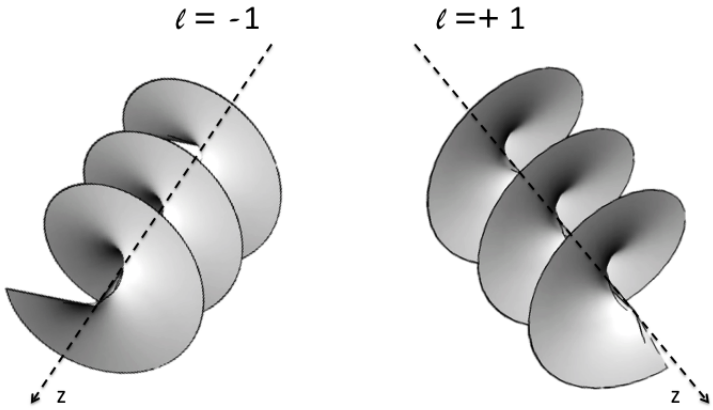

Figure 2.9: Mode $l = -1$ and $l = +1$ beam wavefronts. Changing the sign of the mode number means changing the handedness of the vortex.

Specifically, the maximum intensity radius is proportional to the square root of the mode number l as shown in equation (2.23).

$$R_l = w\sqrt{\frac{l}{2}}\,, \tag{2.23}$$

L-G modes are well suited to represent OAM carrying beams as they add the $\exp(il\phi)$ structure of the phase to the typical Gaussian description of light beams. The L-G description also fits with our work because the source and receivers in the experimental setups are millimetre wavelength feed horn antennas that are often modelled using this formalism. Moreover, the paraxial approximation applies to our experimental case.

It can be demonstrated that the total angular momentum of a single photon is

$$TAM = (\sigma + l)\hbar\,, \tag{2.24}$$

where σ, associated with the photon SAM can be only ± 1 and l, is related to the OAM state of the photon and can assume infinite integer values ranging between $-\infty$ to $+\infty$. The value l is generally called the *topological charge* of the beam. Moreover, the angular momentum to energy ratio is

$$\frac{J_z}{W} = \frac{l \pm \sigma}{\omega}\,, \tag{2.25}$$

where ω is the angular frequency.

The Laguerre-Gaussian modes formulation in (2.18) is not the only one used in optics. Another common one that is slightly different is

$$E_{p,l}(r,\phi,z) = \left[\frac{2p!}{\pi(p+l)!}\right]^{0.5} \frac{1}{w(z)} \left[\frac{\sqrt{2}r}{w(z)}\right]^{l} L_{p,l}\left(\frac{2r^2}{w^2(z)}\right)$$

$$\exp\left[\frac{-r^2}{w^2(z)} - ikz - \frac{i\pi r^2}{\lambda R(z)} - i(2p+l+1)\,\phi_0(z)\right] \tag{2.26}$$

$$\cos(l\phi)\,,$$

that features dark radial lines as well as dark concentric rings. Mathematically, these can be described simply by replacing the phase factor $\exp(il\phi)$ in equation (2.18) by a sine or cosine function as done in (2.26). These are called sinusoidal Laguerre-Gaussian modes and the lack the helicoidal phase front typical of the vortex beams. Instead, they have spherical phase fronts, just as the HermiteGauss modes.

The result of this difference in the phase dependence between the two sets of modes can be seen in their intensity pattern (see figure 2.10). While the helical L-G modes intensity pattern shows continuos intensity rings, the sinusoidal L-G modes intensity pattern features dark radial lines as well as dark concentric rings.

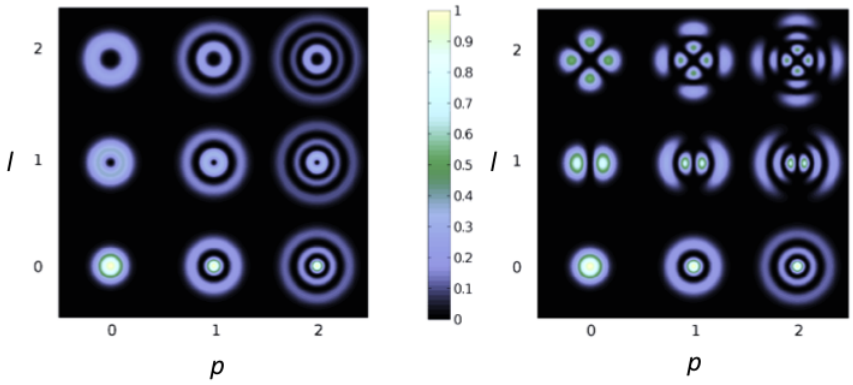

Figure 2.10: Intensity pattern of the helical L-G modes (left) and of the sinusoidal L-G modes (right) for the first radial and azimuthal indices p and l.

2.3 The Poynting vector

An important consequence of the equal-phase front having the described structure is the behaviour of the Poynting vector. The Poynting vector is always perpendicular to the wave front as it is defined, at each point in space, as by

$$\mathbf{S} = \mathbf{E} \times \mathbf{H} \,. \tag{2.27}$$

In a plane wave the instantaneous Poynting vector would always be oriented in the direction of propagation oscillating only in intensity. In the case of a collimated beam with helical wavefronts, instead, the vector would spiral around the direction of propagation thus giving rise to a non-zero component on the azimuthal plane in addition to the z component [53, 6].

(a) *(b)*

Figure 2.11: Normalized **E**, **H** and **S** vector scheme for a plane wavefront (a) and normalized **E**, **H** and **S** vector scheme for a spiral wavefront (b). The **S** is defined to be always perpendicular to the wave front. In the case of a spiral wavefront this means that the Poynting vector spirals around the z direction as the beam propagates.

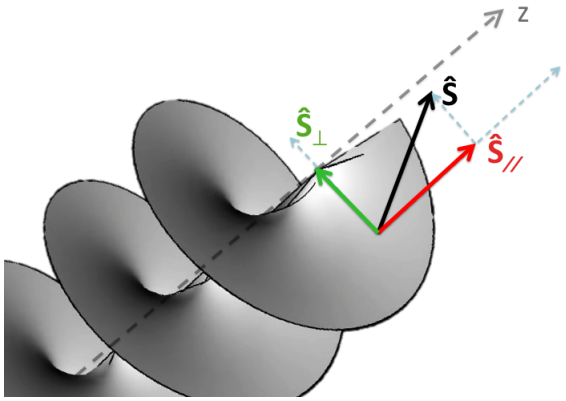

Figure 2.12: The Poynting vector associated with a spiral wavefront presents a component in the propagation direction and a component on the azimuthal plane.

The amount of rotation the Poynting vector of a helical L-G mode undertakes was calculated by Padgett and Allen in [53]. A radius that corresponds to a fixed point within the relative intensity distribution, that is the radius corresponding to the maximum intensity, was chosen and, for a L-G mode with $p = 0$ corresponds to

$$r_{I_{max}}(z) = \frac{\sqrt{2}\omega(z)}{2}\sqrt{l}\,. \tag{2.28}$$

The rotation of the Poynting vector varies with z as follows

$$\frac{\partial}{\partial z} = \frac{l}{2} \frac{\omega(z)}{r(z)}^2 \frac{z_r}{z_r^2 + z^2} . \tag{2.29}$$

which integrated to find the total Poynting vector rotation from the beam waist to a position z gives

$$\theta = \frac{l}{2} \frac{\omega(z)}{r(z)}^2 \arctan \frac{z}{z_r} . \tag{2.30}$$

If the maximum intensity radius expressed in (2.28) is substituted in (2.31) the total rotation is found to be

$$\theta = \arctan \frac{z}{z_r} . \tag{2.31}$$

2.4 PMDs for the generation of OAM carrying waves

It is possible to generate beams carrying orbital angular momentum through devices specifically designed to act on the wavefront and modify it in such a way that the outgoing wave would carry a vortex (see Chapter 1). The mode of the output vortex depends on the plate design and on the initial mode of the incoming beam. For the purpose of the project which was to investigate the design, production and performance of such devices at millimetre wavelengths, two devices were focused on: q-plates and SPPs. These are the easiest to make because at the required wavelengths,

dielectric materials' properties are easily exploitable, due to their low cost and the relative ease of machining them during the manufacturing process. The required $2l\pi$ phase shift around the axis of propagation can be achieved with a plate made of a material with a certain refractive index and with a thickness that varies helicoidally with the azimuthal angle. Such a device is called a Spiral Phase Plate (SPP) (see next section). Alternatively, it is possible to obtain the same effect of an azimuthally varying thickness using a flat slab of birefringent material where the geometry of the ordinary and extraordinary optical axes is designed such as the wave sees a resulting refractive index that varies on the transverse plane. Such a plate is called a q-plate. These devices can be used both to generate or detect light's OAM. Before looking at how the components were designed, a more detailed description of their working principle is required in order to understand their behaviour.

2.4.1 Spiral Phase Plates

The structure of a SPP is quite intuitively understandable as it consists of a slab of a chosen dielectric material with a defined refractive index n but with a thickness that varies proportionally with the azimuthal angle. The thickness variation of the plate is calculated to obtain a $2l\pi$ phase shift along a circle around the propagation axis as follows:

$$h = h_s \frac{\phi}{2\pi} + h_0 \,, \tag{2.32}$$

where h_0 is the initial thickness of the plate and h_s is the total thickness step (see figure 2.13 for an illustration of the plate) calculated as follows.

$$h_s = \frac{\Delta l}{\Delta n} \lambda \,. \tag{2.33}$$

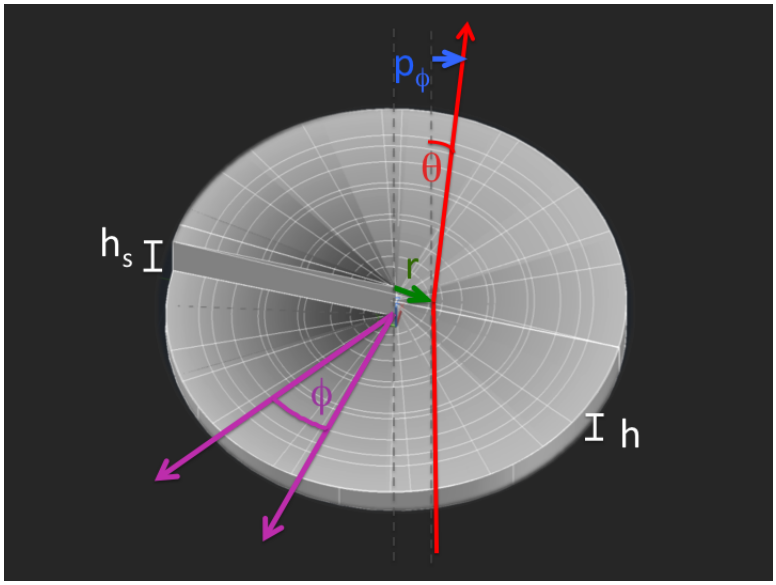

Figure 2.13: Coordinate and parameters scheme of a SPP. ϕ is the azimuthal coordinate, r the distance from the SPP's centre, θ is the angle by which the ray is diffracted and p_ϕ is the azimuthal component of the momentum. h_s is the step height and h is the SPP thickness at each point, as calculated in (2.32) and (2.33).

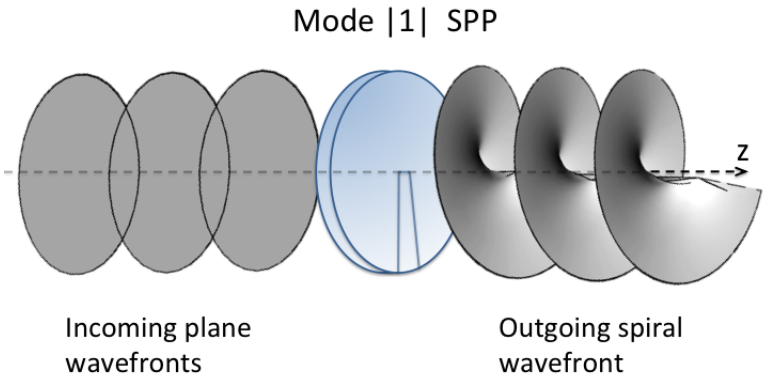

Figure 2.14: Representation of the light's wavefront change after interacting with a mode |1| SPP if the incoming radiation has a plane wavefront.

Assuming the incident beam's complex amplitude is $u(r, \phi, z)$, the amplitude after the plate will be $u' = u \exp(-i\Delta l \phi)$, where Δl is

$$\Delta l = \Delta n \, \frac{h}{\lambda} \, . \tag{2.34}$$

In the latter equation Δn is the difference between the SSP's refractive index and the one of the surroundings. At each point of the SPP surface, the phase delay imparted on the incoming radiation will then be

$$\Psi = \frac{(\Delta n) \, h_s}{\lambda} \, \phi \, . \tag{2.35}$$

Diffraction, due to the central dislocation, and consequent interference, are the cause for the appearance of the annular intensity pattern [13]. The SPP can be used to impart OAM on a Gaussian beam or to change the value of OAM carried by a L-G beam to the one of another L-G beam. The SPP, however, is not a pure mode converter. The SPP transforms an incoming fundamental Gaussian or L-G mode into a superposition of infinite L-G modes with coefficients that depend on the composition of the input beam and on the mode for which the SPP was designed [13].

As explained later in this chapter, the SPP effect is to apply a $\exp(il\phi)$ phase factor to the Gaussian amplitude of an incoming beam. The result does not correspond to any of the pure L-G modes of the basis that we use to represent vortex beams. This means that to be able to predict the propagation of the beam out coming from the SPP a modal decomposition is needed in order to find the coefficients indicating how much each mode contributes to the vortex beam. As reported in [13] the modal decomposition is performed through the following integral

$$c_{lp} = \int u \cdot u^*_{lp} d\phi \, . \tag{2.36}$$

It was also shown in [5] that the total OAM exchanged between the beam and the plate is

$$L \approx \hbar \, \frac{s \, \Delta n}{\lambda} \approx l\hbar \, . \tag{2.37}$$

The ideal SPP is one with a perfectly smooth variation of the thickness and a

perfectly sharp edge at the centre of the plate. That would be the most efficient, but it has been shown that a multilevel SPP can perform quite well assuming there is a reasonable number of steps-to-mode ratio. The choice, for a given required mode, between a smooth and a multilevel SPP depends on different factors such as plate performance, cost or size limitations in the manufacturing process.

2.4.2 q-plates

The q-plate is an inhomogeneous anisotropic plate first reported by Marrucci and colleagues in a paper in 2006 [41]. The working principle of the q-plate is slightly more complicated than for a SPP as it involves the polarisation. The structure of a q-plate is such that it locally behaves as a Half Wave Plate (HWP) but with a particular geometry of the optical axis. Since the plate acts as a HWP light with right/left circular polarisation will be converted to light with the opposite handedness polarisation. When this happens the SAM of the photons goes from ± 1 to ∓ 1 meaning that two units of angular momentum are transferred to the plate. If the geometry of the optical axes associated with the birefringence of the plate is designed as explained in the paper just mentioned these two units of angular momentum can be converted into OAM.

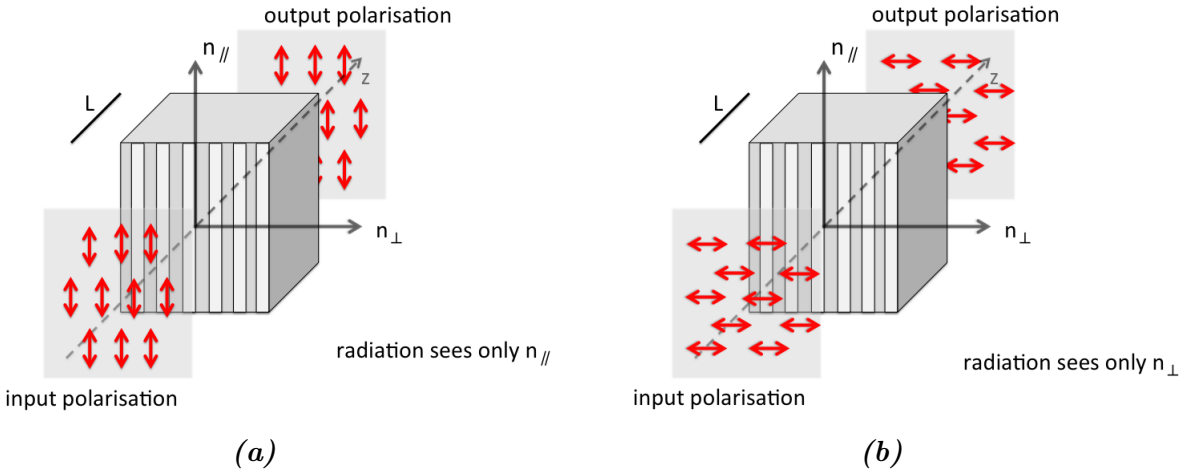

(a) *(b)*

Figure 2.15: Effect of the HWP on an incoming wave with polarisation parallel (a) and perpendicular (b) to the plate axis.

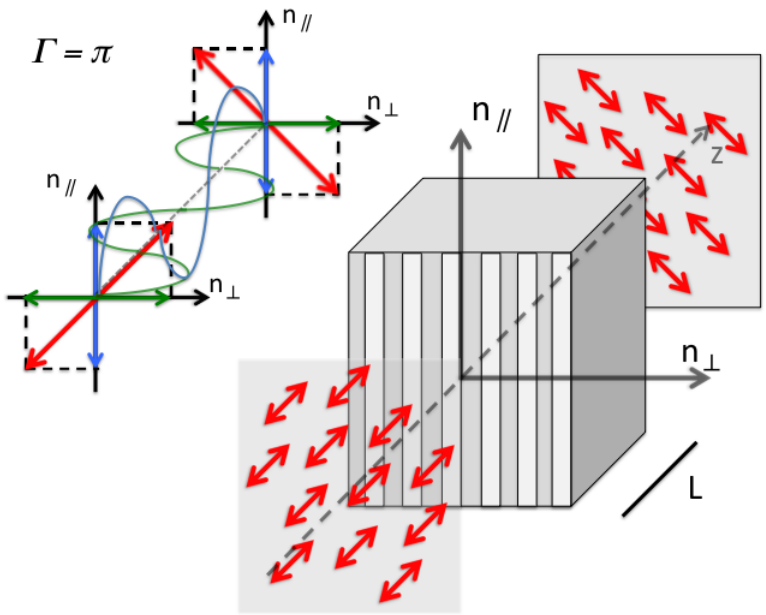

Figure 2.16: Effect of the HWP on a wave polarised at 45 to the plate's axis.

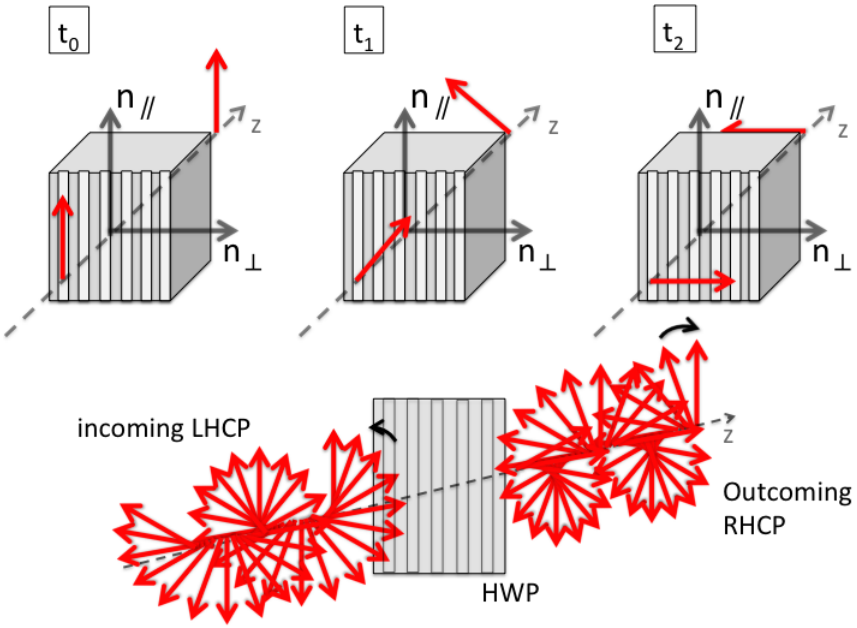

Figure 2.17: Effect of the HWP on an incoming circularly polarised wave.

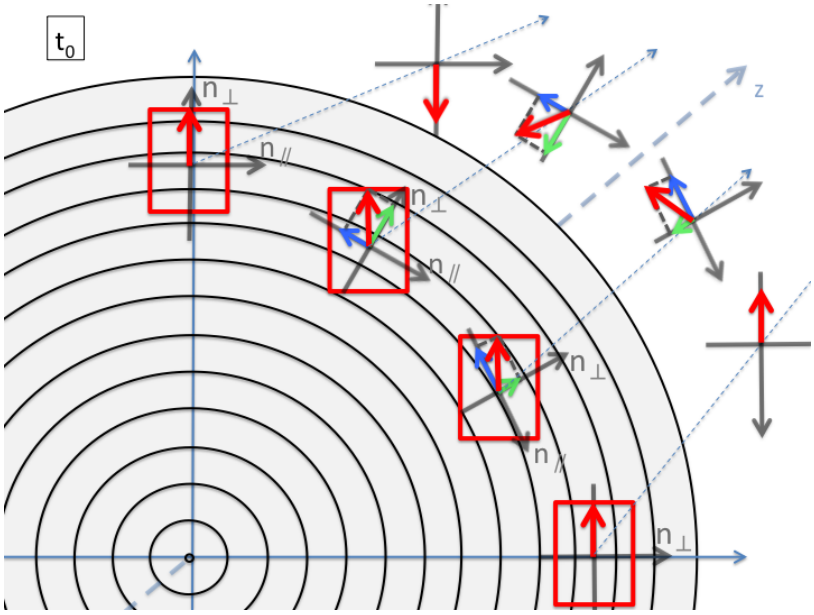

(a)

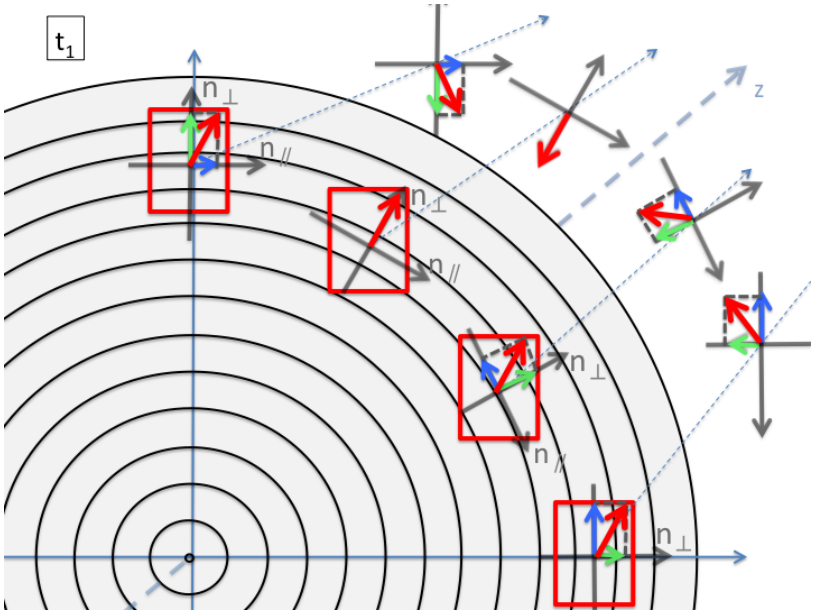

(b)

Figure 2.18: Incoming **E** vectors at t_0 and corresponding out coming vectors after interacting with the q-plate (a). It can be seen that the interaction locally corresponds to the interaction with a HWP oriented at different angles depending on the position on the azimuthal plane. In b) the same scheme at t_1.

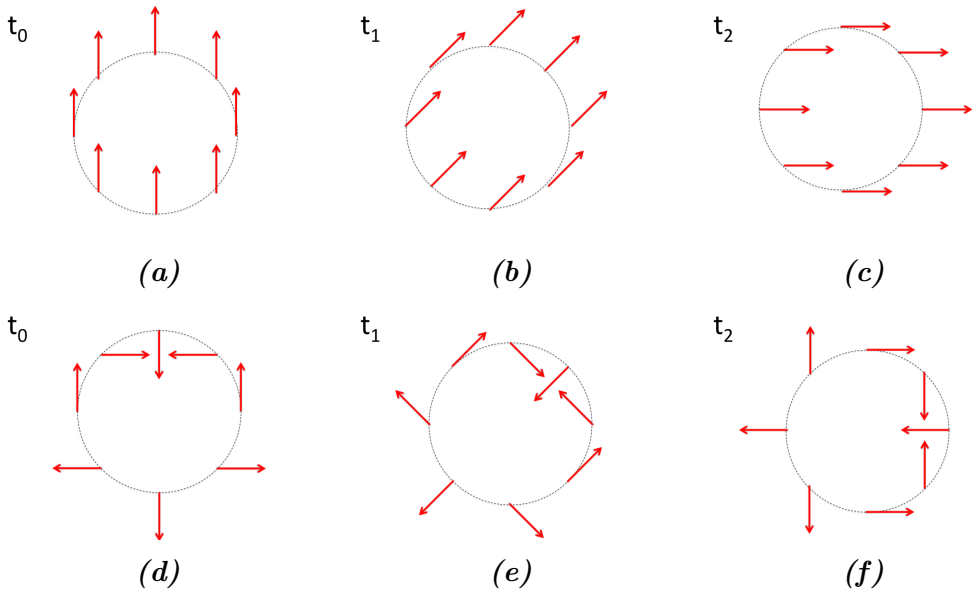

Figure 2.19: The **E** vector orientation on a circle around the propagation axis for the input wave at instant t_0 (a), t_1 (b) and t_2 (c) and the correspondent vectors after the interaction with the q-plate (d, e, f).

As an example, one of the two possible structures for a mode |2| q-plate shown in [41] (see figure 1.12) is looked at. This same structure was eventually manufactured to create a prototype dielectric q-plate. The concentric rings design was chosen for the manufacturing of the first prototype (see figure 1.14). This design requires more time for manufacturing and is more delicate as the space between the grooves is such that the material could melt during the cutting. However, this design is preferable compared to the radial one as it permit a higher precision on the central part which is vital for the good perform ance of the plates as it corresponds to the beam singularity. Cutting the radial grooves on a dielectric plate would result in an emptying of the central area compromising the working principle of the device.

The optical axis orientation across the plate's surface α is expressed by the following equation:

$$\alpha(r, \phi) = q\phi + \alpha_0 \tag{2.38}$$

where r and ϕ represent points in cylindrical coordinates on the transverse plane and q, α_0 are constants that depend on the Δl that the plate is required to impart on incoming radiation. The $\pm$ sign indicates the sense of rotation of the vortex and depends on the polarization of the incoming wave being either circularly right-handed (RHCP) or left-handed (LHCP) polarized. Specifically, the Jones matrix representing the mode q-plate is:

$$\mathbf{M} = \begin{bmatrix} \cos(2\alpha) & \sin(2\alpha) \\ \sin(2\alpha) & -\cos(2\alpha) \end{bmatrix} \tag{2.39}$$

where α is the quantity expressed in formula (2.38). Assuming an incoming LHCP wave, the transformation that it undergoes can be written as follows:

$$\begin{aligned} \mathbf{E_{out}} =& \mathbf{M} \cdot \mathbf{E_{in}} = \mathbf{E_0} \exp(\mathbf{i2}\alpha) \begin{bmatrix} 1 \\ -i \end{bmatrix} = \\ =& E_0 \exp(i2q\phi) \exp(i2\alpha_0) \begin{bmatrix} 1 \\ -i \end{bmatrix} . \end{aligned} \tag{2.40}$$

For the chosen design of the prototype, the two geometrical properties are defined to be $q = 1$ and $\alpha_0 = \pi/2$. Using the previous calculations for this specific case of a mode $|2|$ q-plate we obtain the following:

$$\alpha(r, \phi) = \phi + \frac{\pi}{2} \tag{2.41}$$

$$\mathbf{M} = \begin{bmatrix} \cos(2\,(\phi + \frac{\pi}{2})) & \sin(2\,(\phi + \frac{\pi}{2})) \\ \sin(2\,(\phi + \frac{\pi}{2})) & -\cos(2\,(\phi + \frac{\pi}{2})) \end{bmatrix} = \\ = \begin{bmatrix} \cos(2\phi + \pi) & \sin(2\phi + \pi) \\ \sin(2\phi + \pi) & -\cos(2\phi + \pi) \end{bmatrix}, \tag{2.42}$$

and since $\sin(\beta + \pi) = \cos(\beta)$ and $\cos(\beta + \pi) = -\sin(\beta)$ the matrix becomes

$$\mathbf{M} = \begin{bmatrix} -\sin(2\phi) & \cos(2\phi) \\ \cos(2\phi) & \sin(2\phi) \end{bmatrix}, \tag{2.43}$$

Assuming an incoming LHCP field $\mathbf{E_{in}}$, the following can be obtained

$$\begin{aligned} \mathbf{E_{out}} =& \mathbf{M} \cdot \mathbf{E_{in}} = \mathbf{E_0} \begin{bmatrix} -\sin(2\phi) & \cos(2\phi) \\ \cos(2\phi) & \sin(2\phi) \end{bmatrix} \cdot \begin{bmatrix} 1 \\ i \end{bmatrix} = \\ =& E_0 \begin{bmatrix} -\sin(2\phi) + i\cos(2\phi) \\ \cos(2\phi) + i\sin(2\phi) \end{bmatrix} = E_0 \begin{bmatrix} i\exp(i2\phi) \\ \exp(i2\phi) \end{bmatrix} = \\ =& E_0\, i\, \exp(i2\phi) \begin{bmatrix} 1 \\ -i \end{bmatrix} = \\ =& E_0 \exp(i\frac{\pi}{2}) \exp(i2\phi) \begin{bmatrix} 1 \\ -i \end{bmatrix} \end{aligned} \tag{2.44}$$

It can be seen from the calculation in (2.44) that the Jones vector representing the polarisation goes from LHCP to RHCP after the interaction with the q-plate. This is the expected result as it is known that the q-plate locally behaves as a HWP. The factor $\exp(i2\phi)$ also appears, that gives rise to the 4π phase change around the axis.

The **E** field vectors, the optical axis orientations and the α and α_0 angles are shown in the scheme in Figure 2.20.

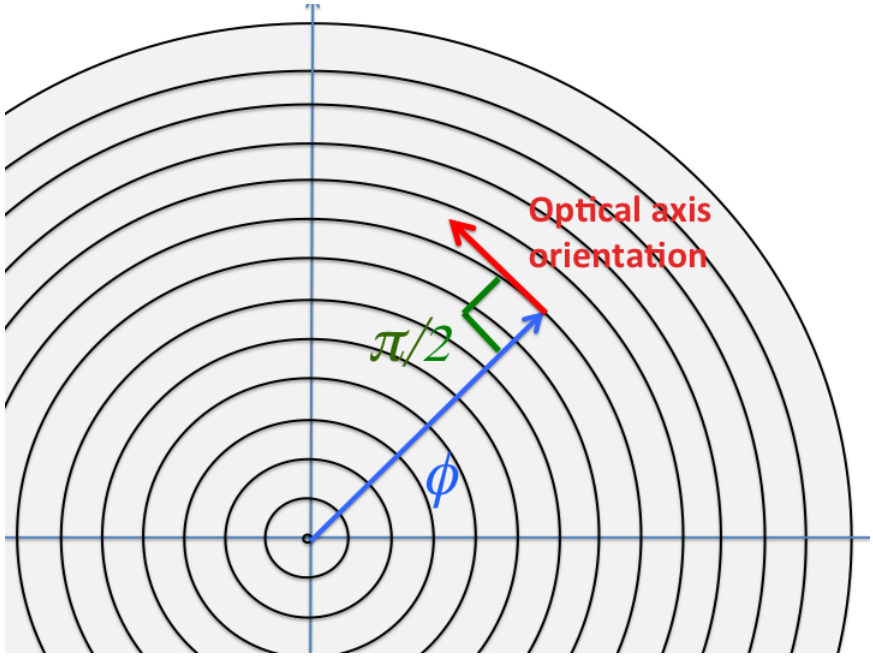

Figure 2.20: Optical axis orientation on a mode |2| q-plate as according to equation (2.41).

The required birefringence and the geometry of the optical axes can be achieved in different ways depending mainly depending on the frequency for which the plate will be used. In the visible and infrared regime liquid crystals are generally preferred as their orientation can be controlled by applying fields [62]. At longer wavelength other techniques such as dielectric engraving can be used as in the case of this work.

In the next Chapter we explain how the above described PMDs can be designed and manufactured at the millimetre wavelengths we are interested in.

Chapter 3

Simulations and design

"What I cannot create, I do not understand."
Richard Feynman

Outline

Understanding light's OAM is not as immediate as understanding polarisation could be. The topic doesn't have a long research history as SAM and circular polarisation have. Moreover, this project is the "first approach" to the topic our research group has undertaken. Consequently, it was useful and didactic to write a short code to reproduce plots of the propagation of L-G modes as described in Chapters 1 and 2. The code was also used to produce the images of the L-G modes and their propagation found in the previous chapters. In the present chapter it is shown how the code was constructed together with a few examples (Section 3.1). Moreover, in Section 3.2 I explain what are the principles to design and simulate the plates prior to production. Finally I report some information about the manufacturing process (Section 3.4).

3.1 Numerical representation and example plots (Intensity and Phase profiles)

In order to start visualising optical vortices and the associated L-G modes, they were simulated with the IDL programming language [21]. Using software specifically designed for simulations of realistic electromagnetic fields would be more effective than writing code in IDL. The Finite Element Analysis software HFSS [7] was used to check that the q-plate designed by Dr. Pisano was actually generating an OAM beam. The working principle for q-plates is somewhat more complicated than for SPPs and a reliable simulation was required before production. Software like HFSS, however, acts like a black box, providing the output fields of the modelled system. Choosing to first numerically represent the beam-plate interaction with my own IDL code had a didactic function. It was a way to understand the problem in a deeper way, facing all the doubts and problems that this topic presents. It is clear that the IDL code is nowhere as accurate as the finite element simulation.

The very first thing one can do is to calculate separately the pure L-G modes and have a look at the structure of their amplitude, intensity and phase in order to better understand their properties.

The set of L-G modes in Equation (2.18) and recalled here in (3.1) represents the 3D distribution of the field in cylindrical coordinates r, the distance from the propagation axis on the azimuthal plane, ϕ, identifying the angle on the azimuthal plane and z, the distance from the beam waist along the propagation direction. L_p^l is the correspondent generalised Laguerre polynomials as expressed in equation (2.19), p is the radial index and l is the azimuthal index.

$$E_{p,l}(r,\phi,z) = \left[\frac{2p!}{\pi(p+l)!}\right]^{0.5} \frac{1}{w(z)} \left[\frac{\sqrt{2}r}{w(z)}\right]^{l} L_{p,l}\left(\frac{2r^2}{w^2(z)}\right)$$
$$\exp\left[\frac{-r^2}{w^2(z)} - ikz - \frac{i\pi r^2}{\lambda R(z)} - i(2p+l+1)\,\phi_0(z)\right] \tag{3.1}$$
$$\exp\left(il\phi\right),$$

The IDL code set up a 2D grid where the size and density of points (i.e. the resolution) that could be modified by the user. Each point on the grid corresponds to a pair of coordinates (r, ϕ) and one grid can be calculated at any value of z along the propagation axis. These coordinates are then inserted in Equation 2.18 and the complex value for the field is calculated and stored in that position of the grid. The 2D array is also calculated for some value of the l and p indices, which I recall define the number of nodes along the radius and along a circle around the propagation axis, from 0 up to the desired threshold. The result is a 2D array where each position is identified by the l, p indices and contains another 2D array where each position is identified by the coordinate on the azimuthal plane, in our case (x, y) for convenience. This contains the complex value of the field storing the information about the field amplitude and phase, as shown in Figure 3.1.

Before doing any calculation on the field, plots of the amplitude, the intensity and the phase of different modes were made and compared with the corresponding fundamental beam. The values for the wavelength λ and the beam waist w_0 were chosen so that could be easily achieved in the laboratory setting. They were: $\lambda = 3\,\mathrm{mm}$ and $w_0 = 5\,\mathrm{mm}$.

A change in the wavelength or in the beam waist means a change in the way the beam spread out as it propagates, the smaller the beam waist for the same wavelength the faster the size of beam waist changes with z (Figure 2.7).

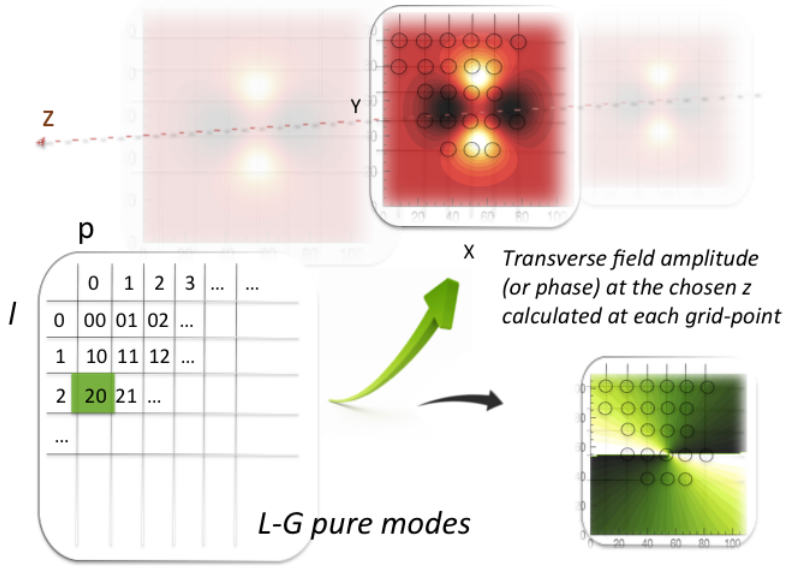

Figure 3.1: Illustration of the basis of the numerical simulation. In each position of the 2D array representing the first some L-G modes another $n \times n$ array is stored. This grid represents the transverse plane $x - y$ at a chosen distance z from the beam waist along the propagation direction of the L-G beam . At each node of this grid the field is calculated implementing the right x, y and z in the L-G modes equation (2.18).

Table 2.1 illustrates the field amplitude, intensity and phase on the beam waist for a few values of the indexes l and p.

Table 2.2 shows the mode $|1|$ beam as an example to visualise its behaviour through propagation, thus changing the value of z at which we calculate the grid.

Both figures were created with this code.

Having shown how the single modes behave, a more complex and realistic situation in which there is a beam propagating and interacting with a phase plate i.e. either a q-plate or a SPP can be studied. To do so an origin for the beam waist of the incident beam was chosen. For simplicity, the beam was set to be LG_{00}. After deciding at which point of the propagation the beam encounters the phase plate, the field grids at that z are calculated and then multiplied by the phase factor imparted on the radiation by the plate at that point on the azimuthal plane. The result is a grid with

new values of the field at the position after interaction with the plate. This is no longer one of the pure LG modes and cannot be "propagated" by the code as was carried out on the fundamental mode.

The computed fields are then "decomposed" into a set of pure modes of the LG array and the coefficients that indicate how much of each mode is contributing to the output field are calculated.

This calculation is expressed by the equation (3.2), adapted here to the discrete case (3.3), as there are only a limited number of points on a grid.

$$c_{lp} = \int u \cdot u^*_{lp} d\phi \,. \tag{3.2}$$

Considering the discrete grids the integral in 3.2 becomes

$$c_{lp} = \frac{1}{N} \sum_{l,p=0}^{n} u \cdot u^*_{lp} \,, \tag{3.3}$$

with N being the number of points on the grid at which the field is sampled.

Before using the code to simulate other beams, such as superpositions of modes or beams interacting with more than one plate, the code's ability to correctly calculate the c_{lp} needed to be verified. To do so the calculated results for a fundamental LG_{00} passing through a mode 1 SPP were compared with the ones known from an existing publication [13]. For a LG_{00} passing through a mode 1 SPP the values obtained for the first few values of the index l and the index p are reported in the following table (3.1) together with the ones from Beijersbergen's paper [13].

LG mode	Beijersbergen	Our simulation
LG_{10}	78.5	79.05
LG_{21}	9.82	9.73
LG_{32}	3.68	3.59
LG_{43}	1.92	1.84
LG_{54}	1.17	1.11
LG_{65}	0.79	0.73

Table 3.1: Mode contents (relative intensity percentage) of a mode LG_{00} after passing through a $\Delta l = 1$ SPP

Having double-checked the part of the code that calculates the coefficients, I can use it as a tool to reconstruct any generic beam (even not pure L-G modes) at any stage of the optical path. Any optical element that involves the polarisation of the radiation will be represented with the Jones formalism where two component vectors are used to keep record of the X and Y-components of the field e.g. in the case of a setup involving a q-plate where quarter wave retarders are needed to convert linearly polarised to circularly polarised radiation.

For example, the simulation shown in figure 3.3 is computed starting with a Fundamental Gaussian mode circularly polarised. The LG_{00} mode then passes through a mode $|1|$ q-plate where it acquires OAM and finally goes through a horizontal linear polarisers. The generated beam can be decomposed on the L-G modes basis and the coefficients representing the contribution of each mode to the beam can be determined.

Recalling the equations (2.39) and (2.40) to determine the q-plate matrix and the out coming beam, the mentioned optical path can be represented as follows:

$$\mathbf{E_{out}} = \begin{bmatrix} 1 & 0 \\ 0 & 0 \end{bmatrix} \cdot \mathbf{M_q} \cdot \mathbf{E_{0,0}}(\mathbf{r}, \phi, \mathbf{z}) \cdot \begin{bmatrix} 1 \\ -i \end{bmatrix} = \mathbf{E_{0,0}} \exp(\mathbf{i}\phi) \begin{bmatrix} 1 \\ 0 \end{bmatrix} , \tag{3.4}$$

where the polarisation and polariser vectors are defined by the Jones' formalism.

In the case of elements or lenses refocusing the beam, thus recreating a beam waist of a different size and location, ray transfer matrix analysis is used. With this method, knowing the position and size of the input beam waist, the wavelength and the type of device (thin slab, thick slab, thin lens etc.) it is possible to determine an ABCD matrix that would allow the extrapolation of the new beam waist position and size.

Here are reported some examples of this kind of simulation together with their calculated modes content.

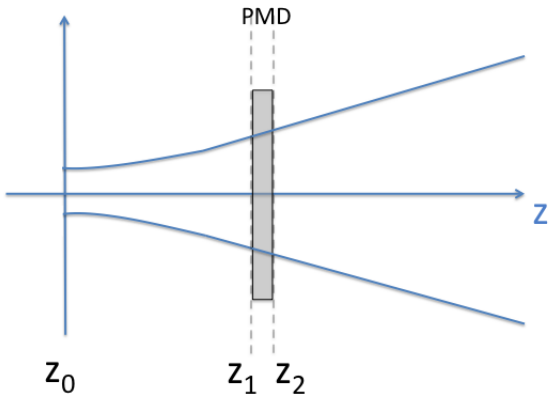

Figure 3.2: Scheme of the simulated configuration when only the PMD is inserted in the beam's path.

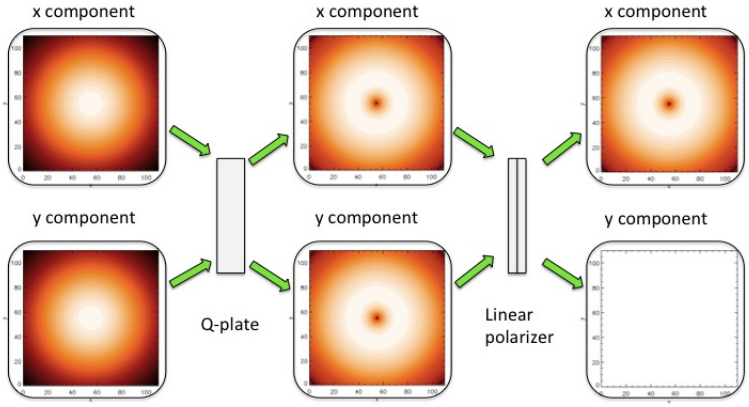

Figure 3.3: Example of IDL numerical simulation where the x and y polarisation components are represented. The incoming beam is a fundamental Gaussian beam circularly polarised (for the q-plate to work). We check the mode contents of the beam after passing through the q-plate and then through a linear polariser.

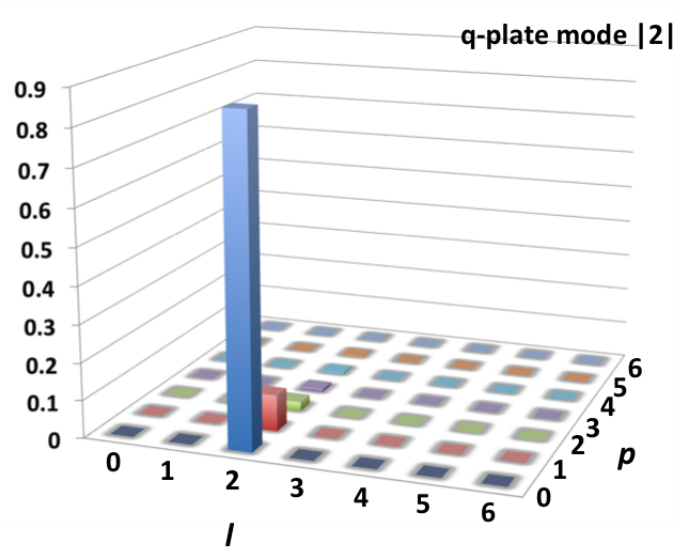

Figure 3.4: OAM spectrum of the beam generated by the configuration in figure 3.3. The coefficients of the modes are calculated using custom code.

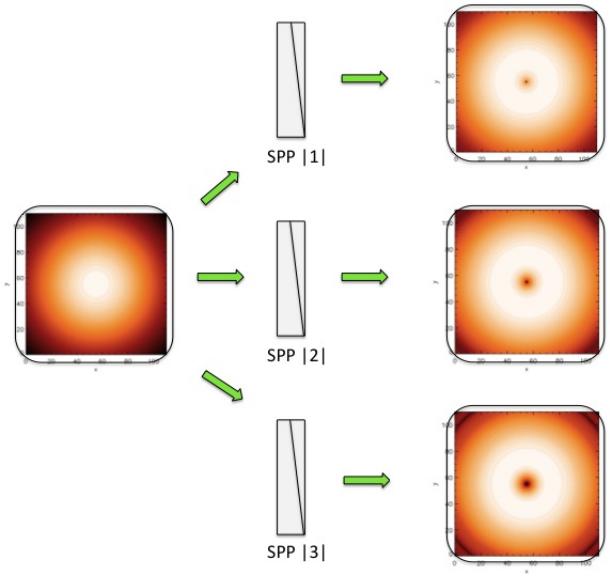

(a)

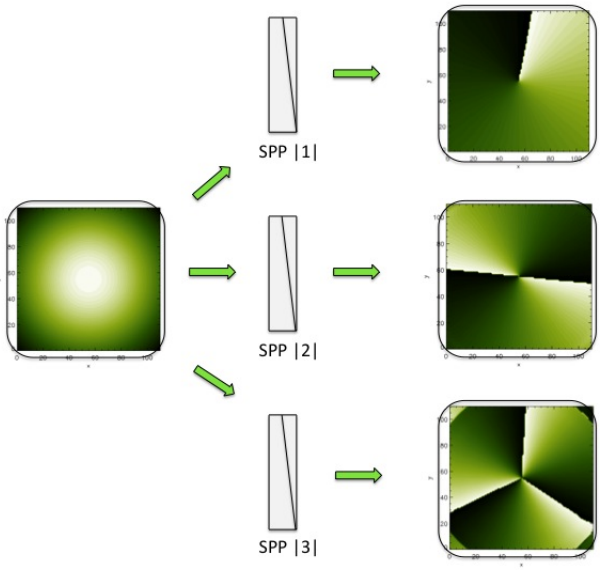

(b)

Figure 3.5: Example of IDL numerical simulation. The incoming beam is a fundamental Gaussian beam linearly polarised. We check the mode contents of the beam in three different cases: after passing through a mode |1| SPP, a mode |2| SPP and a mode |3|. The transverse field is plotted in both intensity (a) and phase (b).

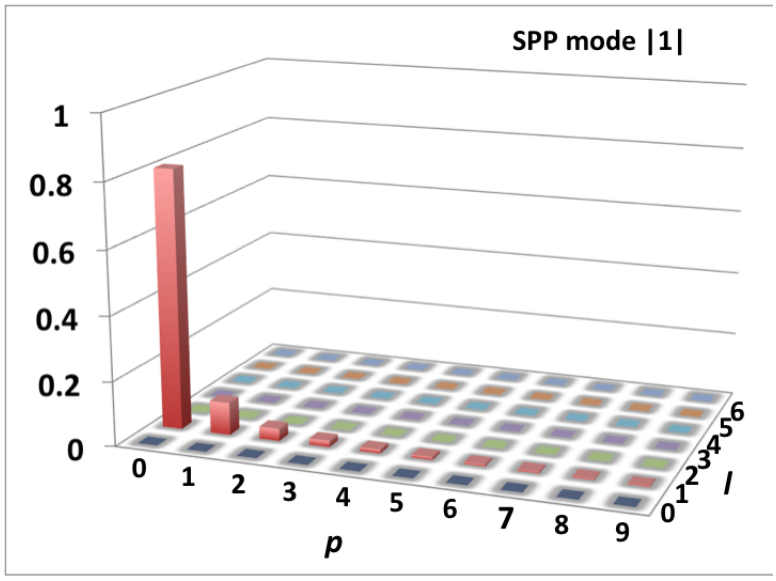

Figure 3.6: OAM spectrum of the beam generated by the SPP mode |1| as in figure 3.5. The coefficients of the modes are calculated using custom code.

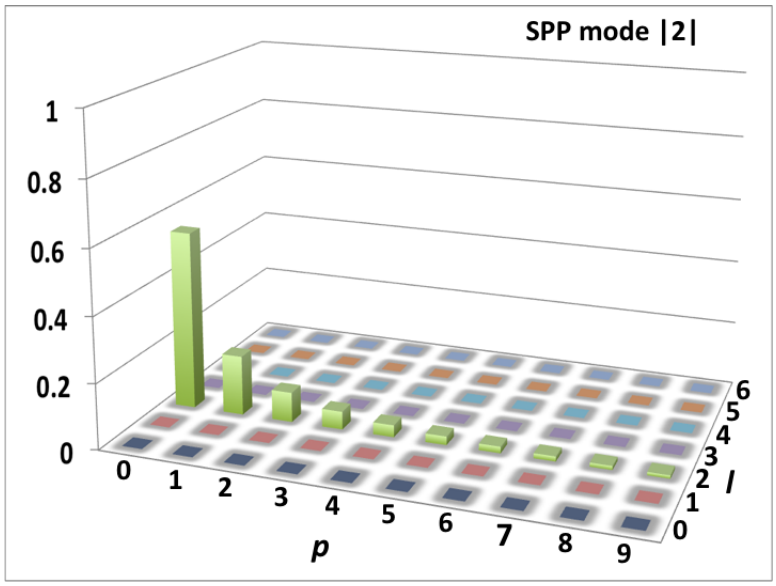

Figure 3.7: OAM spectrum of the beam generated by the SPP mode |2| as in figure 3.5. The coefficients of the modes are calculated using custom code.

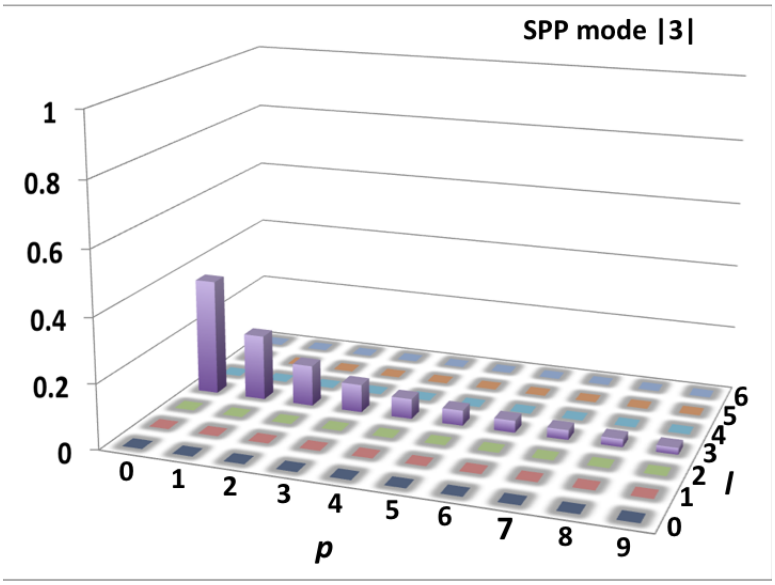

Figure 3.8: OAM spectrum of the beam generated by the SPP mode |3| as in figure 3.5. The coefficients of the modes are calculated using custom code.

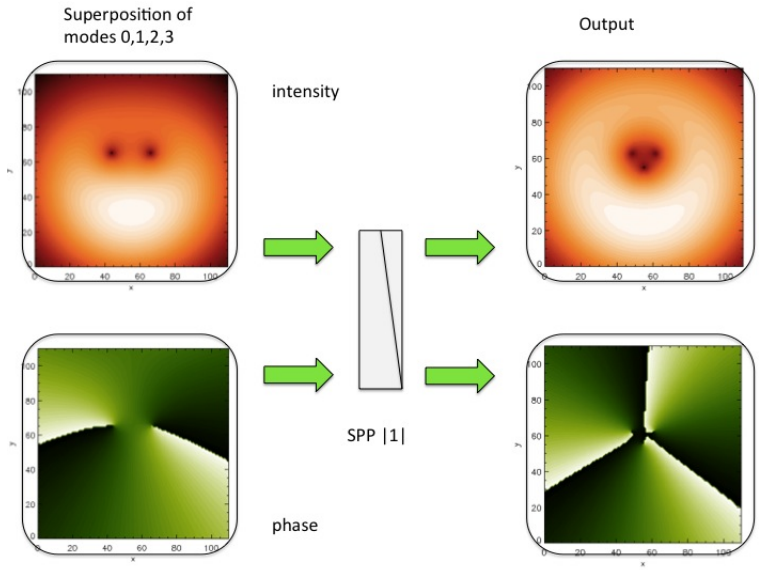

Figure 3.9: Example of IDL numerical simulation (intensity and phase). The incoming beam is a superposition of modes 0,1,2 and 3. The beam then passes through a SPP mode |2| and the mode content of the output is calculated.

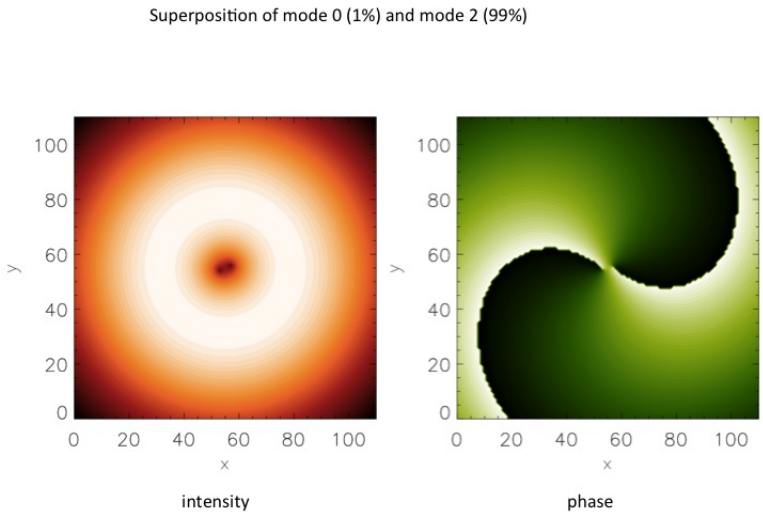

Figure 3.10: Example of IDL numerical simulation of the transverse intensity and phase of a superposition of mode 0 and 2 OAM beams.

An additional comment on figure 3.10 is needed. What is represented in the plot just mentioned could explain the double inner vortex that can be seen in the measurements performed with the 3D scanner presented in the next chapter. The plate is not expected to be 100% efficient causing part of the beam not to be converted to a vortex. These effects will be further investigated and studied both theoretically and experimentally in the near future.

3.2 The Design of the Plates

Within this work, 4 different types of SSP were designed and tested. A q-plate that was designed by Dr. Pisano was also tested and compared to data from a Finite Element simulation. Specifically, the plates are:

1. a $|\Delta l| = 2$ q-plate
2. a $|\Delta l| = 1$ SPP with a smooth surface
3. a 16 wedge $|\Delta l| = 1$ SPP

4. a 32 wedge $|\Delta l| = 2$ SPP

5. a $|\Delta l| = 2$ wedge SPP with a split ramp

Here in the following sections we look at how in practice such devices for millimetre wavelengths are designed.

3.2.1 q-plate design

It has been theoretically shown that sub wavelength gratings of dielectric materials can act as homogeneous birefringent plates [22] at optical wavelengths. In order to avoid diffraction, the grating periodicity must also be smaller than $\lambda/2$, where λ is the wavelength of the incident radiation. All the grating parameters, such as the thickness t, the period p and the opening-to-period ratio q, are functions of λ. Given the refractive index n of the material and that of its surroundings (usually air, $n = 1$) it is possible to derive the birefringence Δn from simple formulas describing $n_{\parallel}$ and $n_{\perp}$, where the former is the refractive index as seen by linearly polarised light parallel to the grooves and the latter in the orthogonal direction. Therefore, for example, the thickness can be chosen to be $t = \lambda/(4\Delta n)$ in order to obtain a quarter-wave plate, or $t = \lambda/(2\Delta n)$ for a HWP [22]. A portion of the structure of such gratings is shown in Figures 3.11 and 3.12.

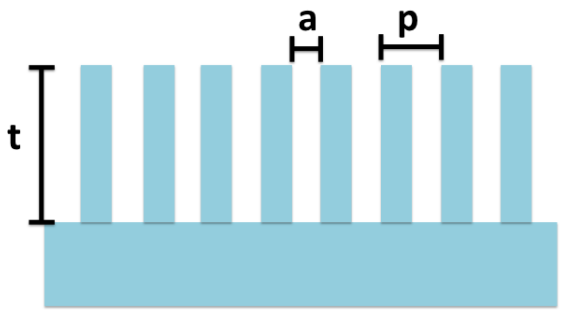

Figure 3.11: The geometrical parameters t, p and a of the diffraction grating.

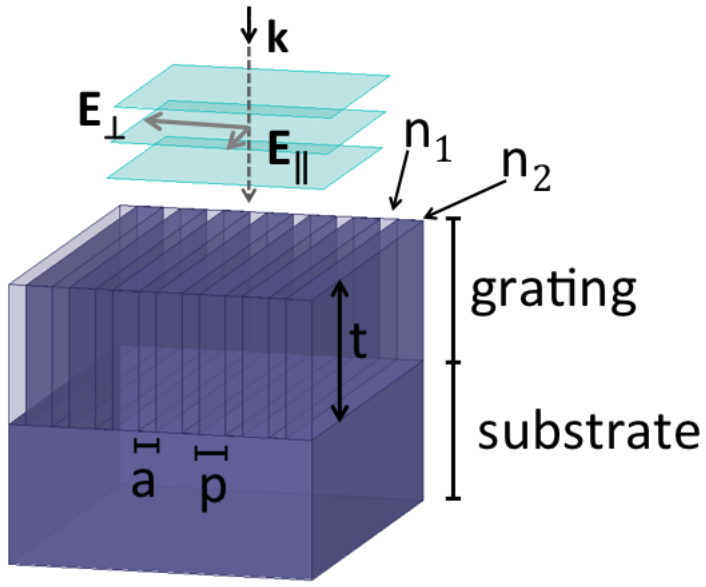

Figure 3.12: Illustration of the birefringent grating structure. Zones with two different refractive indexes, n_1 usually being equal to 1 (air), alternate with a ratio and a periodicity that determine the effective refractive indexes experienced by the two components of an incident electromagnetic wave parallel and perpendicular, respectively to the grating grooves.

This principle was used to design a $\Delta l = \pm 2$ q-plate by changing the orientation of the birefringence optical axis according to the recipes formulated by Marrucci et al. [41]. The practical realisation of the q-plate consists of carving concentric rings in a dielectric material disc using the thickness, the periodicity and the depth values previously calculated for the homogeneous HWP. The first q-plate prototype was made of Nylon ($n = 1.73$ at room temperature) and optimised to work at the frequency of 100 GHz. The plate parameters, reported in Table 3.2, were initially calculated using the formulas given by Dale C. Flanders [22] and then optimised by using finite element analysis software (Ansoft HFSS by Ansys). Specifically the parameters can be calculated as follows:

$$n_{\parallel} = [n_1^2 + n_2^2(1-q)]^{\frac{1}{2}} \tag{3.5}$$

$$n_{\perp} = [(1/n_1^2)q + (1/n_2^2)(1-q)]^{-\frac{1}{2}} \tag{3.6}$$

$$\Delta n = n_{\parallel} - n_{\perp} \tag{3.7}$$

$$\Gamma = \frac{2\pi\Delta n L}{\lambda_0} \tag{3.8}$$

where Γ is the resulting relative phase shift between the two perpendicular field components. Considering our specific case we have $n_1 = 1$ and $n_2 = 1.73$ giving $n_{\parallel} = [3.99 - 2.99q]^{1/2}$ and $n_{\perp} = [0.34 + 0.66q]^{-1/2}$. By plotting Δn versus q a suitable value for q may be chosen. The chosen value must satisfy the conditions that $P<\lambda/2$ and that it can produce the π phase shift required for our plate (as expressed in equation 3.8). Additionally the thickness L of the slab should be low to limit the absorption. It can be seen on the graph in figure 3.13 that a higher level of birefringence could have been achieved but physical factors limited the available choices. The chosen value for q was dictated by the milling tool size as there was not a possibility of going smaller than 0.5 mm. The reason for that being the fragility of the tool itself and the difficulty in handling thin slices of Nylon as the heat from the milling would bend it.

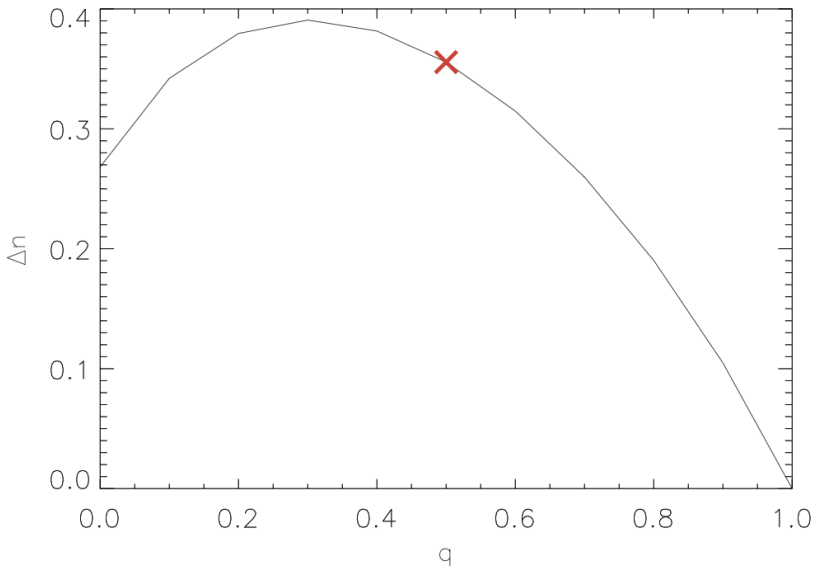

Figure 3.13: Artificial birefringence as a function of the opening-to-period ratio, q.

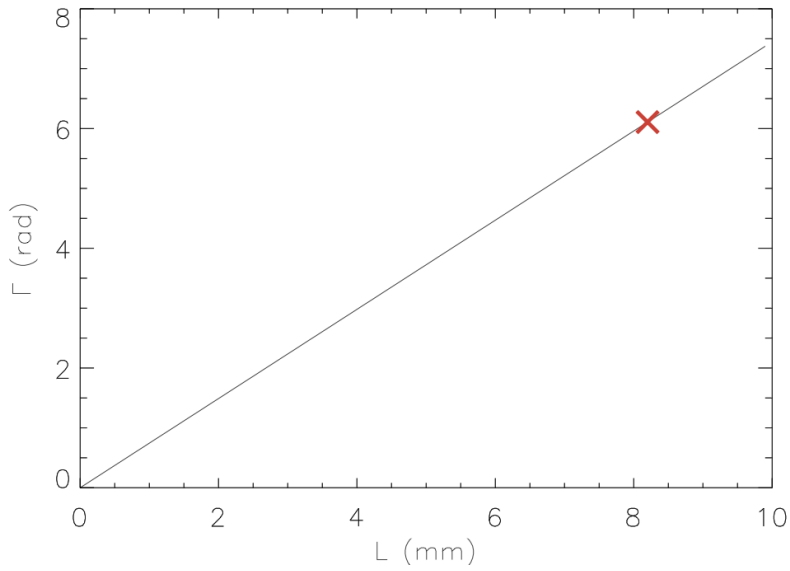

Figure 3.14: Induced phase-shift for the chosen q for different thicknesses. The red cross indicates the point on the curve at which a 2π phase shift required for a HWP is achieved. This value for the phase shift corresponds to a thickness of 8.2 mm.

Because of the impossibility of creating a self-sustained grating the design includes an intermediate layer of Nylon whose thickness is calculated as follows in order to be matched with the wavelength (see figure 3.15).

$$d = \frac{\lambda}{2n} \tag{3.9}$$

The total depth of the grooves required for the thickness was reached by milling half of it on both sides of the supporting layer of Nylon.

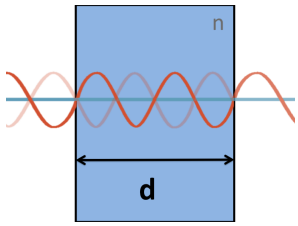

Figure 3.15: Matching condition for a slab of material of refractive index n. The distance is calculated so that the reflected wave that propagates inside the material is out of phase with the reflected wave from the first surface.

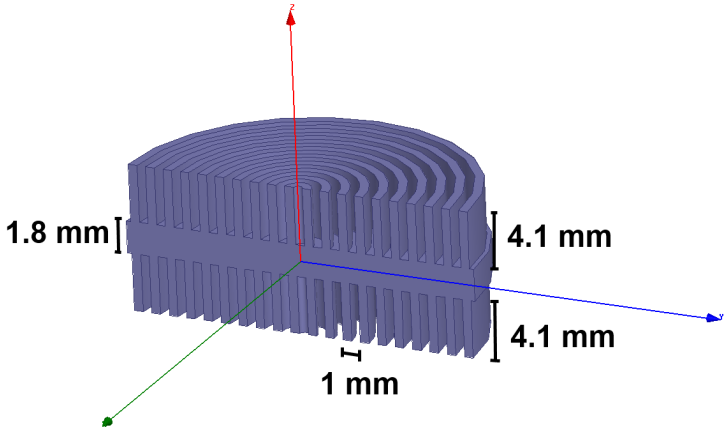

Figure 3.16: Section of the prototype q-plate along the diameter. The grooves total depth required to make the slab of nylon birefringent was reached digging half of the depth on both sides of a central matched thickness.

Nylon mode |2| q-plate	
Plate diameter	110 mm
Total thickness	10 mm
Inner layer thickness	1.8 mm
Grating period	1 mm
Space-to-period ratio (q)	1/2
Grooves depth (t/2)	4.1 mm

Table 3.2: q-plate geometrical parameters.

The q-plate geometrical parameters are reported in table 3.2.

3.2.2 SPPs design

The SPPs were designed to use and manufactured with a different material than the q-plate: Polypropylene instead of Nylon. Polypropylene, whose refractive index is lower than that of Nylon, has other better characteristics in terms of lower absorption at the frequencies of interest. The two materials' absorption coefficients are compared in figure 3.17.

Knowing that the refractive index of Polypropylene is $n = 1.5$ and that the plate should work at a frequency of 100 GHz the required height of the step of the SPP can be calculated from (2.33).

For a $|\Delta l| = 1$ SPP that means

$$h_{s_1} = \left(\frac{1}{\Delta n}\right)\lambda = \frac{0.003}{0.5} = 0.006\,\mathrm{m} \tag{3.10}$$

while for a $|\Delta l| = 2$ we have

$$h_{s_2} = \left(\frac{2}{\Delta n}\right)\lambda = \frac{0.006}{0.5} = 0.012\,\mathrm{m} \tag{3.11}$$

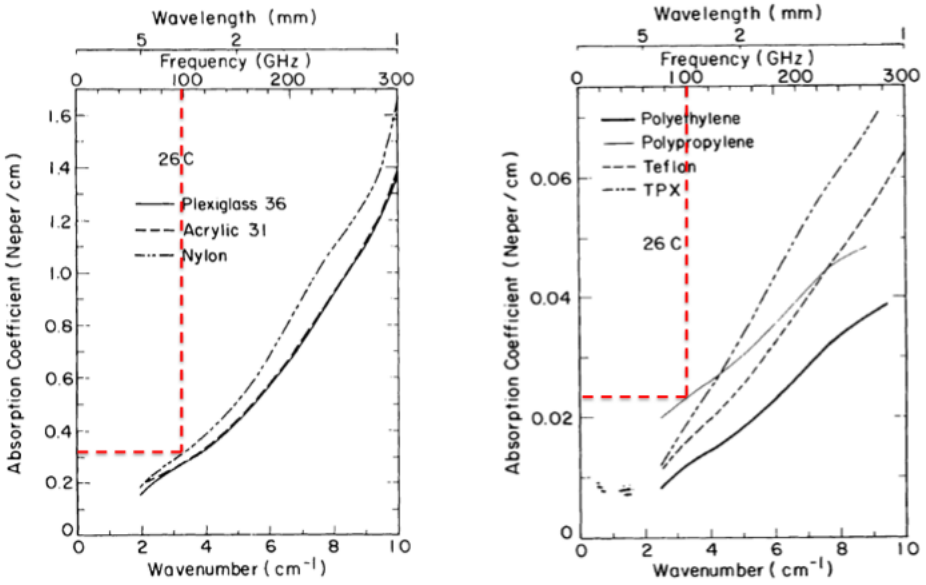

Figure 3.17: Absorption coefficient for Nylon (left graph) and Polypropylene (right graph) as reported in [4].

Knowing that the refractive index of Polypropylene is $n = 1.5$ and that the plate should work at a frequency of 100 GHz the required height of the step of the SPP can be calculated from (2.33).

For a $|\Delta l| = 1$ SPP that means

$$h_{s_1} = \left(\frac{1}{\Delta n}\right)\lambda = \frac{0.003}{0.5} = 0.006\,\mathrm{m} \tag{3.12}$$

while for a $|\Delta l| = 2$ we have

$$h_{s_2} = \left(\frac{2}{\Delta n}\right)\lambda = \frac{0.006}{0.5} = 0.012\,\mathrm{m} \tag{3.13}$$

One can design the smooth mode ± 1 SPP using equation (2.32) to determine the thickness of the plate at each point on the surface adding a base layer as a support with a matched thickness (so that reflections are out of phase and cancel out) calculated in the following way and increased by doubling the matched thickness

maintaining the matching condition in order to be handled by the workshop machines during manufacturing.

$$d = \frac{\lambda}{2n} = \frac{0.003}{3} = 0.001\,\mathrm{m} \tag{3.14}$$

Using the same sizes but dividing the 2π radians around the plate's axis into 16 wedges it is possible to calculate the height of each single step of the 16 in order to obtain the same h_s as the smooth version. A wedge SPPs was designed because, when choosing a large enough number of steps, they have performances very similar to the continuous version but are much easier to manufacture. A 32 wedge $|\Delta l| = 2$ SPP was also produced following the same method. The number of wedges was chosen so that the total phase-shift-to-number of steps ratio is the same as for the mode ± 1 SPP. Finally, a "split" wedge SPP where the ramp is broken into two parts giving 2π phase-shift each. The latter split structure could be useful for keeping the thickness of the plate small even for higher modes.

3.3 Finite Element Analysis with HFSS

Once the design of the q-plate was complete Dr. Pisano simulated it using a Finite Element Analysis software, namely HFSS by Ansys Ansoft. This step is important to check the plate is actually behaving as expected and to have realistic simulation to compare the future data with.

In order to simulate the radiation-matter interaction and determine the field throughout the whole model, HFSS splits the 3D model into tetrahedral cells varying their size and density depending on the complexity and the details they have to fit. The field equations are then numerically and iteratively solved on the discretised tetrahedral mesh.

To generate the simulation the 3D structure of the plate has to be recreated in the HFSS space and then assigned the material that the manufactured plate will use.

The next step is to create a box around the object that can be "filled" with air ($n = 1$) as it will be in the lab and to set the walls of this box as totally radiative in order to simulate free space and avoid any reflection from the boundaries.

Once this is done it is necessary to create a radiation source at a certain distance from the plate that will resemble the real future experimental configuration (see next chapter) and set it to be a Gaussian beam. The wavelength, beam waist and polarisation of the beam are also chosen to match with the real conditions. Irradiating the plate under test with the fundamental Gaussian beam and plotting the amplitude, intensity and phase of the beam in the far field on the other side of the plate allows a check to see if the plate is actually imparting a vortex on the beam and provide an expected outcome for the next experimental test in the lab.

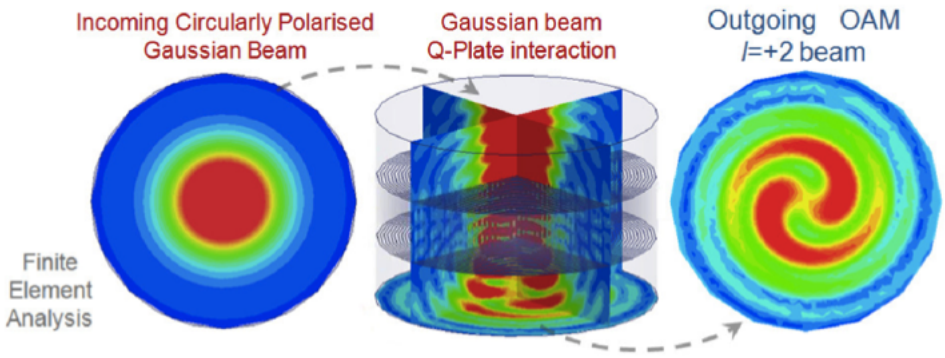

Figure 3.18: Finite Element simulation of the Gaussian incoming transverse field (left) and the out coming field after the interaction with the inner section of the mode |2| q-plate (left).

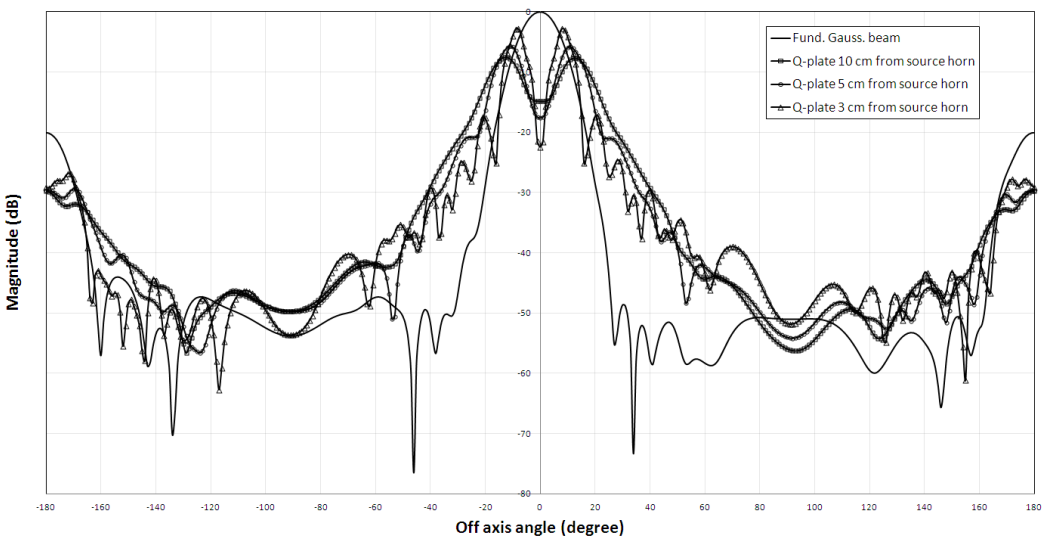

Figure 3.19: Finite Element simulation of the out coming field after the interaction with the inner section of the mode |2| q-plate. Data are plot on a transverse far field beam cut.

Simulations with HFSS are physically accurate but the calculation method implemented requires huge computational power. The resources available in these terms at the moment allow simulations of only a small portion of the q-plate. The portion simulated corresponds to an inner circle of 3 cm of radius. Following this first try we understood that if we wanted a feasible and still accurate enough simulation it was better to change to another software, namely FEKO. At the time of this thesis, simulations using another software for Electromagnetic modelling, FEKO [64] are being made by colleagues in order to compare the results with the actual data collected testing the SPPs. The results will be published in a paper soon.

3.4 Manufacture

The q-plate prototype was manufactured in the School of Physics and Astronomy workshop at the University of Manchester. The grooves were machined using a commercially available milling tool with a 0.5 mm diameter. Such a small milling tool could not reach the required depth of 8.2 mm and so, half-depth grooves were cut on both sides of the disc in order to obtain the same required overall phase shift

effects (Fig. 3.16). This assumption was verified again with the FEA software and it was also checked the absence of standing waves that the central disc, supporting the grooves on both sides, could have created. With this manufacturing technique it is possible to produce q-plates able to generate beams carrying OAM with other states (or for other frequencies) by simply changing the groove geometry (i.e. depth, spacing, thickness).

The SPPs were manufactured using a milling machine. The precision of the steps was limited by the size of the tools.

Tolerance of the machine movement is 0.01 mm but with cutter push off and the nature of the material in reality it probably reached ± 0.05 mm.

The centre of the plates is the most difficult part to manufacture and, at the same time, the most important for the proper functionality of the plate. In the case of the wedge SPPs that implies the sides to be slightly rounded and not sharp. In the case of the smooth SPP a cylindrical volume of polypropylene of 6 mm of diameter had to be left at the centre of the plate as the machine couldn't be set to create the singular central point.

Something to be taken into account when manufacturing plates made from this kind of material, is that it is relatively soft. This means that the friction produced by the contact with the milling tools during manufacturing could affect the good outcome of the process. Due to the flimsy work holding only light cuts could be taken. Unfortunately it was not possible to use air cooling in the making of the plates. The problem was solved at the price of longer production times (of the order of weeks) by making the tool move at a very slow rate. However, a coated carbide cutter was used to reduce friction and only minimal heat was generated.

3.4.1 Plates list

To summarise, all the produced plate type characteristics are reported on the next page together with pictures of the prototypes.

Plates prototypes	
Mode |2| q-plate	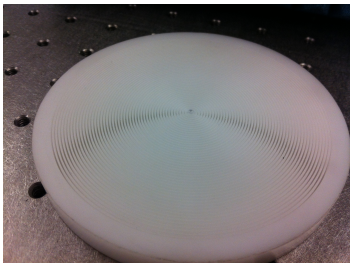
SPP mode |1| smooth	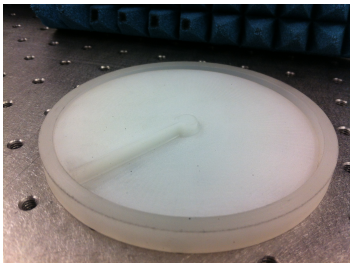
SPP mode |1| wedges	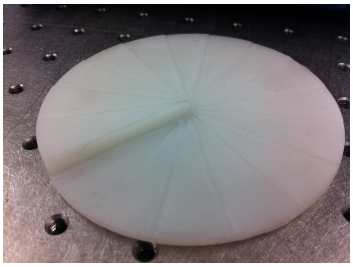
SPP mode |2| wedges	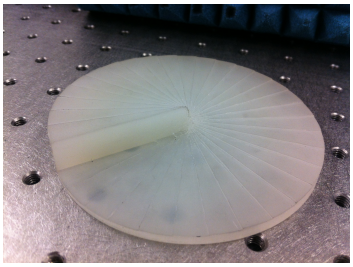
SPP mode |2| double ramp	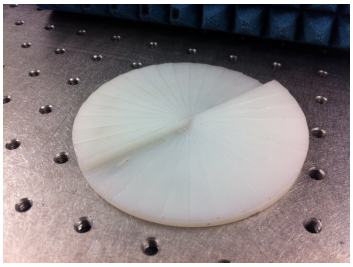

Chapter 4

Experimental testing and results

"A theory is something nobody believes, except the person who made it. An experiment is something everybody believes, except the person who made it."
Albert Einstein

Chapter outline

In this chapter I report the various measurements that were performed on the prototype PMDs described in the previous chapter. Considering that the q-plates and the SPPs have different working principles, different set of measurements and optical elements were needed. For instance the q-plate working with circular polarisation implies the need of optical elements like quarter wave retarders (QWRs). These are not needed for the SPP tests because these devices can also work with linear polarisation. Having designed and manufactured q-plates and SPPs for the first time during this project meant that all the lab equipment had to be reconfigured for OAM measurements and that a standard procedure for the testing of these plates needed to be put in place.

The first thing to be demonstrated is that the manufactured q-plate and SPPs are in fact producing optical vortices. That means checking that the main characteristics of an OAM beam are present. The two main features that identify it are the phase change around the propagation axis and the annular intensity pattern in the far field

zone (Table 2.1). To confirm the presence of these characteristics measurements were performed using different experimental setups that are described in detail in the following sections. The measurements are reported in the same order as they were performed in the lab following the evolution of our equipment.

The chapter is structured as follows:

1. The description of the main piece of equipment in the RF lab, the Vector Network Analyzer (Section 4.1)
2. A section with the four types of measurements and relative experimental setup that were performed with the q-plates (Section 4.2)
3. A section where a set of measurements performed specifically only on the mode |2| wedge SPP is reported (Section 4.3)
4. A section that reportes all the intensity and phase data of the SPP generated beams (Section 4.3.6) collected with the new near-field scanner setup.

4.1 The Vector Network Analyzer (VNA)

The main piece of equipment in the RF laboratory is a Rohde&Schwartz Vector Network Analyzer. The VNA has input-output ports both able to transmit and receive microwave signals. The VNA is consequently able to measure the S-parameters of a system that can be just a waveguide or a free space setup. In the case of a waveguide system, in order to measure the S-parameters of a device it is required to calibrate the system including everything that is not under test and then connect the device directly to the two ports. In the case of a free space system the alignment between the source and the receiver antennas becomes a matter of extreme importance and the most time consuming.

The S-parameters of a microwave system are defined as the elements of the so-called Scattering Matrix that links the incident (a_1, a_2) and reflected (b_1, b_2) wave amplitudes as follows (see Figure 4.1).

$$\begin{bmatrix} b_1 \\ b_2 \end{bmatrix} = \begin{bmatrix} S_{11} & S_{12} \\ S_{21} & S_{22} \end{bmatrix} \cdot \begin{bmatrix} a_1 \\ a_2 \end{bmatrix} . \tag{4.1}$$

This in equation form is

$$b_1 = S_{11}a_1 + S_{12}a_2\,, \tag{4.2}$$

$$b_2 = S_{21}a_1 + S_{22}a_2\,. \tag{4.3}$$

That means that S_{11} is the input port voltage reflection coefficient, S_{12} is the reverse voltage gain, S_{21} is the forward voltage gain and S_{22} is the output port voltage reflection coefficient. From the measured S-parameters it is possible to retrieve the intensity and the phase of the field. Specifically, for the transmitted wave, the field's intensity and phase are

$$I = |S_{21}|^2\,, \tag{4.4}$$

$$\phi = \arctan\left(\frac{ReS_{21}}{ImS_{21}}\right)\,. \tag{4.5}$$

In these experiments the outgoing waves were mainly looked at. As such, interest was mainly focussed on the S_{21} parameter (considering port 1 the emitting port and port 2 the receiving port).

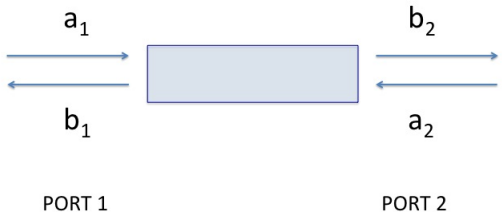

Figure 4.1: Scheme of the S-parameters and their meaning.

The RF laboratory VNA together with specific W-band heads generate radiation

with frequencies ranging from 75 GHz up to 110 GHz. This work is mainly focussed on radiation at 100 GHz as the plates are inherently narrowband and have been designed specifically for that frequency.

4.2 q-plate testing

The purpose of the tests was to demonstrate that the manufactured Nylon mode |2| q-plate is actually generating a vortex beam by comparing its performance with the previously simulated results. A set of experimental measurements were carried out using the VNA equipped with W-band heads ($75 - 110$ GHz). Pyramidal Eccosorb [1] was used in the experimental setup to cover any metallic surfaces surrounding the optical path to minimise reflections and diffracted radiation. Two identical corrugated horn antennas were used to generate and receive an almost pure fundamental Gaussian mode (98% of the total power). The W-band Winston-like corrugated horns that were used by the author in this and in all of the following setups as emitting and receiving antennas are correctly performing elements whose behaviour is fully described in [38]. The feed horn generates a beam with a beam waist $w_0 = 5$ mm at 100 GHz. It satisfies the Gaussian beam model condition which states that the waist has to be larger than about $2\lambda/\pi$. In this case $2\lambda/\pi < 5$ mm.

Four different measurements were performed on the q-plate designed for operations at 100GHz as listed below:

1. Beam cut measurements to demonstrate that the q-plate locally acts as a HWP (converting the polarisation state from LHCP to RHCP)

2. Azimuthal beam cut measurements to check the ring-shaped intensity pattern and its symmetry

3. 2D planar transverse scan for the reconstruction of the beam phase structure

4. Telescope setup measurements of collected power under the action of one or two identical q-plates

4.2.1 Measurement of the LHCP to RHCP (and vice versa) conversion through the q-plate

In the first set of measurements, the goal was to show that the q-plate locally acts as an HWP, as theoretically expected. If so, the q-plate would convert LHCP to RHCP and vice versa (Fig. 4.3). This can be deduced from the signal intensity using the right configuration of quarter-wave retarders (QWRs). The test consisted of a far-field beam pattern measurement, on a cut parallel to the optical table, as shown in figure 4.2. In order to perform such a measurement, a rotary stage was used to rotate the transmitter and q-plate around the transmitting horns phase centre. The rotating system covered an off-axis angle of $\pm 35°$. The VNA measures the S-parameters of the system allowing the beam intensity profile to be reconstructed as a function of the off-axis angle. Although the VNA emits and detects radiation at all the frequencies within the W-band, the data analysis was only carried out at 100 GHz, frequency for which the q-plate was designed. The VNA produces and detects linearly polarised radiation propagating in rectangular waveguides. Therefore, in order to generate the circular polarised Gaussian beam required by the q-plate, a rectangular-to-circular waveguide transition, a waveguide circular polariser (or QWR), and a corrugated horn were added to the VNA transmitter as well as on the receiver. The distance between the q-plate and the receivers is such that the far-field condition, $d = 2D^2/\lambda$, where D is the maximum dimension of the antenna, is assured. Lets consider the beam-scan setup (Fig. 4.2) but without the q-plate. It consists of two sliding platforms where it is possible to mount the VNA heads and align them at any distance within about 80 cm. One of the two platform sits on a rotary stage that rotates parallel to the optical table and on top of it is another rotary stage, albeit perpendicularly mounted, that can perform rotations of the VNA head on the transverse plane. With this experimental configuration we are able to measure one dimensional far-field beam pattern angular cuts of the kind shown in Fig. 4.4. Specifically, the two horns are aligned by positioning them at a distance according to the requirements, then, the alignment is refined by levelling the stages and maximizing the received signal. After that step the plate under examination was placed on a support fixed to the horizontal rotary stage and aligned by minimising the received signal. The signal needed to be

minimised because the horns are supposed to be centred with the singularity of the generated vortex where the field is expected to be zero (i.e. not defined, singularity). Rotating the whole horn-plate system around a centre corresponding to the beam waist of the emitted beam allowed the intensity and phase profile of the beam to be measured.

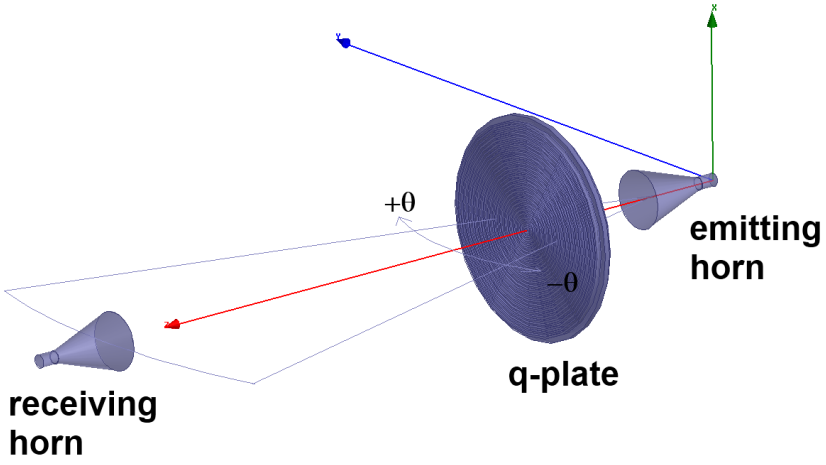

Figure 4.2: Experimental set-up for far field beam pattern measurements. The source horn and the q-plate rotate together around a centre located on the beam waist of the beam at the horn aperture making it possible to scan the wavefront at a certain distance with the receiver horn.

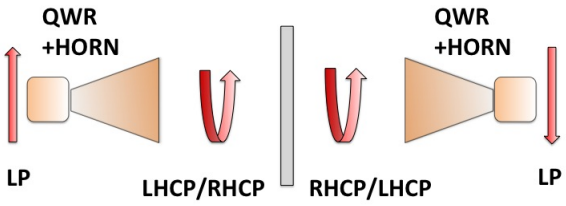

Figure 4.3: Polarisation of the radiation at the different stages of the experimental setup. The q-plate acts as an HWP thus rotating the circular polarisation obtained with the QWR from right handed to left handed or vice versa.

When the two QWR on the VNA heads are placed at 90 degrees with respect to each other, the collected signal is maximum as the receiver is sensitive to the same polarisation as the emitted radiation, i.e., RHCP (solid curve in figure 4.4 a)). As the q-plate is introduced in between the two horns the signal is expected to be minimised as the plate acts as a HWP because of its birefringence (dotted curve in Fig. 4.4 a)). The QWR on the receiver was then rotated by 90 degrees and the same measurements were performed to further corroborate the result (see Fig. 4.4 b)). It was therefore confirmed the q-plate was acting as a HWP converting RHCP to LHCP (and vice versa).

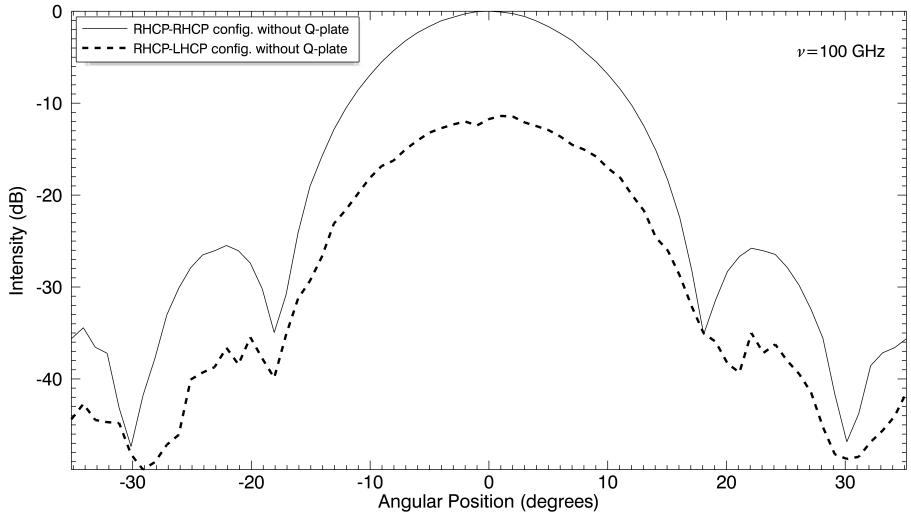

(a)

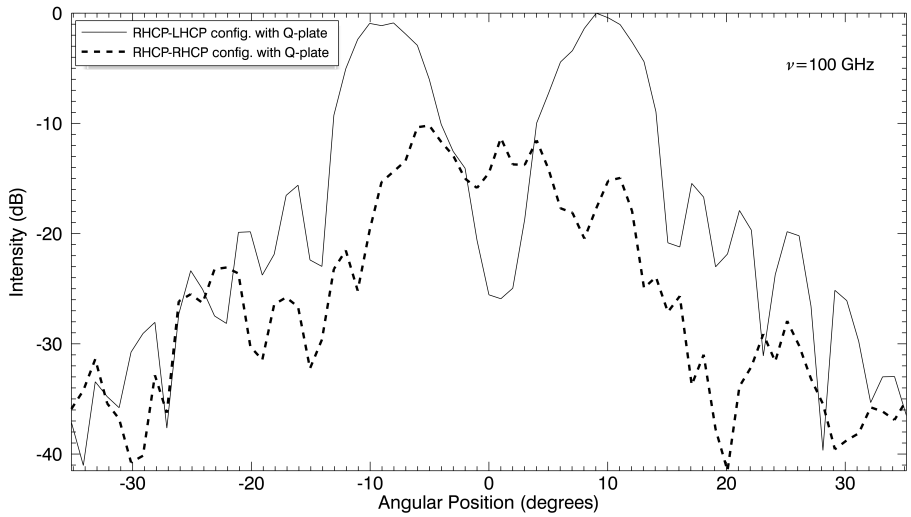

(b)

Figure 4.4: Beam intensity profile of both the Fundamental Gaussian beam produced by the source horn and the OAM beam generated by inserting the q-plate a few centimetres after the source horn are reported. Both beam patterns were measured having the two horns emitting and receiving radiation with the same circular polarisation (a) or opposite circular polarisation (b) in order to confirm the q-plate is acting as an HWP.

It should be noted that the waveguides only let vertical linear polarisation go through and therefore act as linear polarisers.

Expressing the process using Jones' formalism helps understand what happens. What has been described can be expressed as follows.

The generic matrix for a wave retarder is

$$J_{wp}(\phi,\theta) = \begin{bmatrix} \cos\frac{\phi}{2} + i\sin\frac{\phi}{2}\cos 2\theta & i\sin\frac{\phi}{2}\sin 2\theta \\ i\sin\frac{\phi}{2}\sin 2\theta & \cos\frac{\phi}{2} - i\sin\frac{\phi}{2}\cos 2\theta \end{bmatrix}, \tag{4.6}$$

where ϕ is the induced phase shift between two orthogonal field components and θ is the wave retarder's optical axis orientation.

A QWR induces a $\pi/2$ phase shift between two perpendicular components of the incoming radiation parallel to its axis. This phenomenon produces circular polarised light. Since the input radiation is linearly polarised the QWR's axis should be oriented at 45 degrees to the polarisation direction. It follows that the previous matrix becomes

$$J_{wp}\left(\frac{\pi}{2},\frac{\pi}{4}\right) = \frac{1}{\sqrt{2}}\begin{bmatrix} 1 & i \\ i & 1 \end{bmatrix}, \tag{4.7}$$

and

$$J_{wp}\left(\frac{\pi}{2},\frac{3\pi}{4}\right) = \frac{1}{\sqrt{2}}\begin{bmatrix} 1 & -i \\ -i & 1 \end{bmatrix}, \tag{4.8}$$

in the case of a QWR at 90 degrees to the previous one.

The matrix of a HWP, which induces a π phase shift between two perpendicular components is

$$J_{wp}(\pi,0) = \begin{bmatrix} i & 0 \\ 0 & -i \end{bmatrix}, \tag{4.9}$$

What happens can be represented in terms of polarisation along a straight line passing through a single position on the q-plate surface as follows

$$J_{wp}\left(\frac{\pi}{2},\frac{3\pi}{4}\right)\cdot J_{wp}(\pi,0)\cdot J_{wp}\left(\frac{\pi}{2},\frac{\pi}{4}\right)\cdot\begin{bmatrix}0\\1\end{bmatrix}= \\ =\frac{1}{\sqrt{2}}\begin{bmatrix}1&-i\\-i&1\end{bmatrix}\begin{bmatrix}i&0\\0&-i\end{bmatrix}\frac{1}{\sqrt{2}}\begin{bmatrix}1&i\\i&1\end{bmatrix}\begin{bmatrix}0\\1\end{bmatrix}=-\begin{bmatrix}1\\0\end{bmatrix} \quad , \tag{4.10}$$

If the same calculation is done neglecting the HWP which corresponds to taking the q-plate out from the optical path, we have, instead

$$J_{wp}\left(\frac{\pi}{2},\frac{3\pi}{4}\right)\cdot J_{wp}(\frac{\pi}{2},\frac{\pi}{4})\cdot\begin{bmatrix}0\\1\end{bmatrix}= \\ =\frac{1}{\sqrt{2}}\begin{bmatrix}1&-i\\-i&1\end{bmatrix}\frac{1}{\sqrt{2}}\begin{bmatrix}1&i\\i&1\end{bmatrix}\begin{bmatrix}0\\1\end{bmatrix}=\begin{bmatrix}0\\1\end{bmatrix} \quad , \tag{4.11}$$

As can be seen in (4.10), with the previously explained configuration of QWRs, if the q-plate is inserted the output wave at the receiving horn is linearly polarised perpendicularly to the input wave. This implies that the receiving horn is not able to detect the signal as it is acting as a vertical linear polariser.

In the second case (4.11) the q-plate is not inserted so the output polarisation is the same as the input. Note that we did not introduce the q-plate matrix here but only the HWP matrix oriented at a certain angle representing the local behaviour of the plate.

4.2.2 Beam cut measurements

A second set of measurements was taken with the same technique above, but this time performing the cut at different angles with respect to the transverse plane. These multiple cuts allow us to see if the vortex beams typical ring-shaped intensity pattern is present and if it is symmetric, as expected for a pure OAM state. It can be seen in Fig. 4.7 that the magnitude of the field on all the cuts is similar as expected. These

data were also compared with the FEA simulations previously performed by Dr. Pisano, taking into account the distance between source and the q-plate ($d = 10\,\mathrm{cm}$). Figure 4.6 shows that the simulation and experimental profiles are in very good agreement. The comparison between the experimental and the modelled results is made for both the reference fundamental Gaussian beam produced by the horn and for the beam transformed by the q-plate. The transmission magnitude, calculated from the S_{12} parameter, is reported as a function of the off-axis angle at the fixed frequency of 100 GHz.

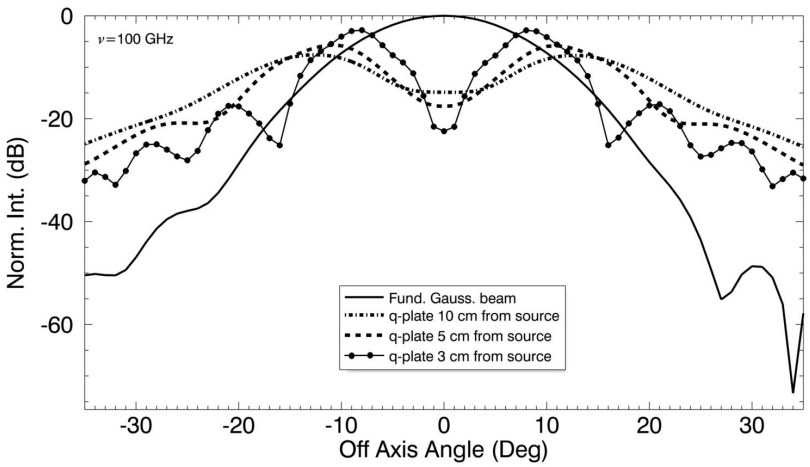

Figure 4.5: Beam profile, Finite Element simulations: the fundamental Gaussian beam taken as a reference is compared with the same beam going through the q-plate positioned at 3, 5, and 10 cm from the horn antenna aperture.

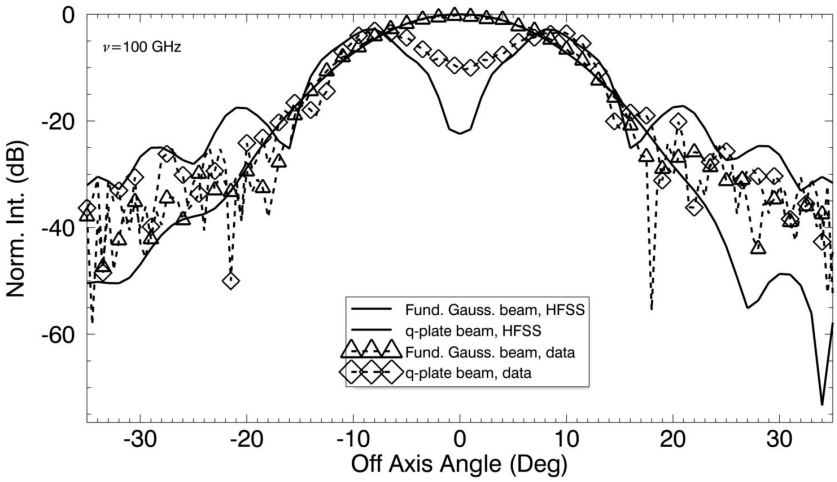

Figure 4.6: Model (dashed curves) and experimental data (solid curves) of the original Gaussian beam and the beam after passing through the q-plate placed at 10 cm from the source.

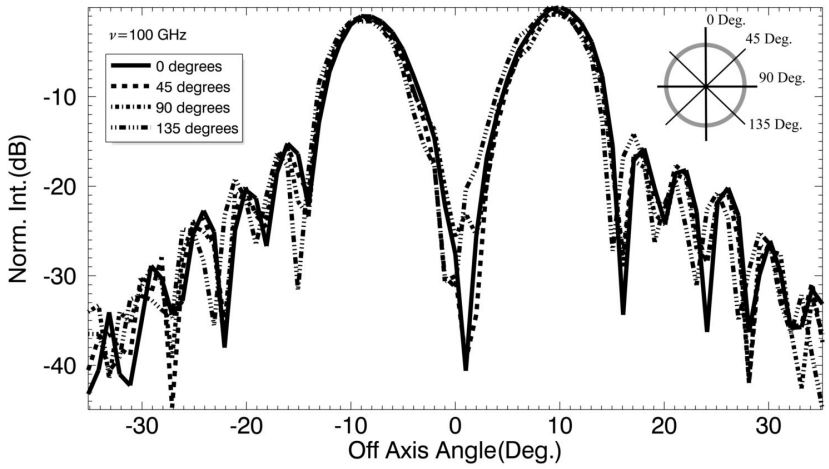

Figure 4.7: Far-field intensity pattern of the q-plate output beam at different angles on the transverse plane obtained with the rotary beam scan setup. For simplicity only the cuts at 0, 45, 90, and 135 deg are reported but data were taken every 5 deg and all the cuts are consistent.

4.2.3 2D planar transverse scan for the reconstruction of the beam phase structure

To fully characterise the q-plate behaviour a third set of measurements was performed. After aligning the source and receiver horns to the central point of the q-plate, the plate itself was transversally moved along an imaginary grid in order to collect data at different points of the plate surface. Data was collected at 5 mm intervals covering an area of about 25 cm^2 on the q-plate surface. Using this technique, the real part of the E field was recorded. The phase value at each point is compared to a chosen phase which is taken as zero reference. This way it is possible to plot the phase shift induced in each point of the surface and map the global behaviour of the plate. The local birefringence effects are then visible. Using this scanning system was the best way possible at the time to simulate a plane wave illuminating the plate point by point as if using a pencil beam. A scheme of the setup can be seen in Figure 4.8. The experimental data, reported in Fig. 4.9, shows the total phase change, around the central axis of the plate, to be 4π. Both the measured real part of the field and the relative phase-shift (Figs. 4.8 c) and 4.8 d)) match with the ones expected from the theory calculated with the IDL code explained in the previous chapter (Figs. 4.8 a) and 4.8 b)). These data agree extremely well with expectations, since the q-plate was designed to produce $l = \pm 2$ modes. The 4π change in the phase is clearly visible and represented the best experimental data available of the phase of a millimetre vortex to our knowledge at the time of this experiment [37].

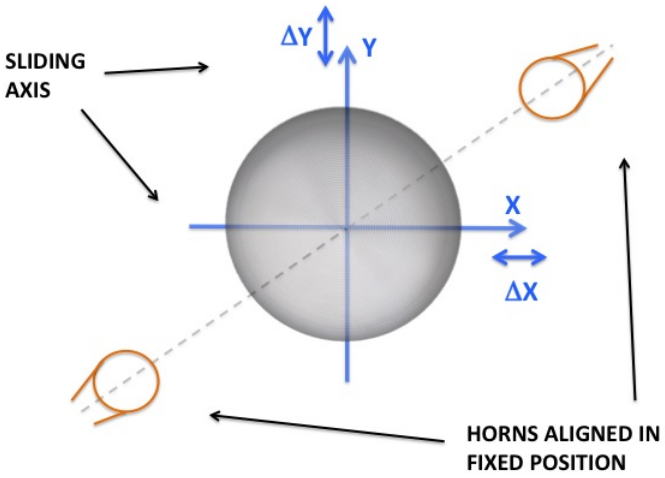

Figure 4.8: Simplified scheme of the 2D scanning setup used to reconstruct the q-plate generated beam's phase structure.

Asymmetries in the data are caused by misalignments between the source horn, the receiving horn and the centre of the plate. Due to the scanning stage being at a very early stage of the process of being developed. The 3D scanning system used later on for the measurements involving the SPPs implemented by colleague Peter Schemmel greatly improved greatly the sensitivity and precision achievable in this kind of measurement.

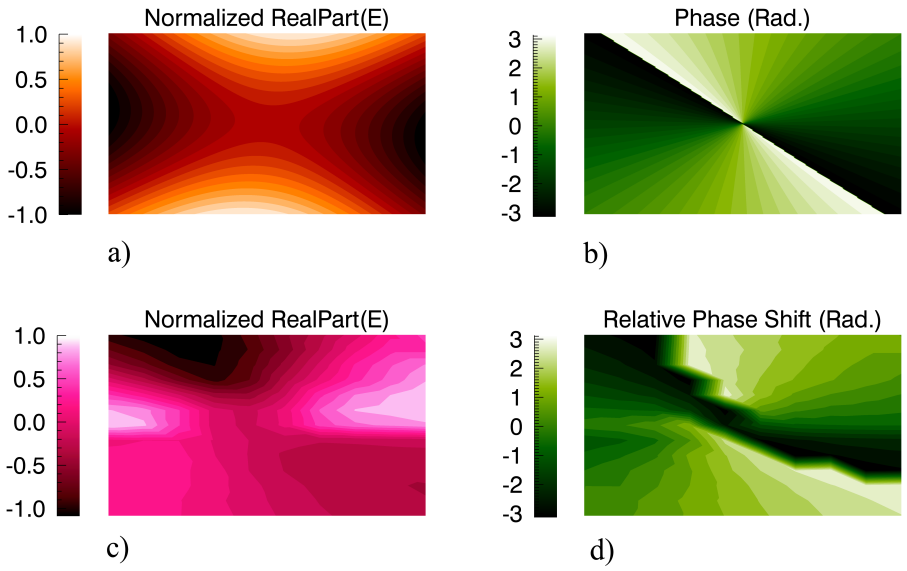

Figure 4.9: Measured E field real part (c) and relative phase-shift (d) induced by the q-plate at different points on the central part of its surface. In (a) and (b) the theoretical expected ones are reported. Asymmetries in the data are possibly due to misalignments between the horns and the limited precision of the xy moving system.

4.2.4 Telescope setup measurements of collected power

A telescope setup was arranged to collect data showing a decrease in power collected by the horn, in which a Gaussian beam was focussed, when a q-plate was interposed. The decrease is expected as the horn is specifically designed to generate, and consequently collect, radiation with Gaussian amplitude and phase distribution profile. If there was perfect alignment and matching between all the parts in the optical system and a 100% efficient q-plate the power should go down to zero. In reality the alignment achievable with this system was not optimal at the time of this measurement.

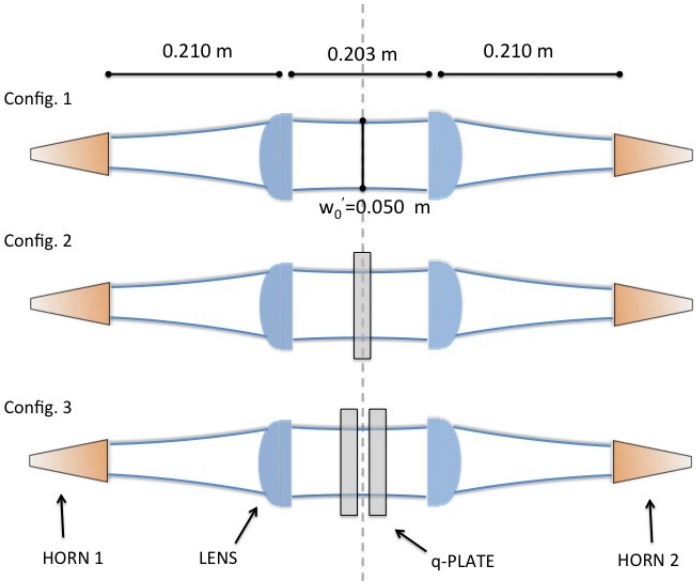

Figure 4.10: The 3 configurations for which data were collected. In configuration 1 (top) a collimated beam is created in between two lenses and then the beam is focused back into the second horn. In configuration 2 (middle) the setup is kept as in configuration 1 but now a mode |2| q-plate is inserted in between the lenses where the new larger beam waist is. In the third configuration (bottom) another identical q-plate is inserted in order to cancel out the effect of the previous one.

These measurements will be retaken in the future with a new setup. As for the previous measurements involving the q-plate, QWRs were mounted on both the VNA heads and specifically positioned after the rectangular-to-circular transitions in order to generate and detect the circular polarisation. Moreover, a second identical q-plate was inserted in the setup to show that it would convert the OAM back to zero (ideally). This means the refocused beam is converted back to the fundamental Gaussian and so the horn would again collect signal. The relative distances at which for the horns, the lenses and consequently the plates were calculated using Ray transfer matrix analysis. According to this formalism a 2 x 2 ABCD matrix that represents the action of each of the two thick lenses involved in this setup is considered. It was used to calculate where the new beam waist is created (i.e. at which distance from the lens) and to deduce its width. If we consider the initial beam waist to be $w_0 = 5\,\text{mm}$ and a thick lens with the specifications reported in table 4.1 that the matrix for the lens is

$$\begin{bmatrix} A & B \\ C & D \end{bmatrix} = \begin{bmatrix} 1 + \frac{(n_2 - n_1)d}{n_2 R_1} & \frac{n_1 d}{n_2} \\ -\frac{1}{f} - \frac{(n_2 - n_1)^2 d}{n_1 n_2 R_1 R_2} & 1 + \frac{(n_1 - n_2)d}{n_2 R_2} \end{bmatrix}, \tag{4.12}$$

where f is the lens focal distance and n_1 and n_2 are the refractive indices of the lens surrounding and of the lens material respectively.

The new beam waist and its location are

$$w_{0\,out} = \frac{w_{0\,in}}{[(Cd_{in} + D)^2 + C^2 z_c^2]^{0.5}}, \tag{4.13}$$

$$d_{out} = -\frac{(Ad_{in} + B)(Cd_{in} + D) + ACz_c^2}{(Cd_{in} + D)^2 + C^2 z_c^2}, \tag{4.14}$$

where A, B, C and D are the lens matrix elements, $w_{0\,in}$ and d_{in} are the initial beam waist and its distance from the lens and z_c is the one defined in (2.14).

Thick lenses specifications	
Radius of curvature, R_1,	$-112\,\text{mm}$
Radius of curvature, R_2,	∞
Material,	UHMWPE
Refractive index lens, n_2,	$n_2 = 1.53$
Refractive index air, n_1,	$n_1 = 1$
d	$11.94\,\text{mm}$
Focal length, $f(d_{in})$,	$211.32\,\text{mm}$

Table 4.1: Thick lenses specifications for the lenses used in the telescope setup shown in 4.10

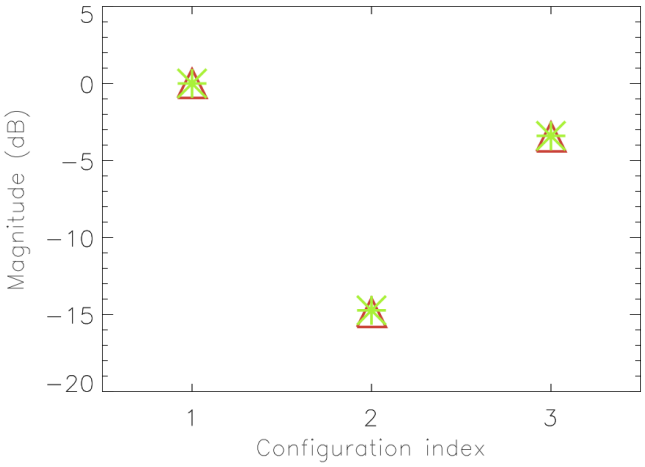

Figure 4.11: Measured S21 (red) and S12 (green) for the 3 experimental configurations in Figure 4.10. Data is normalised to the maximum power collected when no q-plate is inserted in the optical path.

This setup was not optimal and so the alignment between the horns and between the beam and the centre of the q-plates was causing a huge power loss. Alignments between the horns is important to maximase the collected power, while the alignment of the horns with the q-plates is vital for the mode conversion efficiency. Moreover, placing the two q-plates close to each other caused standing waves due to the devices reflections. Although these problems largely influenced the outcome of this measurement, it is still possible to see that the collected powers follow the expected trend. The plot shows a big decrease in collected power when we insert the q-plate (configuration 2) compared to the telescope system without plate (configuration 1). Inserting a second identical q-plate induces a regain in power, even if it is losing about half the signal for the aforementioned reasons.

4.3 SPPs testing

Several measurements were performed on the wedge SPP designed for generating a mode |2| vortex at 100 GHz as a general test while a high resolution 3D set of measurements was taken for all the SPPs. This section is structured as follows:

1. A section with the beam cut measurements performed on the mode |2| wedge SPP

   (a) Intensity and phase of the beam generated by the corrugated circular horn only

   (b) Intensity and phase of the beam generated by the corrugated circular horn with the empty plate holder in place (to check it doesn't affect the main beam)

   (c) Beam cuts of the mode |2| OAM beam (SPP in place) at different angles showing the intensity structure and symmetry of the beam

   (d) Beam cuts of the mode |2| OAM beam (SPP in place) at different distances from the plate

2. Intensity and phase data taken with the 3D near-field scanner on the xz, yz and xy planes for all the designed SPPs

4.3.1 Azimuthal beam cuts

The first set of measurements were performed on the wedge mode |2| SPP only. For this purpose the rotary stage setup shown in the previous section was used to take beam cuts. All the cuts are taken after careful alignment of the source and the receiver and then of the plate. The aligning procedure consists of a first order alignment between the horns on the two ports with levels and rulers and then a more fine alignment by maximising the power signal read by the VNA. When the SPP is introduced it was aligned so the received signal is minimised due to the minimum at the vortex's centre. To do this the SPP's holder was placed on a $x - y$ positioning stage that allowed very small movements to optimise the alignment.

Four different measurements were performed. For each set of measurements both the intensity and phase profile were recorded.

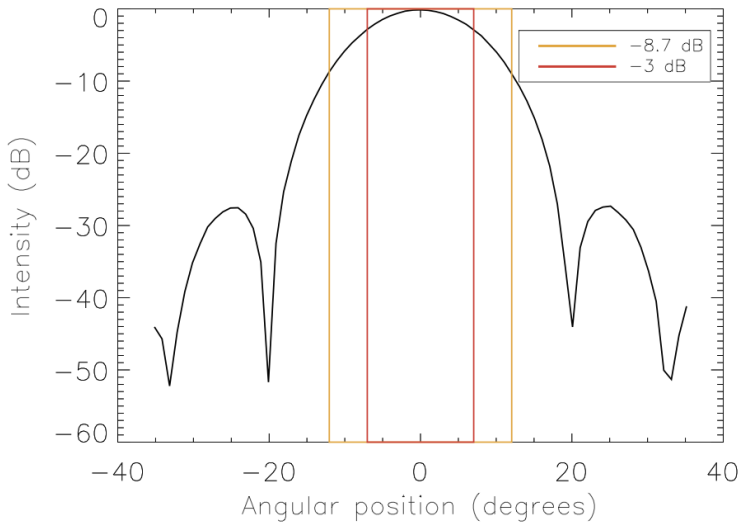

(a)

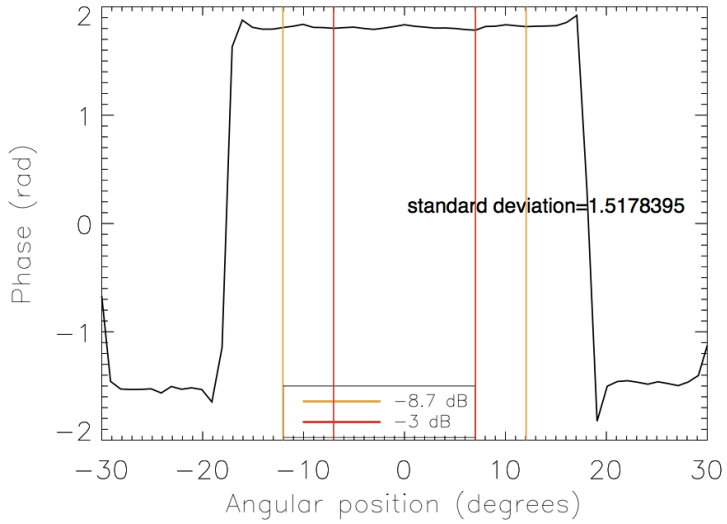

(b)

Figure 4.12: Intensity (a) and phase (b) profile of the Gaussian beam at 100 GHz generated by the corrugated horn. The highlighted areas correspond to the beam within the beam radius.

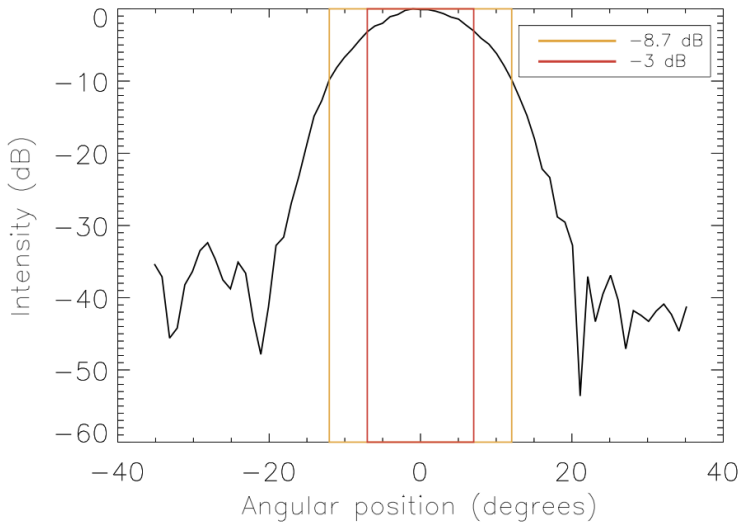

(a)

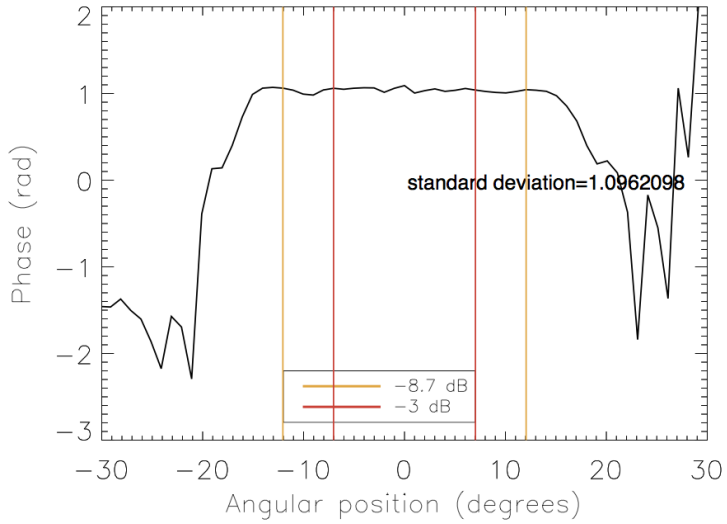

(b)

Figure 4.13: Intensity (a) and phase (b) profile of the Gaussian beam at 100 GHz generated by the corrugated horn when the plate holder is put in place. The highlighted areas correspond to the beam within the beam radius.

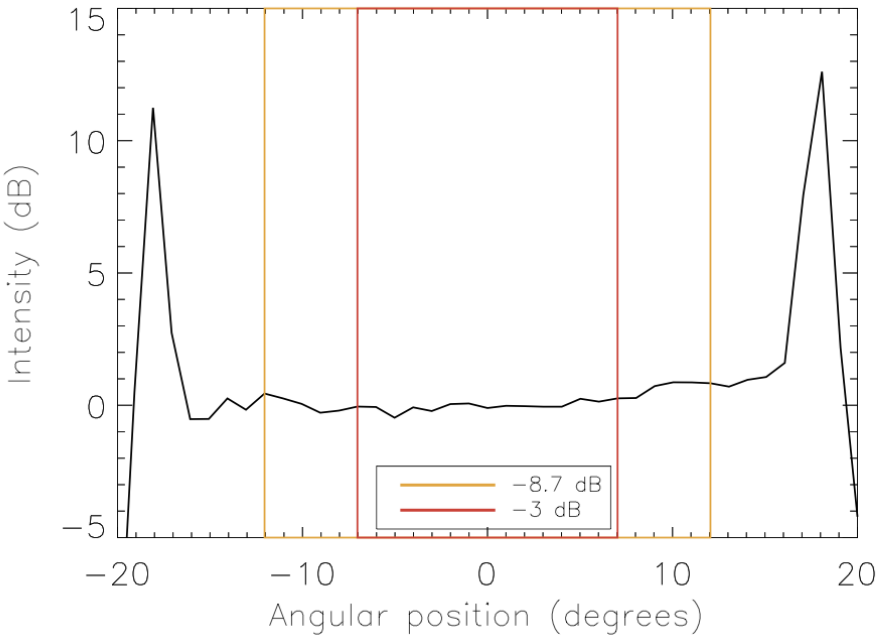

Figure 4.14: Difference in the intensity pattern between the horn beam without an element interposed and with the same beam passing through the empty plate holder used for the following measurements.

In figures 4.12 a), 4.12 b), 4.13 a) and 4.13 b) the area delimited by the red line corresponds to what the author considers to be the main beam. This is the section of the beam that needed to be checked to ensure it was not negatively affected by the presence of the plate holder. As it can be seen in figure 4.14 the beam before and after placing the holder stays reasonably constant across the main beam. Most importantly the phase remains flat (figure 4.12 b), 4.13 b)). The phase being flat in the central part of the beam is the most important feature as it gives the best possible condition (considering we have a Gaussian beam and not plane waves as input) for the proper functioning of the plate. The more constant the input phase is the more the output phase will represent the vorticity due to the plate.

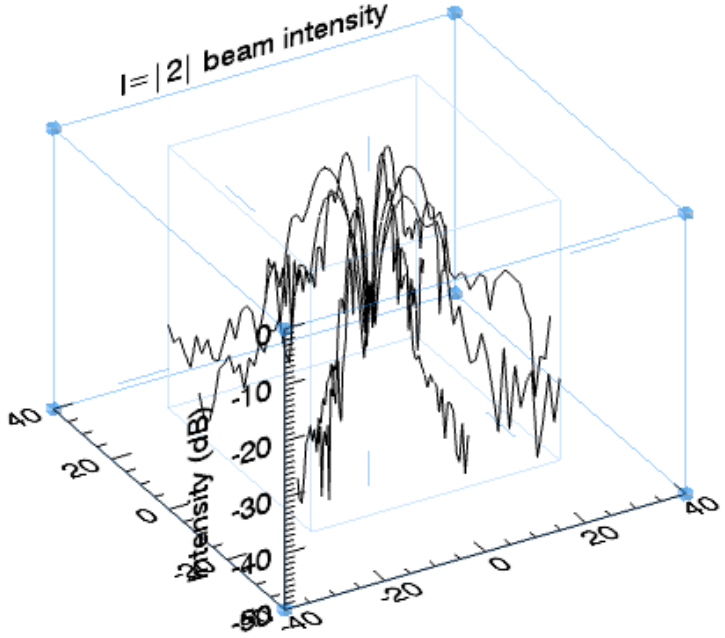

Figure 4.15: Intensity profile in dBs of the beam generated by the mode |2| SPP at different azimuthal angles. The ring shaped transverse profile and the overall symmetry can be seen, together with the central minimum.

The first measurement performed on the mode |2| SPP (Fig. 4.15) was a series of beam cuts on the transverse plane at different azimuthal angles. Data was collected in the same way as the q-plate and for the same purpose. The aim is to check the intensity pattern is ring shaped as expected. A singular beam cut is not enough because other higher modes could generate a similar pattern. The symmetry of the intensity ring also indicates that the plate is generating a pure enough mode as a superposition of modes with similar weights would create asymmetries.

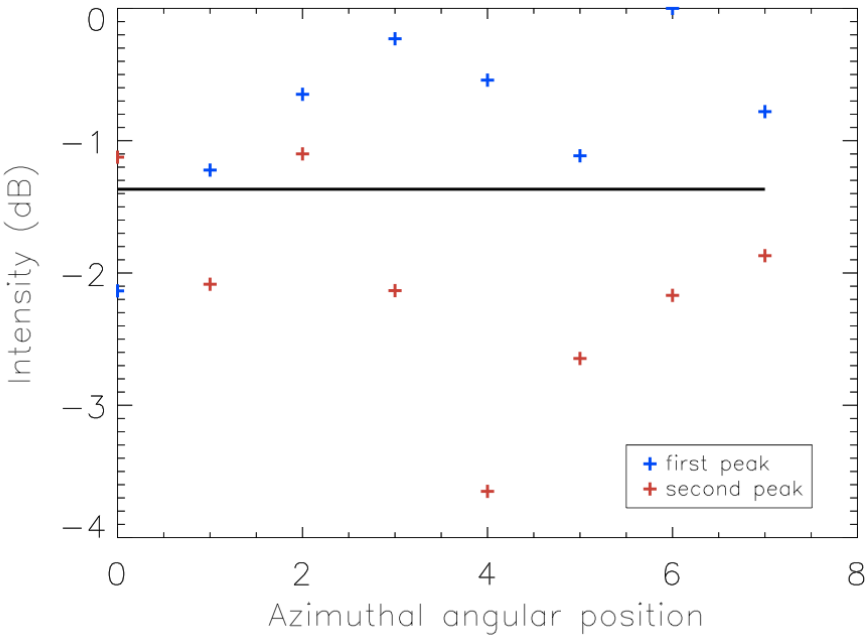

Figure 4.16: Intensity profile in dBs of the beam generated by the mode |2| SPP at different azimuthal angles. A beam cut was performed every 22.5 degrees.

In figure 4.16 the values of the intensity maxima for the first and the second peak along each beam cut and the average of those are reported. It can be seen there is a big excursion between some of them up to the order of $3dBs$ but was not thought to be able to affect the aim of the measurements. The cause is probably mostly due to the very delicate alignment between the elements. In order to take the beam cuts at various azimuthal angles the plate has to be rotated and this causes the central point of the plate to move around the centre of the beam cut in case of a small misalignment. As for all the previous measurements the need for a better alignment system is evident.

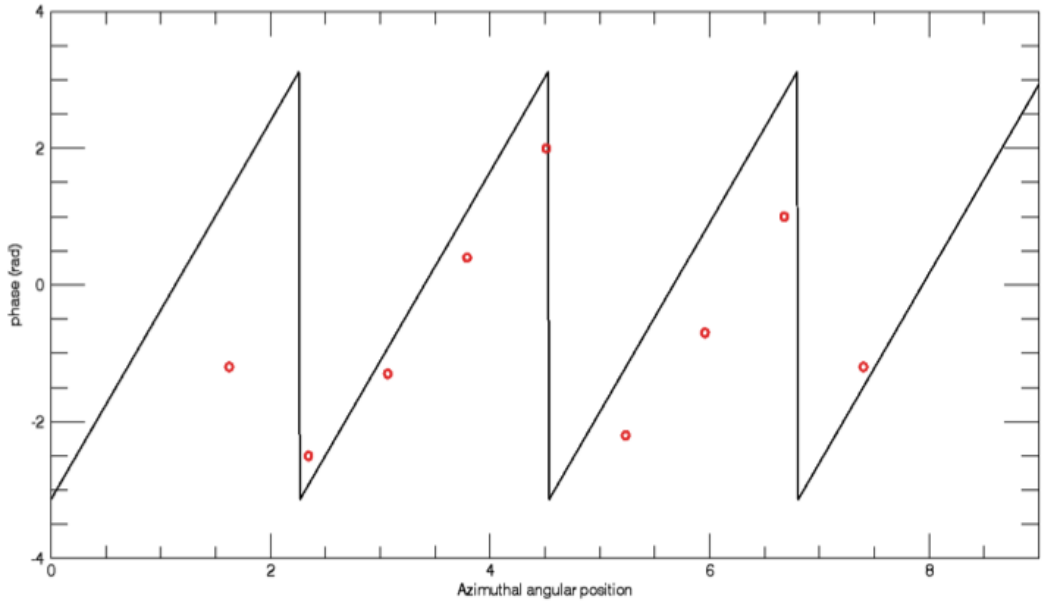

Figure 4.17: Phase value in correspondence to the intensity peaks for each azimuthal cut around the beams axis.

In figure 4.17 the phase data corresponding to the peaks around the beam axis are plotted. Even if the phase change is not the full one expected from theory, as it is probably not exactly centred around the axis, the double cycle expected for a mode |2| vortex is visible.

4.3.2 Beam cuts at different distances from the SPP

Another series of transverse beam cuts was taken, this time changing the distance between the plate and the receiving horn. The emitting horn and the plate are kept at a fixed position and rotated together by the same off-axis angle. Changing the position of the receiver then means taking the beam cut at different stages of the propagation of the same beam. The distance values are not equally spaced due to some experimental limitations of the setup. However these measurements were meant

to check that the phase and intensity profile are consistent through propagation. In figure 4.18 the phase profiles are shown. It is possible to see the phase is symmetric about the centre as expected for a mode |2| as there is a full 2π change between the two arms of the beam cut. In the case of a mode |1| plate we would expect to see an opposite value of the phase at diagonally opposite positions to the beam centre as there would be a π change between the two points. Corresponding to the centre it can be seen the phase "jump" where the phase is not defined due to the singularity.

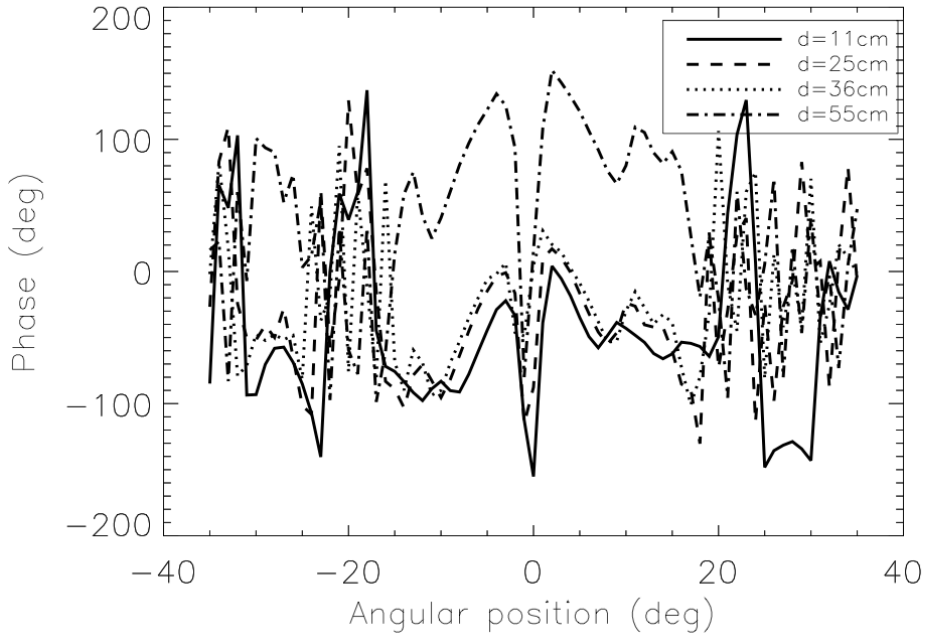

Figure 4.18: Phase profile (deg) of the beam generated by the mode |2| SPP collected moving the receiver horn at different distances from the source horn+plate system.

From the intensity pattern (figure 4.19) it can be seen that the beam profile is maintained through propagation and it spreads as expected. The peaks become smaller but the beam covers the same off-axis angle as the measurements were taken at a distance at which the far field condition is satisfied. The central minimum, while changing slightly in value is always well defined.

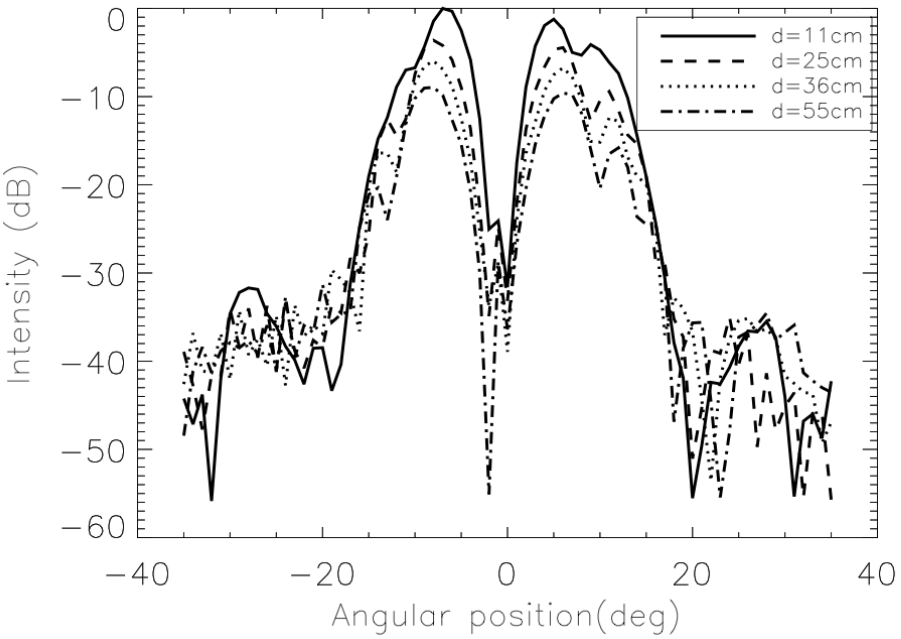

Figure 4.19: Intensity (dB) profile of the beam generated by the mode |2| SPP collected moving the receiver horn at different distances from the source horn+plate system.

4.3.3 Beam cuts for different displacements of the plate from the centred position

In this section I report the data collected for a number of horizontally displaced position of the plate with respect to the central aligned position as represented in figure 4.20. The data was collected on the same beam generated by the mode |2| wedge SPP with emitting horn, receiving horn and the SPP aligned as before. Beam cuts were taken for each shifted position of the plate and at intervals of half a millimetre. The plate was moved by 3mm on both sides. From the beam cut the central intensity value (figure 4.21), the peak intensity (figure 4.22), the peak to central minimum difference (figure 4.23) and the difference between the two peaks (figure 4.24) were extracted. All the data was collected at 100 GHz which is the operating frequency

of the plate. To be noticed that differences in dBs are not meaningful in absolute value but if two signals differ by one decibel they have a power ratio of $10^{\frac{1}{10}}$ which is approximately 1.25892. Therefore the difference value may or may not be significant depending on what is the intensity of the dB scale.

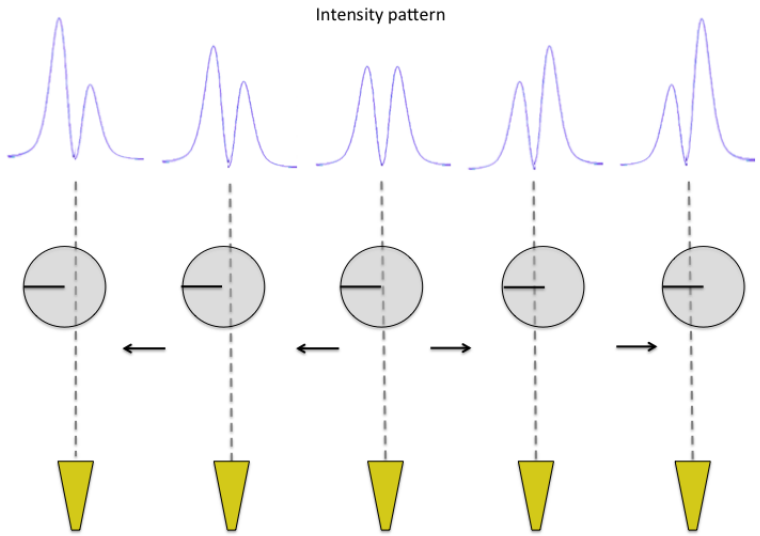

Figure 4.20: A transverse horizontal beam cut is taken for different displaced positions of the plate with respect to the central aligned position. The more the plate is misaligned with respect to the beam axis the more the intensity pattern becomes asymmetric. If the alignment in the central position is accurate, an evaluation of the peaks asymmetry can provide information about the size of the plate displacement.

In figure 4.21 the central intensity value of the transverse beam cut is plotted for each position of the plate. The zero position corresponds to the plate centred with the beam on axis. This position should in principle correspond to the minimum value for the intensity. This is because the plate performs at the best when aligned with the beam. As it can be seen in figure 4.21 the minimum value of the central intensity is not found on the zero position. This could be due to the plate not being 100% efficient thus letting a small percentage of the fundamental Gaussian beam pass through the plate unchanged. Another possibility is that the plate centre is not perfectly aligned with the centre of the beam. Anyway, the difference between the value on the zero position and the next one on position +0.5mm (that corresponds

to the minimum intensity value recorded in this set of measurements) is of the order of 7dBs around −25dBs. The data points corresponding to the negative positions show a trend different from the expected one as the are not specular to the one on the negative positions. This will have to be investigated as it could mean that the SPP not being physically symmetric as the q-plate may have an effect.

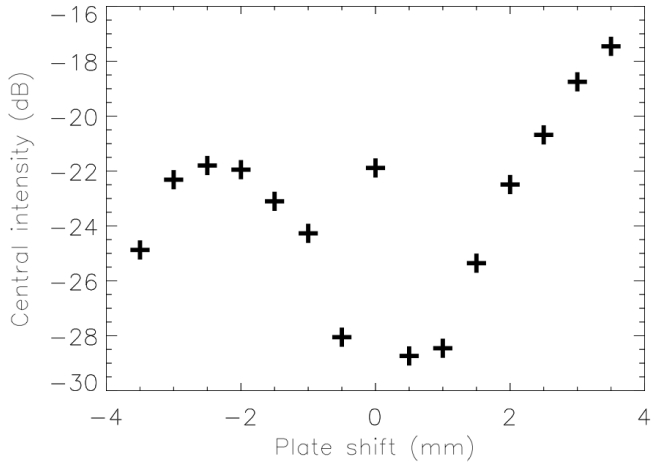

Figure 4.21: Central intensity value of the beam for each position of the plate. The plate is shifted in both directions by 3.5 mm at half millimetre intervals.

In figure 4.22 the value of the intensity on the two peaks of each beam cut is shown. The two peaks are expected to become asymmetric as the plate is displaced from the central position and they should be equal when the plate is centred. It can be seen on the plot that the first (red) and second (green) peaks along the beam cut are more asymmetric the more the plate is out-of-centre as expected, but they are equal for a position different from zero. This can be explained by the fact that on the zero position the intensity peaks are not equal indicating an initial misalignment in the setup or that the generated vortex centre does not correspond to the geometrical centre of the SPP. This data, together with the ones reported in figure 4.21 suggest that the plate could be misaligned with respect to the beam axis by about 1.5mm. Another possibility, as mentioned above, is that the plate is aligned but the generated vortex singularity does not correspond to its centre.

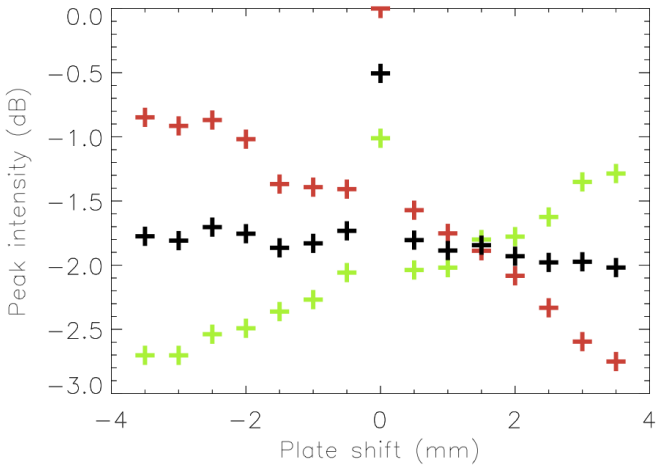

Figure 4.22: Intensity value of the first (red) and second peak (green) and their average (black) for each position of the plate. The plate is shifted in both directions by 3.5 mm at half millimetre intervals.

In figure 4.23 the data points represent the value of the difference between the peaks average intensity (calculated between the two peaks of a single beam cut) and the value at the centre of the beam. The maximum value should be found on the zero position of the plate and become larger as the plate is displaced. Since this plot is complementary to the one in figure 4.21 the same considerations apply.

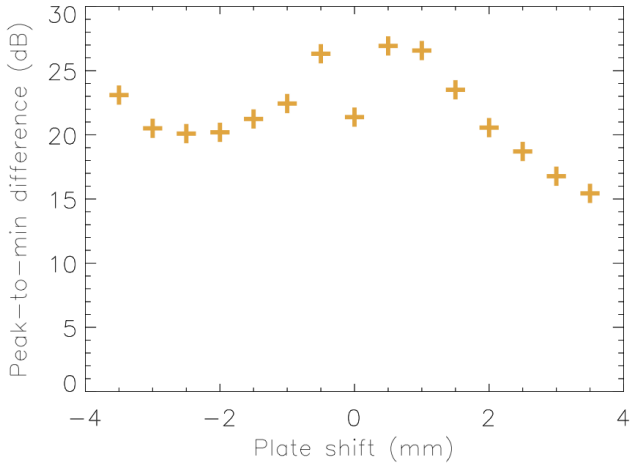

Figure 4.23: For each shifted position of the plate the difference between the average peak value for that beam cut and the minimum (purple) or the central point (orange).

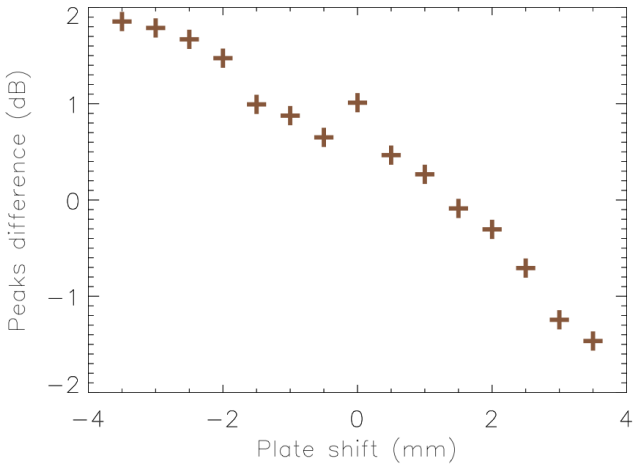

Figure 4.24: Each point of the plot represent the difference between the two peaks of the intensity pattern for a single shifted position of the plate.

In figure 4.24 the difference between the two peaks intensity for each beam cut is reported. If the system was perfectly aligned and symmetric the zero value should be

found at the zero position as the two peaks are expected to be equal.

4.3.4 Beam cuts for different tilted positions of the SPP

With the same conditions as the previous series of measurements data was collected for the plate when the plate was tilted rather than horizontally displaced (see figure 4.25). The same series of plots with new data is reported. Beam cuts were taken for each tilted position of the plate and at intervals of one degree. The plate was moved by six degrees on both sides. From the beam cut the central intensity value (figure 4.26), the peak intensity (figure 4.27), the peak to central minimum difference (figure 4.28) and the difference between the two peaks (figure 4.29) were extracted. All the data was collected at 100 GHz which is the operating frequency of the plate.

All the comments to the plots in the previous section seem to apply for the measurements taken for different tilted positions of the plate.

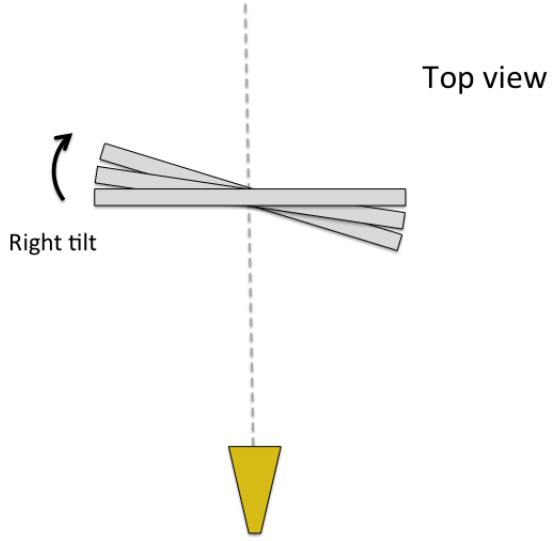

Figure 4.25: A transverse horizontal beam cut is taken for different tilted positions of the plate with respect to the central aligned position. The more the plate is tilted with respect to the beam axis the more the intensity pattern becomes asymmetric. If the alignment in the central position is accurate, an evaluation of the peaks asymmetry can provide information about the size of the plate tilt.

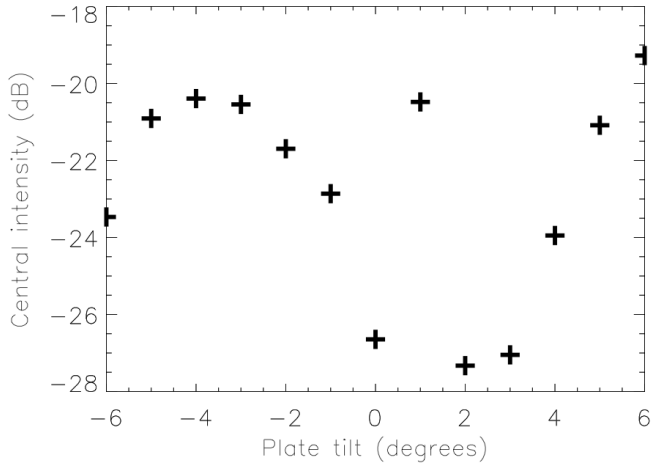

Figure 4.26: Intensity value at the central point of the beam area for each position of the plate. The plate is tilted in both directions by six degrees at one degree intervals

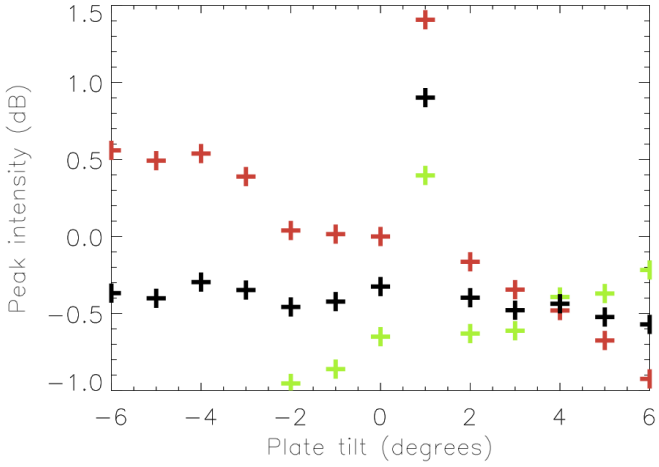

Figure 4.27: Intensity value of the first (red) and second peak (green) and their average (black) for each position of the plate. The plate is tilted in both directions by six degrees at one degree intervals.

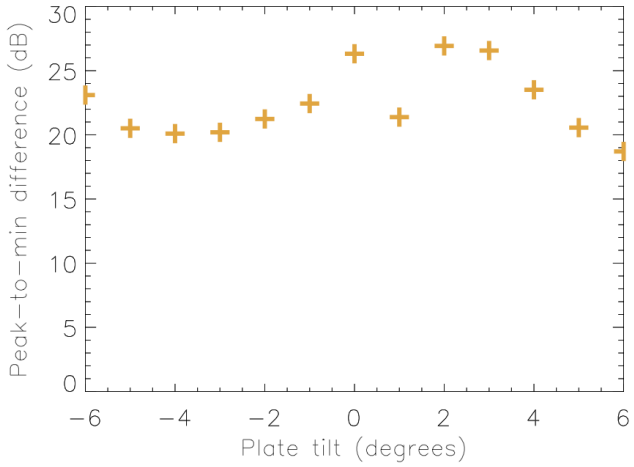

Figure 4.28: For each tilted position of the plate the difference between the average peak value for that beam cut and the minimum (purple) or the central point (orange).

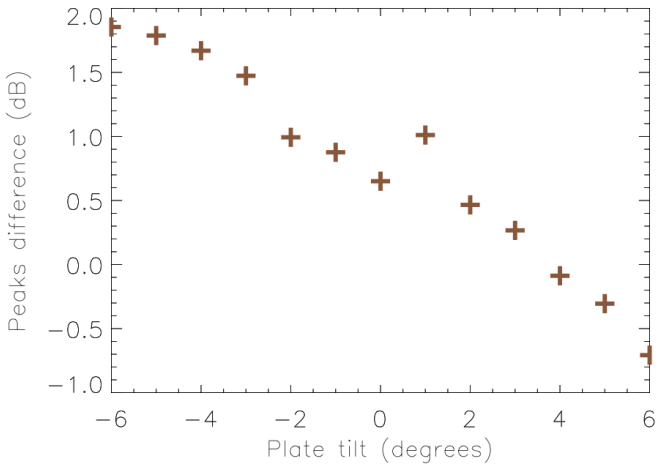

Figure 4.29: Each point of the plot represent the difference between the two peaks of the intensity pattern for a single tilted position of the plate.

4.3.5 Beam cut measurement at non-optimal frequencies

The following two plots (figure 4.30 and 4.31) are meant to show the difference between the generated beam at frequencies that the plate was not designed for. Specifically, transverse beam cut measurements were performed along the diameter of the plate rotating the emitting horn and the plate as usual. The beam cut has been taken at two perpendicular directions, one of which overlaps with the length of the plate's step. Data are for six different frequencies within the W-band are shown.

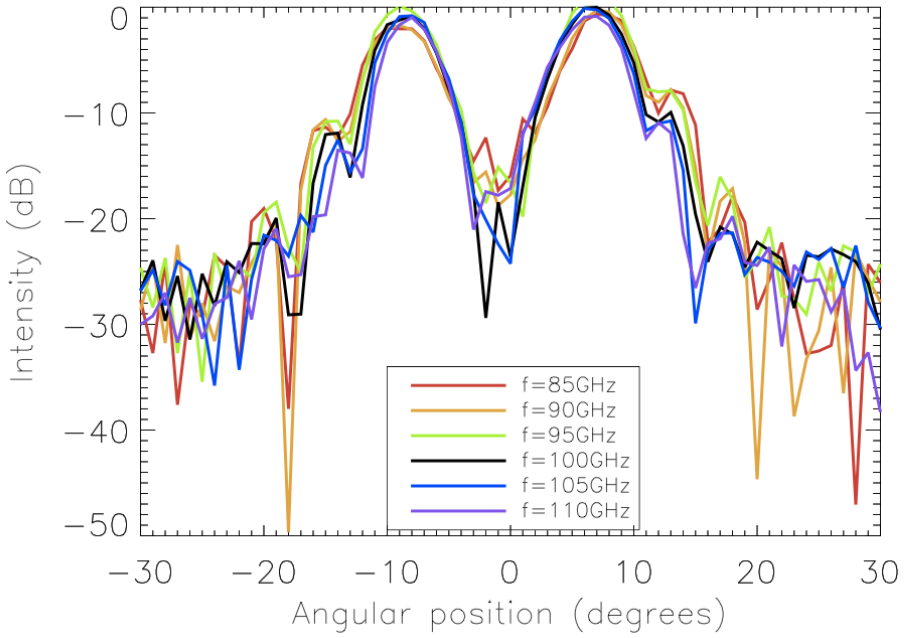

Figure 4.30: Beam cut on the transverse plane at an azimuthal angle normal to the direction of the plate's step. The intensity profile is plot for the six different frequency in the W-band reported in the legend.

In both the plots it can be notice that the vortex beam is present for all the frequencies across the W-band with a central minimum depth that is maximum at 100 GHz. The main difference between the beam cuts at different frequencies is the dispersion angle. It can be seen that the beam is more focused for higher frequencies

and spread out as the frequency decrease. The beam central intensity is higher for non optimal frequency and this means that the plate is not converting all the fundamental Gaussian beam to a mode |2| L-G beam with the same efficiency as for 100 GHz. However, the on axis intensity remains under −12 dBs. It is reasonable to state that the plate is generating an optical vortex across the whole band. It would be interesting to extend the measurements on a wider band and evaluate the exact frequency range on which the plate can be considered effective. This will be the object of further simulations and tests.

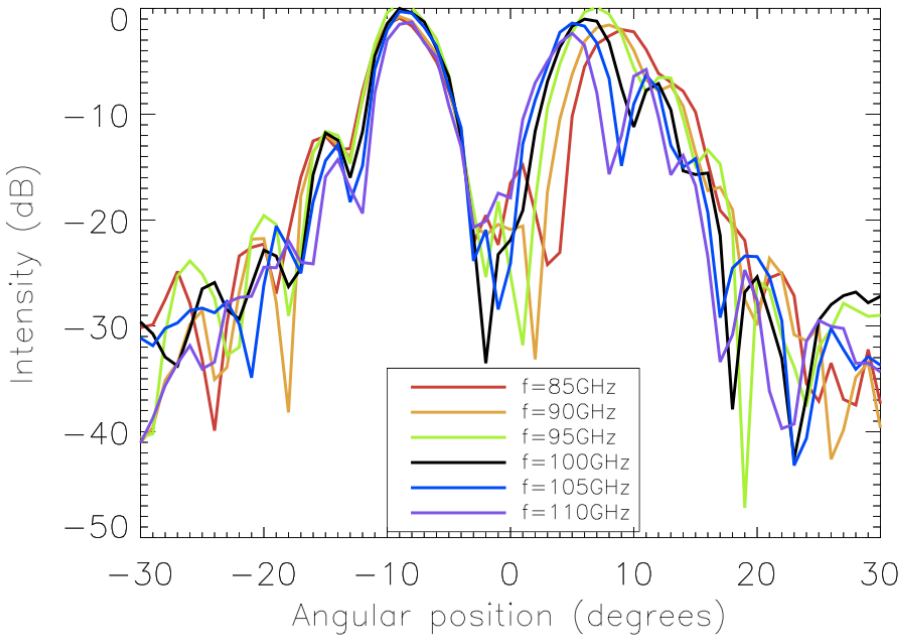

Figure 4.31: Beam cut on the transverse plane along the direction of the step in the plate. The intensity profile is plotted for the six different frequencies in the W-band reported in the legend.

Figure 4.31 shows beam cuts measured in the same way as in figure 4.30 but this time the plate is azimuthally rotated so that the beam cut is performed along the direction of the step. This was done in order to see if the big surface discontinuity due to the step can influence the symmetry of the intensity patter and if such effect

varies with the frequency. It is clearly visible that when the beam cut is performed along the step edge the diffractive effect of the step becomes evident. The diffraction results in a change of the position of the peak on the step side. Looking in a deeper way at this effect could help manage systematic effects in cases where the plates are used for observations or other application where such effects have to be taken into account.

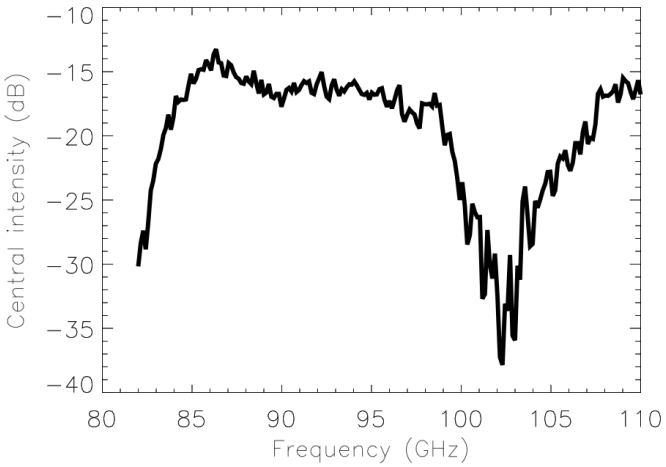

Figure 4.32: On axis value of the intensity for all the frequencies in the W-band.

In figure 4.32 the on axis value of the intensity is plotted as a function of the frequency. A deeper negative peak is found very close to the 100 GHz frequency even if not exactly on it. This may be due to the manufacturing precision. The steps height or the added layer for the matching not being perfectly right could cause this shift. The same comment is valid for the data in figure 4.35 which represent the difference between the average peak intensity across the beam cut and the on-axis value of the intensity. If the the plate was designed to work at 102 GHz the SPP's step would be of a different height. Calculating it with the equation in (3.13) lead to the result $h_s = 11.6\,\text{mm}$. The step hight of the actual SPP for 100 GHz is 12 mm, the difference between the two being 0.4 mm. As reported in Section 3.4 the evaluated machining error is $\pm\,0.05\,\text{mm}$ on each cut. This means that, in the worst case scenario where all the mistakes have the maximum absolute value and they all sum up, the error on

the SPP step would be 0.1 mm on a different between the steps heights for the two frequencies of 0.4 mm.

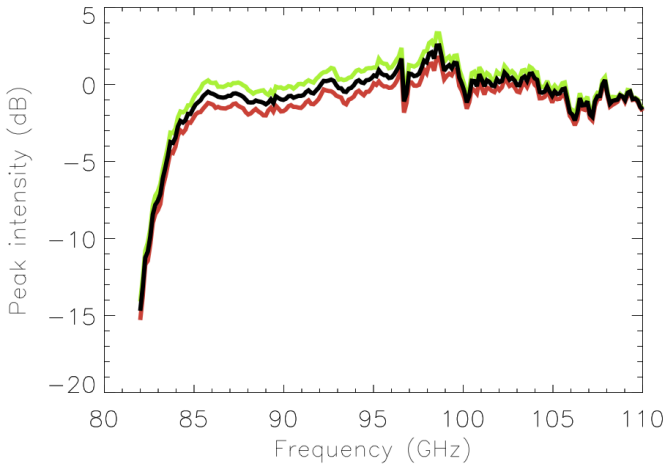

Figure 4.33: Intensity value of the left peak (green), right peak (red) of the transverse beam cut and their average (black) for all the frequencies in the W-band.

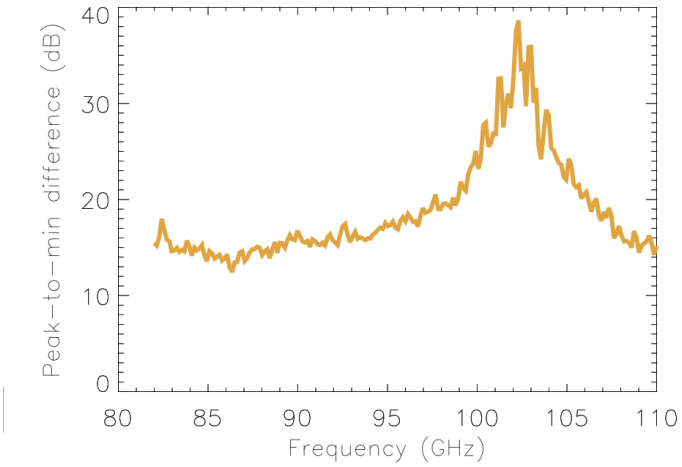

Figure 4.34: The difference between the average peak intensity of the transverse beam cut and the on-axis value plot as a function of the frequency across the whole W-band.

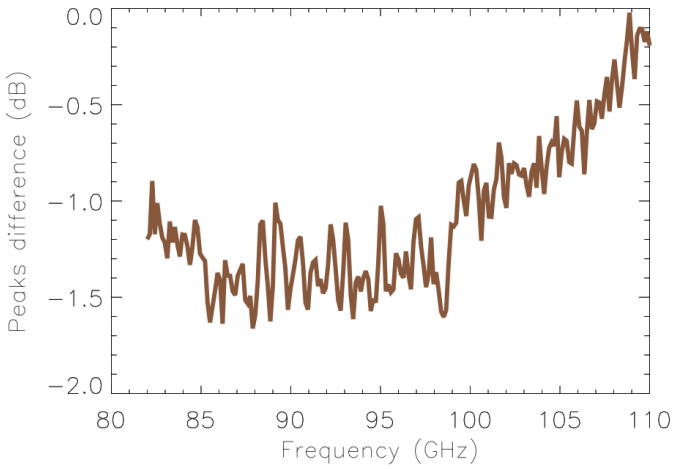

Figure 4.35: The plot represent the difference between the two peaks of the intensity pattern for all the frequencies across the W-band.

4.3.6 3D near field scanning system

The 3D near field scanning system was designed and developed after seeing how promising the 2D field measurements for the q-plate were. Data was already good considering the early stage of our research in radio vortices. However developing a proper volume scanning system would provide the chance to actually see the 3D structure of the beam and the evolution of the phase and intensity profile.

Considering all the plates are designed to work at 100 GHz and the input beam waist is a few millimetres wide, the 3 axis system has been designed to span a volume of 50 cm × 50 cm × 50 cm.

In order to do so, four HepcoMotion [2] linear actuators were assembled to allow movement in the x, y and z directions as shown in Figure 4.37. Specifically, three belt driven rail units were used for the x and z axis and a screw driven rail unit was used for the y axis. The rail unit was chosen so the y axis would be screw driven as it is working against gravity. Moreover it needs to be particularly stable as it has to support and move the platform with the probe VNA head.

Each axis's movement is controlled by a stepper motor and all of them are

interfaced by a gear box so that it is possible to choose the single step length independently according to the resolution one wants to achieve. The intrinsic step length is however much smaller for the y-axis screw driven unit than for the other units because of the intrinsic structure of the part.

The whole scanner is wired to a board connected to our lab computer and controlled through a LabView dashboard developed by colleague Peter Schemmel like most of the near-field scanner [57]. Through the dashboard all the necessary parameters can be set. The total length to be scanned can be set (independently for the 3 axes), as well as the gear ratio, the number of frequency points (as the frequency range is potentially from 75 GHz up to 110 GHz) and the number of sweeps for a single scan so to obtain an average over a series of measurements for each data point.

For all data reported in this chapter that were taken using the near field scanner the 100 GHz frequency only was recorded and each data point is the result of 10 sweeps, meaning it's the average of 10 independent measurements.

A rectangular-to-circular waveguide transition (W-10) designed for the W-band was used as a probe.

The transition is matched to free space and presents a return loss of 34.4 dB at 100 GHz as reported in [57]. It can be seen in figure 4.3.6 that a 3D printed pyramidal plastic absorber was placed round the probe in order to reduce reflections from metal surfaces.

Data was taken every 3.6 mm along x and z and every 3.75 mm along the y direction for all the plane scans. Moreover, for the vortex beams the $x-y$ scans were taken multiple times along z at a distance of 0.01875 mm so to obtain several scans within the space of a wavelength in order to better visualise the phase behaviour. All the measurement parameters are summarised in Figure 4.38.

As part of the validation procedure previously performed by my colleague Peter Schemmel for this new equipment, a far field linear beam scan of the beam generated by the corrugated horn only was taken (figure 4.36) and compared with a simulation made with the FEKO [64] software showing very good agreement [57].

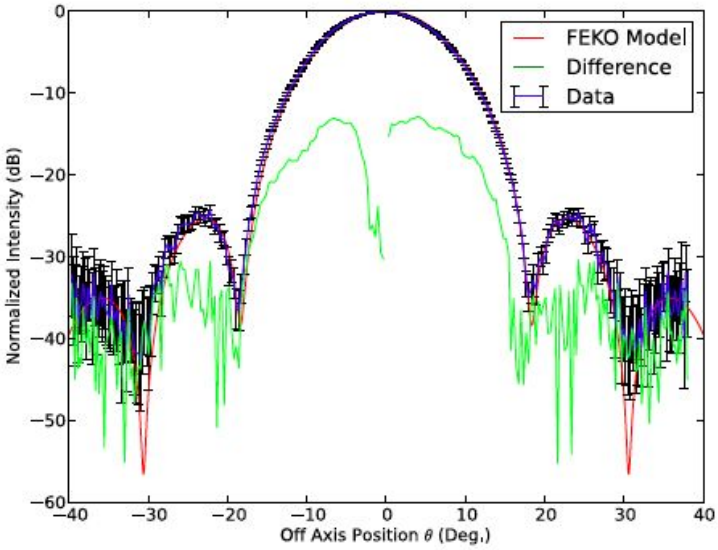

Figure 4.36: Transverse cut of the corrugated horn beam at 100 GHz from the 3D scanner validation paper by P. Schemmel et al. [57]. The intensity in dBs is reported and compared to the corresponding FEKO model.

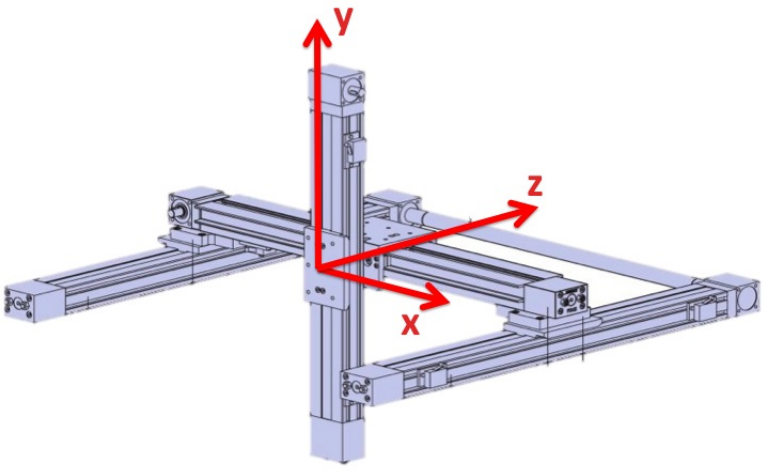

Figure 4.37: Definition and orientation of the x, y and z axis on the moving system. The 3 axis system drawing was taken from the HepcoMotion catalogue for linear motion actuators.

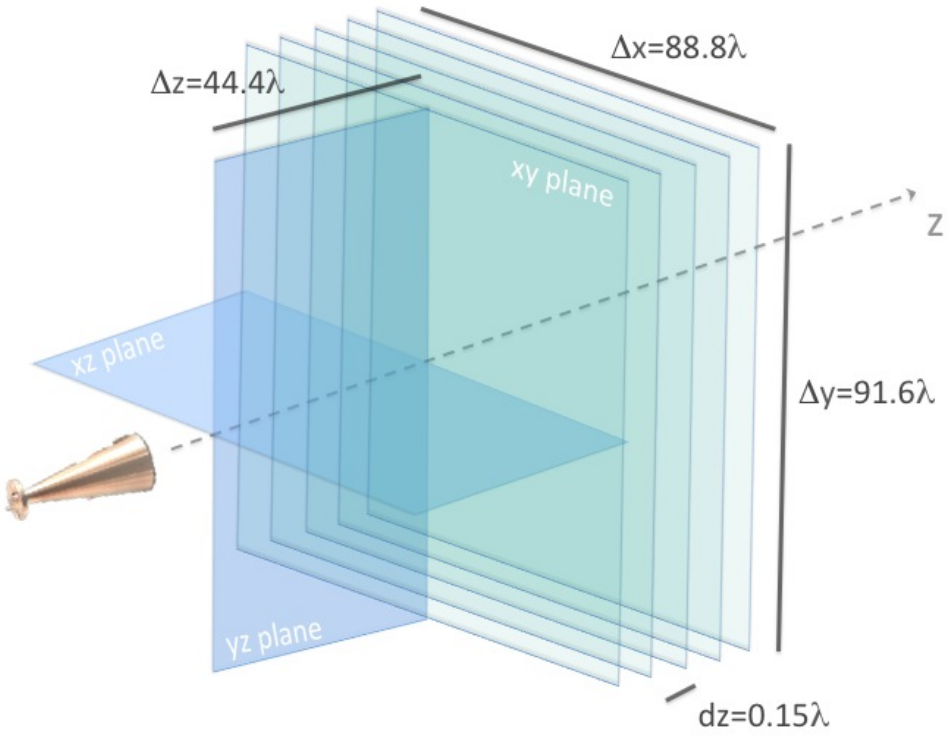

Figure 4.38: Illustration of the measurement planes and scanning dimensions for the 3D near field scanner (not to scale).

The measurements performed with the 3D near field scanner setup exceeded our expectations in terms of quality. They are the best data of a millimetre vortex available to our knowledge at the present date. An initial paper reporting part of them to show what can be achieved with this setup has been just published [58]. Further study and data analysis will be performed on the collected data. The data collected for the corrugated horn beam need to be corrected for the probe beam pattern through deconvolution and for geometrical factors due to the fact that we are scanning on a flat plane as explained. For the SPP data it is not yet clear which corrections need to be taken into account as the complex structure of the plates and the presence of a number of steps around the plate's surface may cause peculiar diffractive effects as well as standing waves. This will be the object of further investigations in future work. No correction is applied to the data reported here but

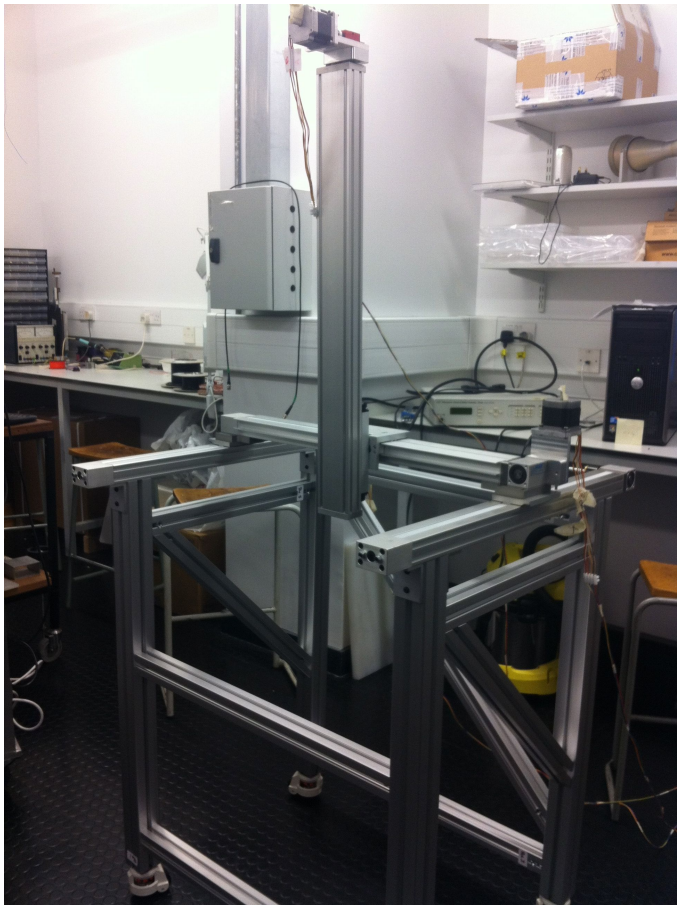

Figure 4.39: Support frame and moving 3D scanning system in the RF lab.

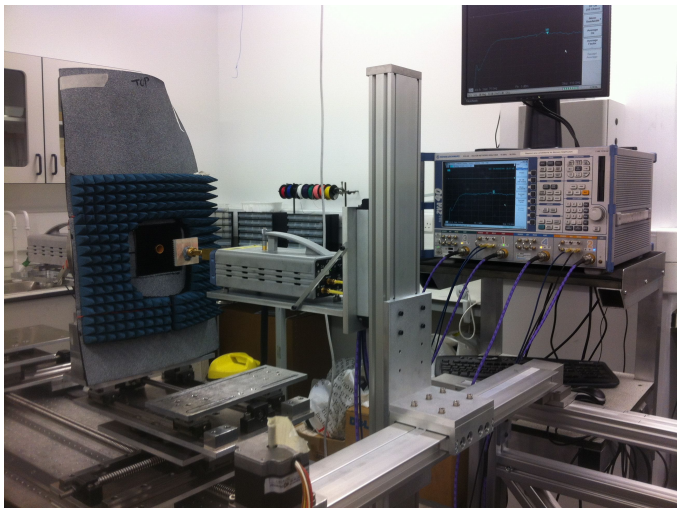

Figure 4.40: Detail of the scanning setup in the RF lab. On the left, the source horn surrounded by pyramidal Eccosorb, on the right, the VNA head with the probe surrounded by 3D printed pyramidal absorbent, on the support stage mounted to the y axis of the 3D scanner. In the background the VNA used to collect the data.

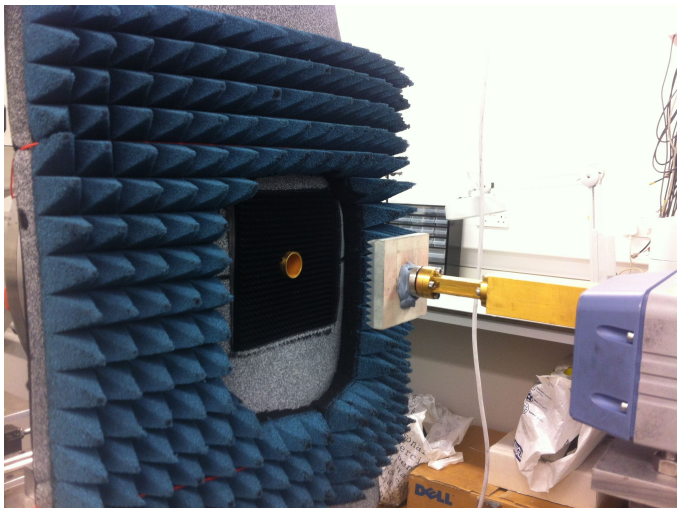

Figure 4.41: Aligned source horn and probe.

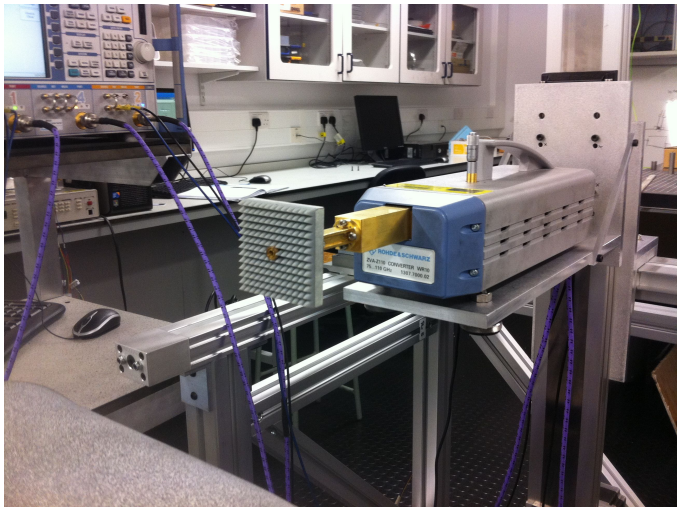

Figure 4.42: The probe surrounded by the 3D printed plastic absorbent.

the information about the validation of the system and about the corrections to be applied are reported in Schemmel's paper [57]. Everything reported here is raw data as collected using this instrumentation. Linear orthogonal scans on planes parallel to the plates were taken and plotted for both the magnitude and the phase of the field as shown in fig. 4.43 for all the plates. Additionally the phase is recorded on the 9 planes at different z (see figure 4.38) on 4 different points around the centre of the vortex (which may not be the centre of the scanning area) [58].

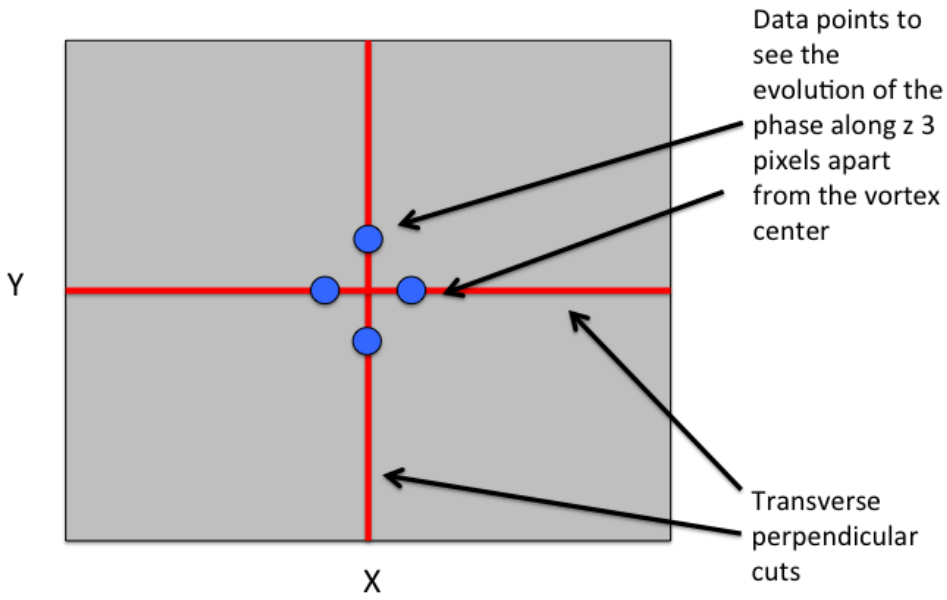

Figure 4.43: Illustration of the measurement cuts and point dimensions for the tests on the smooth SPP |1|, the wedge SPP |2| and the split ramp wedge SPP |2|.

For the wedge SPP mode |1| only the full data collected by the system are shown so we can see the 2D plane intensity and phase pattern on the $x-z$ (Figure 4.50), $y-z$ (Figure 4.51) and transverse plane $x-y$ (Figure 4.52) and the evolution of the phase pattern along z (Table 4.4). Full data was collected for the W-band Winston-like corrugated horn beam for comparison.

4.4 W-band Winston-like corrugated horn

Results obtained with the source antenna only using the previously described experimental setups.

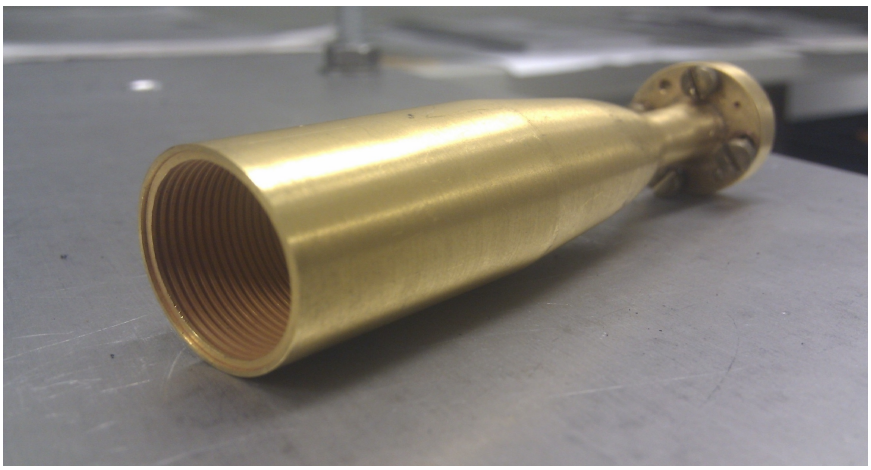

Figure 4.44: The W-band Winston-like corrugated horn that was used as the emitting antenna in all the measurements with the 3D scanner. The characteristics of the horn are reported in [38].

Starting from the horn beam with no plate interposed (figure 4.45, 4.46 and 4.47) the intensity (dBs) and phase (deg) data for the three different cuts illustrated in figure 4.38 are reported. Only the first (closest to the horn) $x-y$ plane was considered. It was chosen to measure only one $x-y$ plane here because the measurements were extremely time consuming and the intensity and phase pattern of the horn beam are not expected to change along the z direction as it is an almost pure fundamental Gaussian mode.

As expected the beam's transverse intensity profile is perfectly Gaussian and the phase is flat in the central part of the main beam area (indicated by the -3dB contour line on the intensity plot in figure 4.47).

It is reasonable to say that the input beam was good enough for phase measurements of the output beam after the interaction with the SPPs.

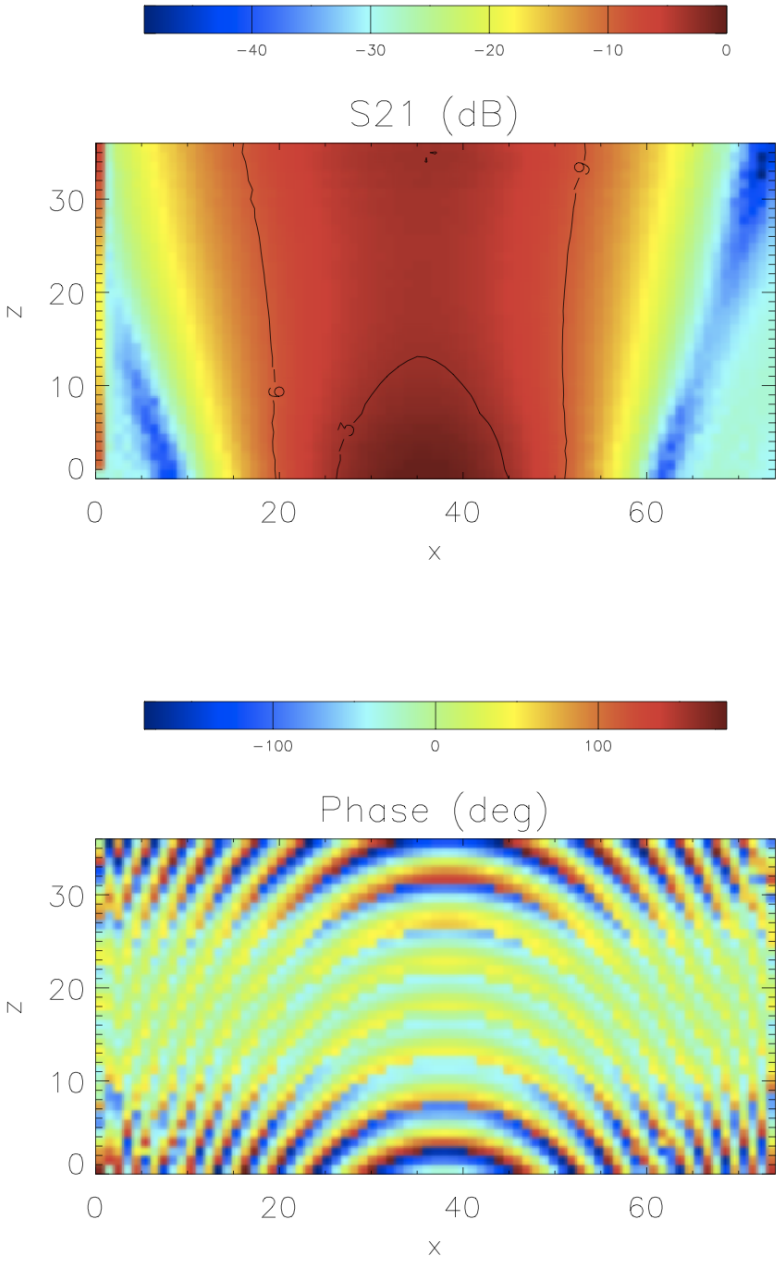

Figure 4.45: Intensity in dBs (a) and phase in radians (b) measured on the $x-z$ plane cutting through the centre of the beam generated by the horn only.

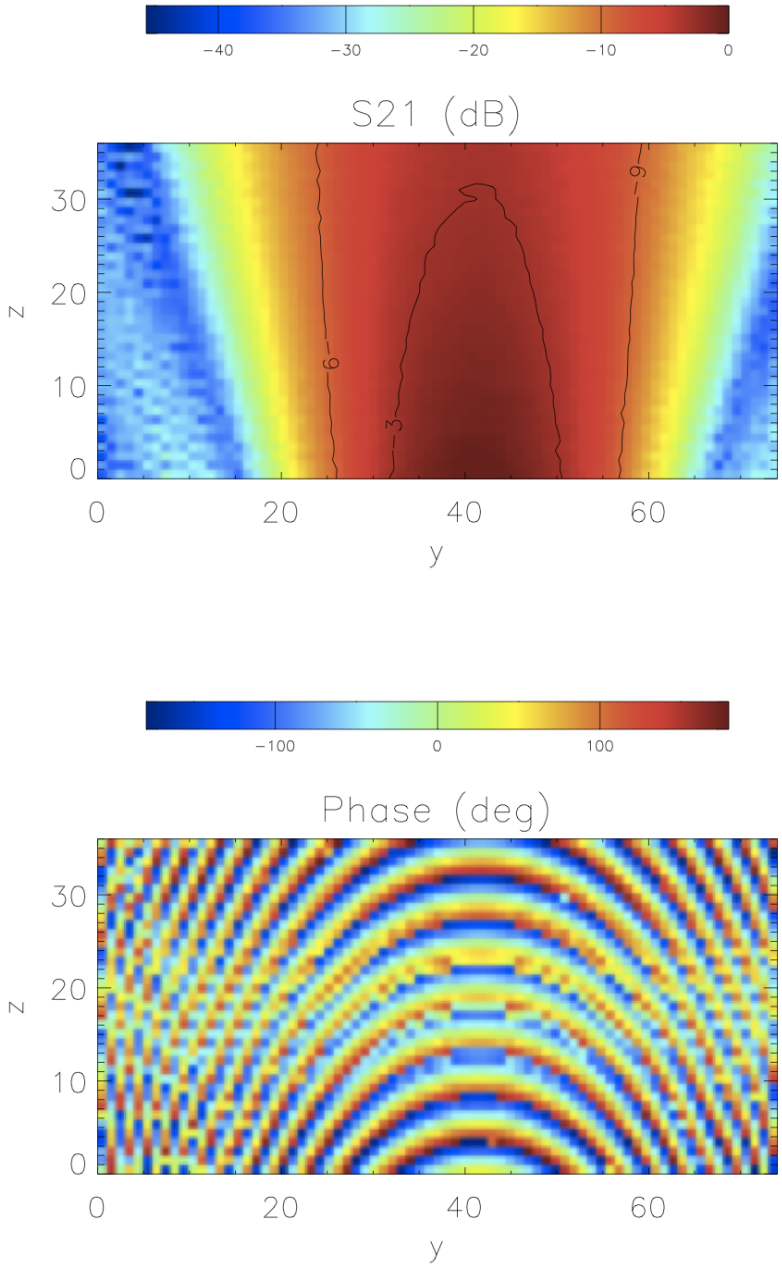

Figure 4.46: Intensity in dBs (a) and phase in radians (b) measured on the $y-z$ plane cutting through the centre of the beam generated by the horn only.

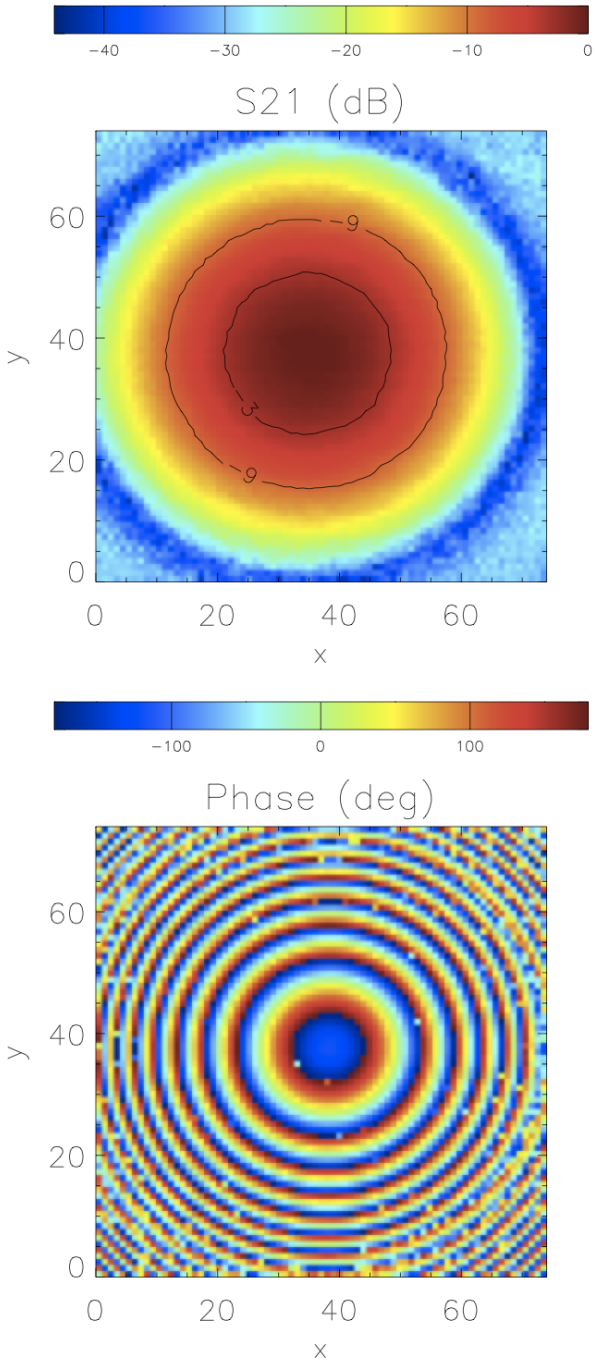

Figure 4.47: Intensity in dBs (a) and phase in radians (b) measured on the $x-y$ plane at distance $z = 111.1\lambda$ from the horn.

4.5 Mode |1| smooth Polypropylene SPP

Results obtained with the smooth SPP mode —1— using the experimental set-ups previously described.

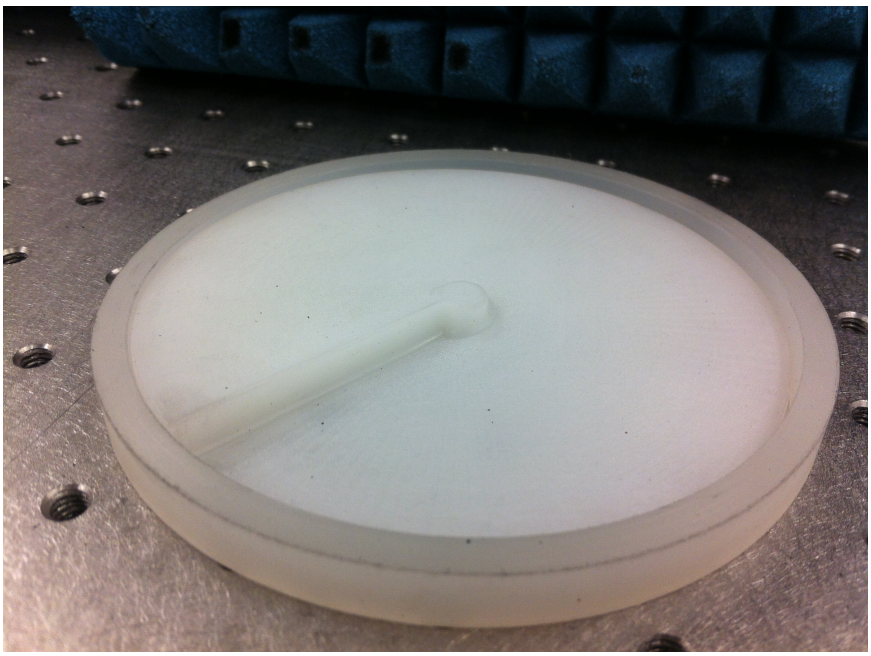

SPP specifications	
Δl imprinted,	|1|
Meterial,	Polypropylene
Refractive index,	$n = 1.5$
Smooth surface	
Total step height,	$h_s = 6mm$

Table 4.2: Mode |1| smooth SPP specifications

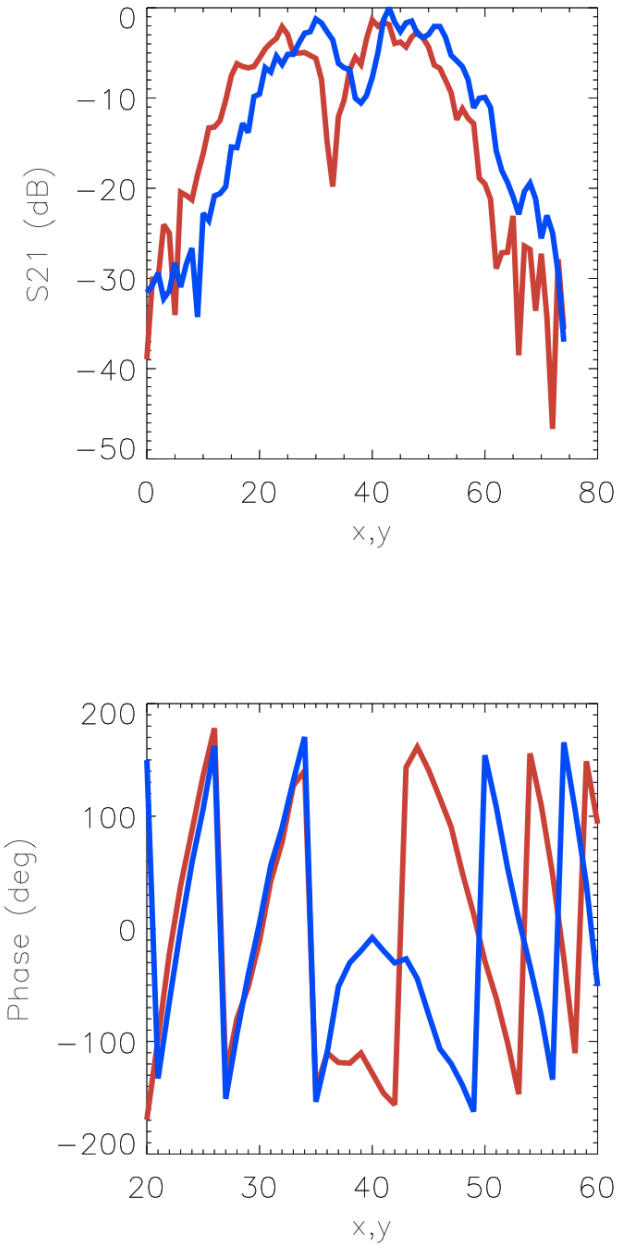

Figure 4.48: Intensity (top) and phase (bottom) of the vortex beam generated with the mode ±1 SPP with smooth surface. Data is collected on horizontal (red) and vertical (blue) cuts on a plane normal to the propagation direction, at a distance of 45.6λ from the plate (see figure 4.43)

In figure 4.48 the data collected on the beam generated by the horn beam passing through the mode |1| SPP with smooth surface are shown. In the $x-y$ plane intensity data the central void is clearly visible as expected. However, the null is not as clear and symmetric as desired, most likely because of the plate's central cylinder. The central point of the plate is very important as it corresponds to the beams singularity region. Using a SPP with such a structure could result in a loss of mode conversion efficiency unless the manufacturing process is improved to higher precision. The intensity pattern in fact shows some degree of asymmetry most likely due to the non optimal manufacturing of the SPP.

In the following figure (4.49) the transverse phase data for four points around the beam singularity are reported (see Fig. 4.43). Data was collected at 9 different distances within the space of a little more than a wavelength to show the phase front rotation through propagation. The expected phase period along z is visible.

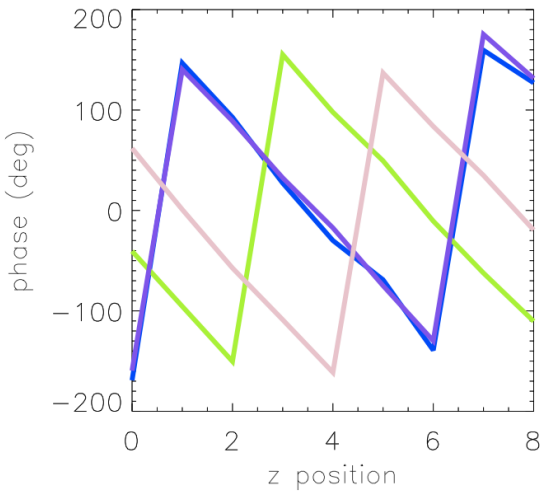

Figure 4.49: Phase evolution on 9 planes along the z direction collected on four points around the vortex centre as shown in figure 4.43 for the smooth SPP |1| beam.

4.6 Mode |1| wedge Polypropylene SPP

Results obtained with the 16 wedge SPP mode 1 using the previous described experimental setups.

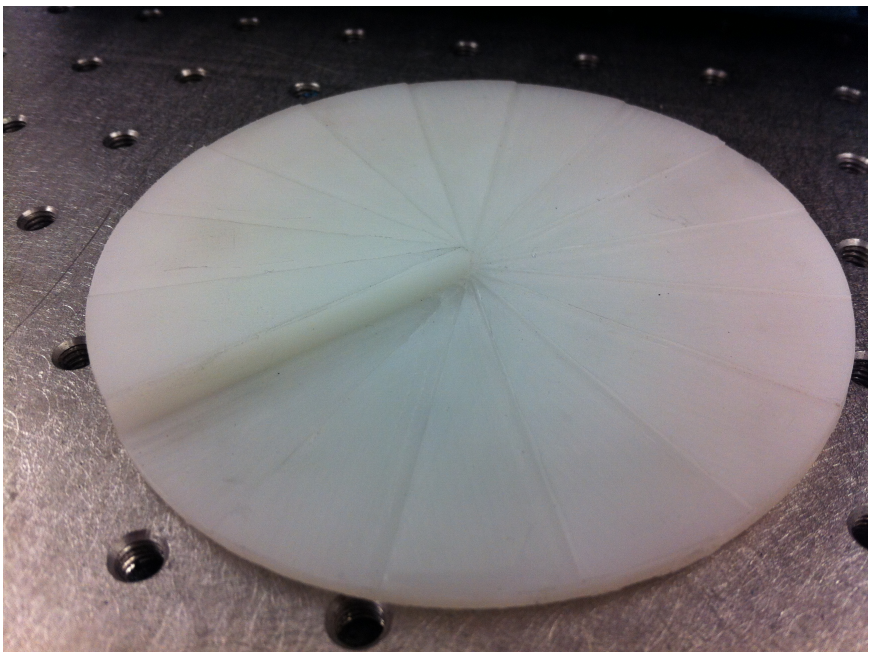

SPP specifications	
Δl imprinted,	|1|
Material,	Polypropylene
Refractive index,	$n = 1.5$
Wedges,	16
Total step height,	$h_s = 6mm$
Single step height,	$h_{s/16} = 0.4mm$

Table 4.3: Mode |1| wedge SPP specifications

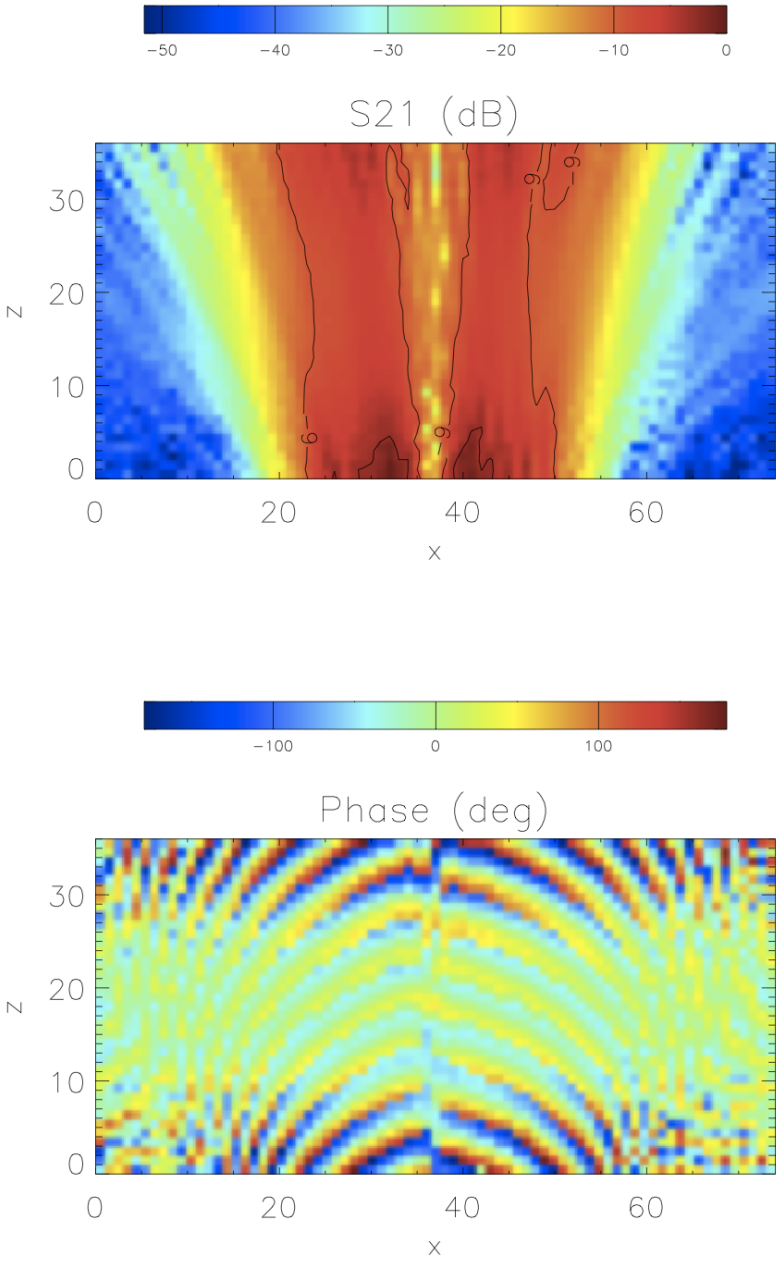

Figure 4.50: Intensity in dBs (a) and phase in radians (b) measured on the $x-z$ plane cutting through the centre of the beam generated by the horn Gaussian beam passing through the 16 wedge mode ± 1 SPP.

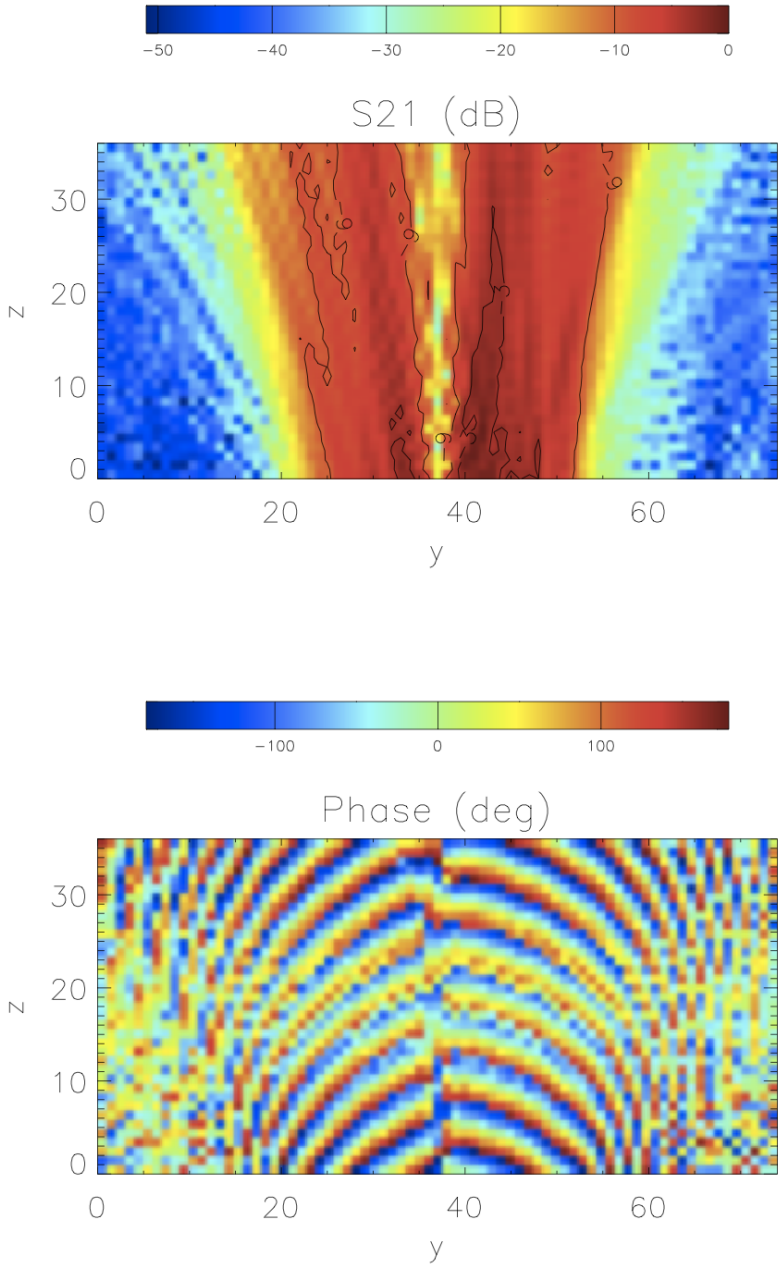

Figure 4.51: Intensity in dBs (a) and phase in radians (b) measured on the $y-z$ plane cutting through the centre of the beam generated by the horn Gaussian beam passing through the 16 wedge mode ± 1 SPP.

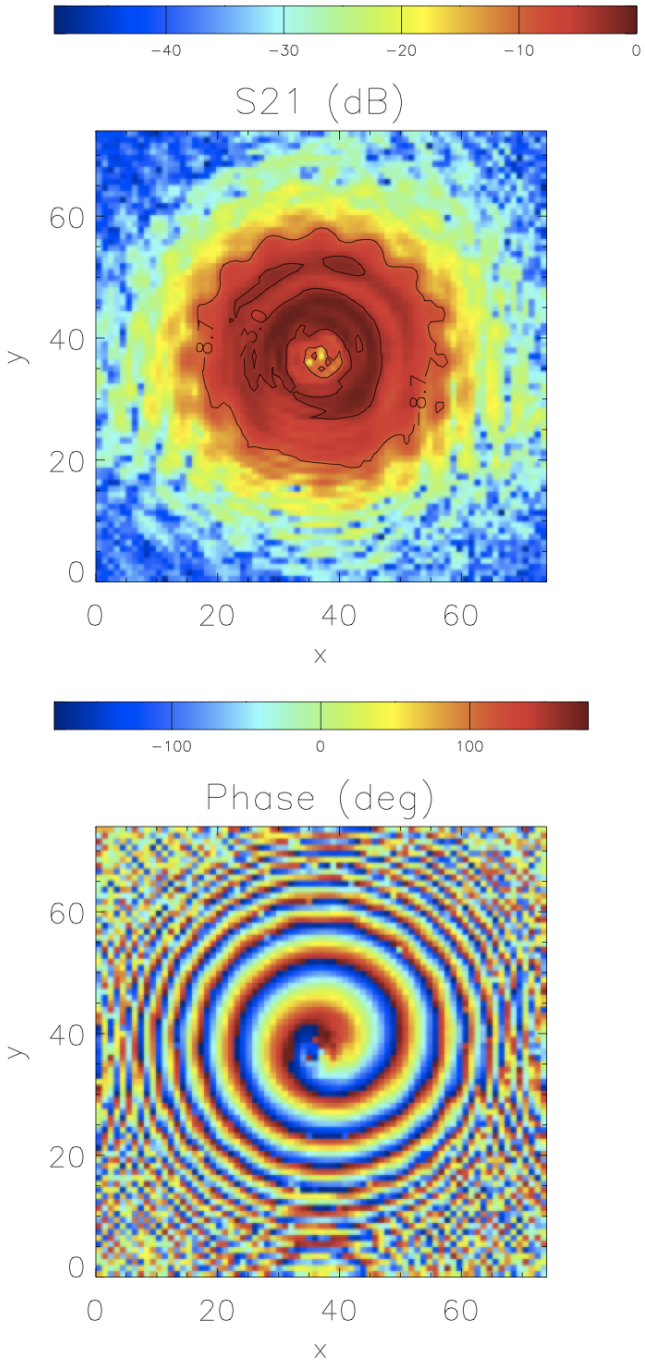

Figure 4.52: Intensity (top) and phase (bottom) of the vortex beam generated with the mode ± 1 SPP with wedges (16 steps). Data is collected on an 88.8λ x91.6λ x1.2λ volume, normal to the propagation direction, at a distance 44.4λ from the plate. Data is shown on planes 0.15λ apart from each other.

The data in figure 4.50, 4.51 and 4.52 represent a better version of the one in the previous paragraph even if a full 3D version should be compared. The mode |1| smooth SPP has been replaced here with wedge SPP that generates the same mode. The stair structure of the plate allowed the milling tool to achieve a much better precision at the centre of the plate. The steps do not seem to affect the output phase significantly. In the $x - z$ and $y - z$ data it is possible to notice that the beam's central area is clearer and more defined and the phase discontinuity sharper.

The $x - y$ intensity pattern seems to be more symmetric but the effect of the multiple steps is clearly visible in the irregular contour of the outer main beam area.

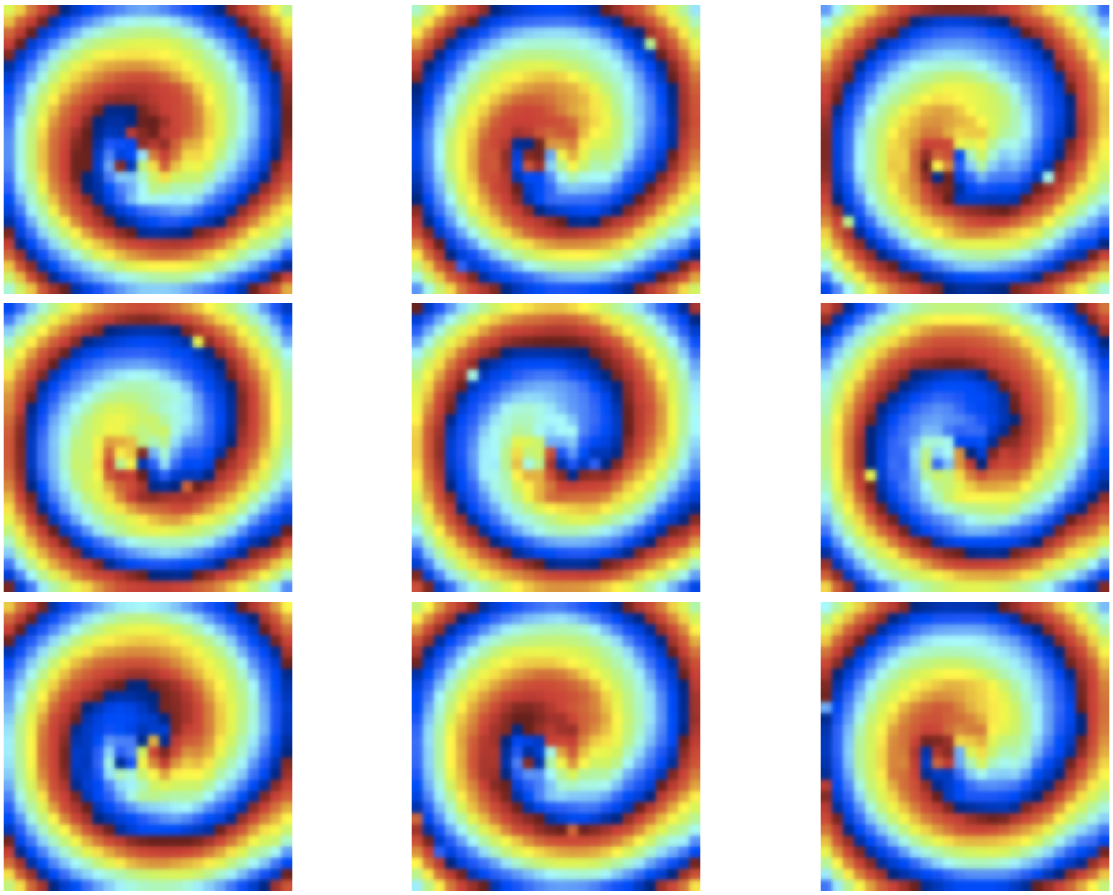

Table 4.4: From top left to bottom right are reported the sequences of $x - y$ scans that have been taken every 0.15λ along z. Only the central part of the scans is reported in order to enphasise the rotation of spiral phase structure around the propagation axis which is normal to the scan plane.

4.7 Mode |2| wedge Polypropylene SPP

Results obtained with the 32 wedge SPP mode 2 using the experimental set-ups described previously.

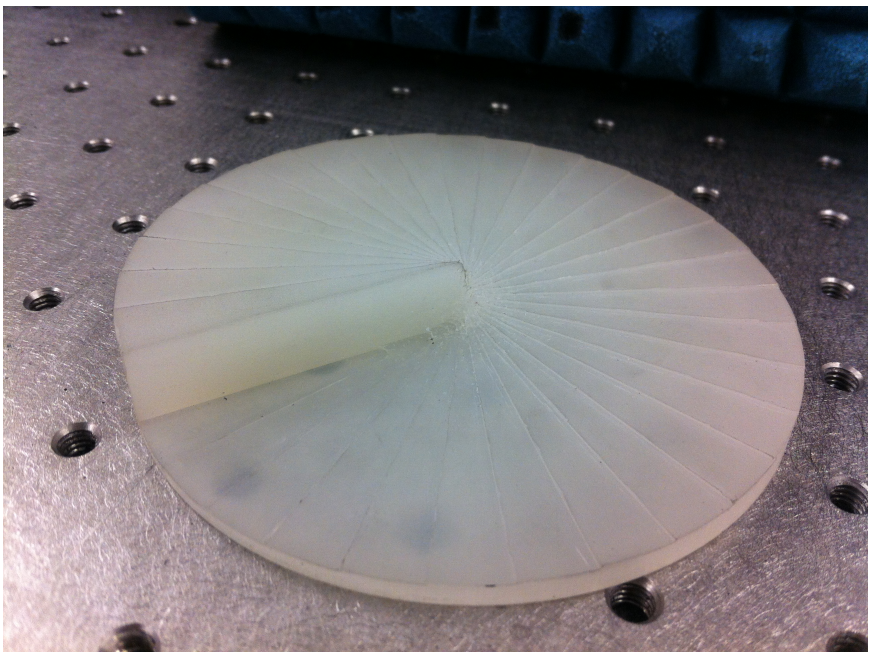

SPP specifications	
Δl imprinted,	$\|2\|$
Material,	Polypropylene
Refractive index,	$n = 1.5$
Wedges,	32
Total step height,	$h_s = 12mm$
Single step height,	$h_{s/32} = 0.387mm$

Table 4.5: Mode |2| wedge SPP specifications

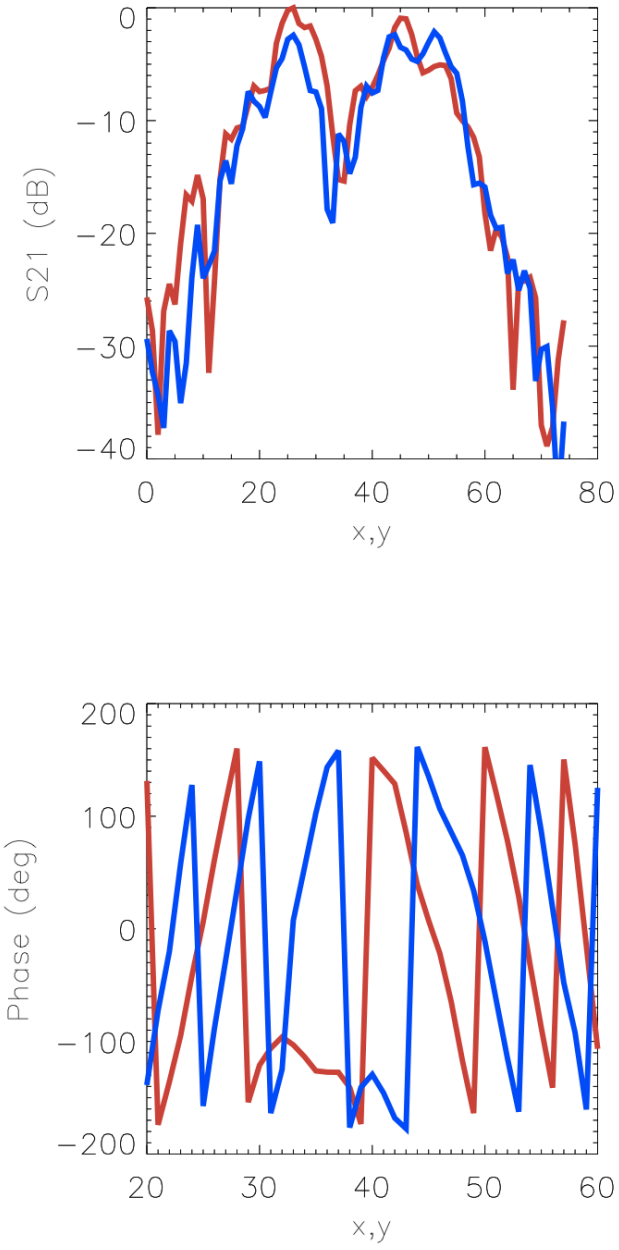

Figure 4.53: Intensity (top) and phase (bottom) of the vortex beam generated with the wedge mode ±2 SPP. Data is collected on horizontal (red) and vertical (blue) cuts on a plane normal to the propagation direction, at a distance of 45.6λ from the plate (see figure 4.43).

As expected for a mode |2| OAM beam the inner, in principle null, area of the beam becomes wider. From the same data it is possible to notice that the beam spreads asymmetrically. It is assumed that this is due to the relatively big main step of the plate and its diffractive effect. The transverse phase data (figure 4.53) clearly show the behaviour expected for a mode |2| vortex.

The central part of the vortex, however, shows a slightly complex structure different from the ideal one that will require further investigation. It has to be understood how this could be related to manufacturing imperfections, number of wedges or other effects.

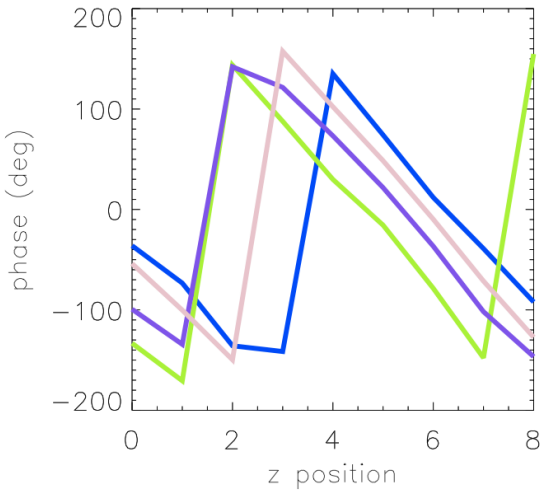

Figure 4.54: Phase evolution on 9 planes along the z direction collected on four points around the vortex centre as shown in figure 4.43 for the wedges SPP |2| beam.

In figure 4.54 the expected phase period along z is visible.

4.8 Mode |2| wedge Polypropylene SPP

Results obtained with the 32 wedge SPP mode 2 with split ramp using the experimental set-ups previously described.

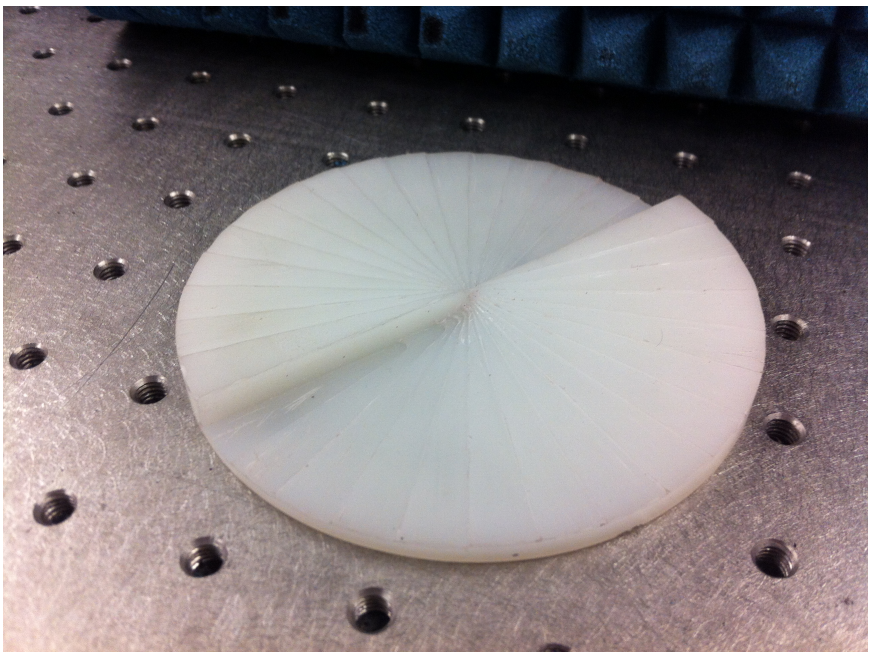

Figure 4.55

SPP specifications	
Δl imprinted,	|2|
Material,	Polypropylene
Refractive index,	$n = 1.5$
Wedges,	32
Total step height,	$h_s = 12mm$
Single step height,	$h_{s/32} = 0.387mm$

Table 4.6: Mode |2| wedge split SPP specifications

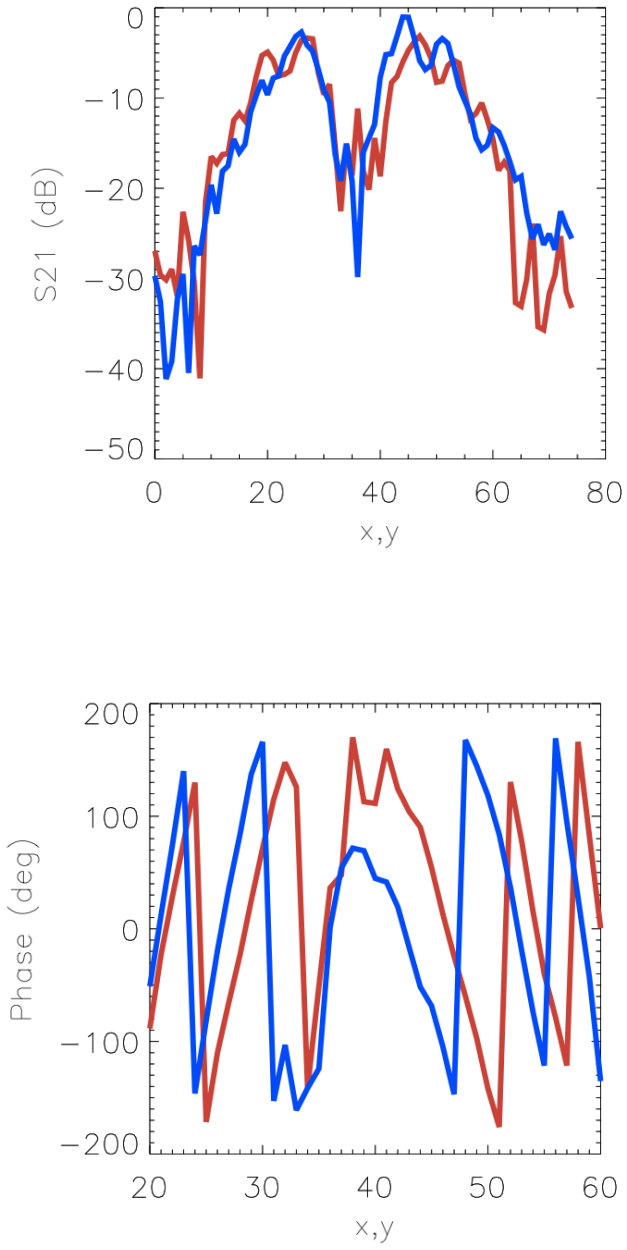

Figure 4.56: Intensity (top) and phase (bottom) of the vortex beam generated with the mode ±2 wedge SPP with split ramp. Data is collected on horizontal (red) and vertical (blue) cuts on a plane normal to the propagation direction, at a distance of 45.6λ from the plate (see figure 4.43).

The same data as in the previous paragraph but for the split ramp mode |2| SPP show a better symmetry of the main beam possibly due to the better symmetry of the plate structure but the central area of the transverse phase is still not perfect.

The evolution of the phase marker points along z is shown in figure 4.57 as for the previous plates.

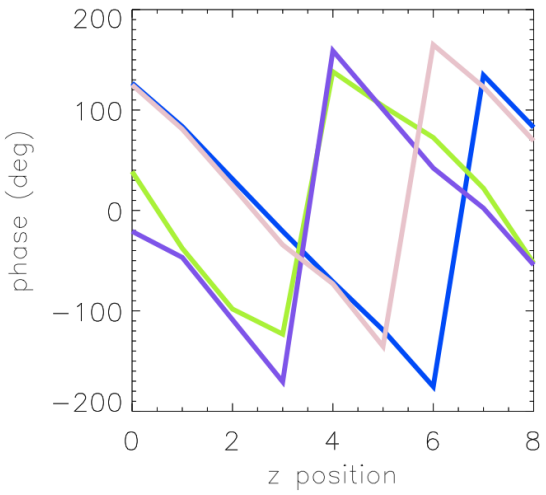

Figure 4.57: Phase evolution on 9 planes along the z direction collected on four points around the vortex centre as shown in figure 4.43 for the wedge split ramp SPP |2| beam.

4.9 Chapter summary

The aim of the experimental work reported in this Chapter was to test that all the SPPs and the q-plate are generating optical vortices with the expected characteristics and to put in place a standard procedure for their testing. As this were the first OAM measurements ever performed in the RF laboratory of the Technology Group the experimental setup changed together with the evolution of the project.For all the experimental measurements a VNA was used together with W-band extension heads and Wiston-like corrugated horns as sources and receivers. The mode |2| q-plate was tested through horizontal transverse beam cuts to measure the intensity pattern that showed the typical double peak expected when an optical vortex is generated. Since the q-plate works with circular polarisation only the necessary SWRs where included in the setup. Changing the relative orientation of these QWRs the HWP behaviour of the q-plate was also confirmed. A different test was performed to map the relative phase shift induced by the birefringence of the plate on the incident wave. The phase data was collected by keeping the source and receiving horns aligned and moving the q-plate to sample the field at different points on an imaginary grid. The expected 4π phase change around the axis was recorded. Moreover, set of measurements were taken with a telescope-like setup to measure the power collected by the horn when the fundamental Gaussian beam or the OAM beam are focused into it. Similar beam cuts, this time not involving the circular polarisation, were performed to test the mode |2| wedge SPP. The expected double peak was found and the symmetry of the ring intensity pattern was confirmed. The beam cuts were measured for a series of configurations, changing the horn-plate distance, the beam-plate alignment or the plate's tilt in order to measure the effects on the intensity pattern. The mode |1| wedge SPP was further tested using the new 3D moving system so that the full 2D phase and intensity pattern was recorded. Moreover, several 2D planes parallel to the plate were scanned changing the distance from the plate along z allowing us to visualise the evolution of the vortex' phase. All the data confirm the plates are generating the expected vortices. Further investigation is needed to quantify the influence of manufacturing imperfections or misalignments on the plates performances.

Chapter 5

Summary, conclusions and future work

"If you torture the data enough, it will confess."
Ronald Coase

5.1 Summary

The work reported in this thesis represents the very first step in starting up a new branch of research within the Technology Group of the Jodrell Bank Centre for Astrophysics. Specifically, the aim was to begin to studying wave vortices at millimetre wavelengths and consequently adapt the known technologies to this frequency range. The logical steps of this process can be summarised as follows:

1. Review the relevant literature about OAM from a theoretical and experimental point of view,

2. Determine which theoretical description better fits our experimental conditions,

3. Determine which PMDs or methods for producing optical vortices within the existing ones can be more easily and efficiently adapted to millimetre wavelengths,

4. Write some IDL code to represent and visualise OAM mode through the L-G formulation,

5. Simulate the effects of devices such as q-plates or SPPs on a Gaussian beam,

6. Reproduce known results to check and confirm the correct functioning of the IDL code,

7. Use the already produced Nylon q-plate prototype to understand what the best testing procedure is and which experimental equipment is needed in order to perform it. The results are compared with a Finite Element Analysis simulation of the q-plate reproducing the experimental conditions,

8. Design new devices and have them manufactured, specifically SPPs,

9. Test the manufactured SPPs with procedures similar to those used for the q-plate as well as using a new near field 3D scanner implemented by a colleague Peter Schemmel [57],

10. Process the collected data to extract guide lines for future work.

In the present section the methods that have been used and the reason why they were chosen are summarised. What is reported here is my personal opinion and future work may or may not confirm these conclusions.

5.1.1 Mathematical representation

There are several sets of modes that can be used to describe light beams carrying OAM. These are usually sets of perpendicular polynomial modes with evident properties of symmetry: radial and azimuthal for L-G or Bessel modes or rectangular for the Hermite ones to name the most important. The most commonly used in the literature are the L-G modes as they naturally contain the $\exp(il\phi)$ phase term that gives rise to the spiral structure of the phase planes. These were used in this project. Not only do they well represent OAM modes but they also fit with our experimental conditions. The 3 mm wavelength Gaussian beams generated by the horn antennas we use satisfy the paraxial condition and the L-G modes are solutions to the paraxial wave equation.

Additionally, as the PMDs used were not pure mode converters, the output is not a pure OAM mode beam but a superposition of modes. After the interaction with a phase modulating plate the new mode coefficients need to be calculated to know the mode composition of the new beam and these modes can be propagated separately.

5.1.2 Simulations

Writing the IDL code to represent L-G modes, L-G mode superpositions, their interaction with the PMDs and to calculate the mode decomposition was vital for my understanding of the topic. It was useful for visualising the different modes and understanding the equations and their behaviour as well as for having the first predictions on how the output beam of an experiment would look like. This method is very fast but of course is not as accurate as a Finite Element Analysis can be. In cases where the expected output beam needs to be known in detail, for example to determine instrumental systematics, the latter approach is needed. As a first try the Ansys software for Finite Elements Analysis, HFSS, was used but it was later found that another software for EM simulation, FEKO, is actually of easier use and less demanding in terms of processing power and time. This software will be used for the beam-device interaction simulations concerning all the plates and the results will be published soon by the group together with the near-field measurements.

5.1.3 Experimental methods

Measurements on OAM beams generated using PMDs were performed in our RF lab for the first time. All the procedures and testing methods needed to be understood and put in place. Since we used two different kinds of plates, namely q-plates and SPPs, different experimental setups were used. The q-plate was the first to be put under test. The working principle of this device is more specific than that of a SPP as it involves circular polarisation of the input and output wave. That means it is necessary to involve QWRs in the experimental setup as explained in detail in the previous chapter. The q-plate is, in essence, a HWP with an azimuthally variable orientation of the birefringence optical axis. The first step is consequently to check the input RCP is turning into LCP after the interaction with the plate. This was

done by mounting on the source and receiver horns specifically oriented QWRs and performing beam cuts through the use of a rotary stage. Beam cuts were performed at various azimuthal angles to confirm the expected symmetry of the characteristic annular intensity pattern. Collected power measurements using a telescope setup were also performed to show the action of a q-plate and two identical q-plates combined. This was done to show that recollecting an OAM beam into a horn that supports almost only Gaussian modes brings an almost total loss of power. Most of the power is recollected when a second identical q-plate is inserted. A 2D scan at the output on a plane parallel to the q-plate was performed in the closest approximation of a plane wave attainable with the present experimental equipment. For the SPPs similar tests were performed on the mode |2| wedge spiral plate while all of the SPPs were then tested using the new near field scanner implemented by my colleague Peter Schemmel [57] which will take this work further testing new plates and comparing the data with FEKO simulations.

5.2 Results and conclusions

Summarising the experimental results, it can be said that the proper functioning of all the plates (q-plate and SPPs) has been demonstrated. The measurements on all the plates confirm the presence of the two characteristic features of a wave vortex: the symmetric ring-shaped transverse intensity pattern and the $l2\pi$ change of the phase around the beam's propagation axis, with l depending on the mode number the specific plate was designed for. In the case of the q-plate the expected change from LHCP to RHCP (or vice versa) was also confirmed as the plate locally acts as a HWP (Section 4.2). For all the plates a central minimum of the OAM beam of at least -20dB was obtained. This value could reach extremes of -30 to -40dB (all the values normalised to the maximum magnitude registered in each set of measurements) for measurements with the best alignment of the system. Knowing that the horn to horn and horn to plate alignment is so important for these kind of measurements I can say that with a very precise aligning procedure, that can now be put in place thanks to the improvement of our equipment, the central null of the vortex can be kept down to the noise level. It is also clear that in order to achieve high accuracy

in manufacturing the SPP's central part, it is preferable to have a smoothly and continuously varying surface (Section 4.3.6). All the measurements were performed at 100 GHz frequency as the plates were designed and optimised for it. However, a few beam cuts at different frequencies within the W-band were reported showing the diffractive effects of the SPPs step (Fig. 4.31). This effect, together with the slight shift of the deepest intensity minimum in figure 4.32 must be considered and further studied.

5.3 Current research activities

During the writing of this thesis further work on OAM research was carried out by colleagues in the Technology Group especially by colleague Peter Schemmel who is the first author of a study on a new SPP design reported in [59]. As a proof of concept, a modular stepped SPP was design, manufactured and tested at 100GHz. The modular SPP consists of ten separate sections that when put together create a mode |10| SPP. This design was developed to improve the precision of the plate's structure avoiding the manufacturing problems for the central point of the plate. The measurements performed with the 3D scanner system show the plate is generating the expected ring intensity pattern and phase profile. However the phase at the centre of the beam results to be largely distorted. These effects are currently under study.

5.4 Future work

Considering the early stages of our OAM research I consider these results to be very promising and I having set this base, in the future it will be possible to focus on more specific studies. I believe as a first approach it would be better to deeply study the most simple device and use it to reproduce real or toy experiments that simulate the conditions in which the plate will be used in reality (inserted in different test setups, in telecommunications systems or, eventually, on telescopes). If the goal is to understand the systematics, the efficiency, the purity, the sensitivity to displacements and misaligning and the leakage between modes I would personally avoid devices involving other degrees of freedom, like circular polarisation, unless strictly required

by the specific situation. This would also reduce the number of elements needed in the optical system as the QWRs could be avoided. Moreover it could be interesting to look for other techniques for producing plates with gradually varying refractive index in order to reduce the diffraction effects of the step. Another option could also be to look for materials and manufacturing methods that could improve the precision of the step sides specifically at the centre of the plate corresponding to the OAM beam singularity which was seen to be of fundamental importance. I think with the development of the 3D printing and the possibility of choosing between more and more materials this could be a way forward. Moreover, as the parameters that determine the geometry of the SPPs only depend on the frequency, it could be interesting to scale the SPPs to be optimal for frequencies other than 100 GHz which was the only one focused during this project. Finding a technique to make these devices broadband would also be useful and innovative.

References

[1] http://www.eccosorb.eu/technical-notes.

[2] http://www.hepcomotion.com/en/.

[3] A. F. Abouraddy, T. M. Yarnall, and B. E. A. Saleh. Angular and radial mode analyzer for optical beams. *Opt. Lett.*, 36(23):4683–4685, Dec 2011.

[4] M. N. Afsar. Precision millimeter-wave measurements of complex refractive index, complex dielectric permittivity, and loss tangent of common polymers. *IEEE transactions on instrumentation and measurement*, IM-36:530–536, 1987.

[5] L. Allen, M. W. Beijersbergen, R. J. C. Spreeuw, and J. P. Woerdman. Orbital angular momentum of light and the transformation of laguerre-gaussian laser modes. *Phys. Rev. A*, 45:8185–8189, Jun 1992.

[6] L. Allen and M. J. Padgett. The poynting vector in laguerre-gaussian beams and the interpretation of their angular momentum density. *Optics Communications*, 184(14):67 – 71, 2000.

[7] Ansys. Hfss, finite element method solver for electromagnetic structures.

[8] J. Arlt, K. Dholakia, L. Allen, and M. J. Padgett. The production of multiringed laguerregaussian modes by computer-generated holograms. *Journal of Modern Optics*, 45:1231, 1998.

[9] C. Barbieri, F. Tamburini, G. Anzolin, A. Bianchini, E. Mari, A. Sponselli, G. Umbriaco, M. Prasciolu, F. Romanato, and P. Villoresi. Light's orbital

angular momentum and optical vortices for astronomical coronagraphy from ground and space telescopes. *Earth, Moon, Planets*, 105:283–288, 2009.

[10] S. M. Barnett and L. Allen. Orbital angular momentum and non paraxial light beams. *Optics Communications*, 110:670–678, 1994.

[11] H. Bechmann-Pasquinucci and A. Peres. Quantum cryptography with 3-state systems. *Phys. Rev. Lett.*, 85:3313, 2000.

[12] H. Bechmann-Pasquinucci and W. Tittel. Quantum cryptography using larger alphabets. *Phys. Rev. A*, 61:062308, 2000.

[13] M. W. Beijersbergen, R. P. C. Coerwinkel, M. Kristensen, and J. P. Woerdman. Helical-wavefront laser beams produced with a spiral phase plate. *Optics Communications*, 112:321–327, 1994.

[14] M.W. Beijersbergen, L. Allen, H.E.L.O. van der Veen, and J.P. Woerdman. Astigmatic laser mode converters and transfer of orbital angular momentum. *Optics Comm.*, 96(13):123 – 132, 1993.

[15] R. A. Beth. Mechanical detection and measurement of the angular momentum of light. *Phys. Rev.*, 50:115–125, Jul 1936.

[16] M. Bourennane, A. Karlsson, and G. Bjork. Quantum key distribution using multilevel encoding. *Phys. Rev. A*, 64:012306, 2001.

[17] R. W. Bowman and M. J. Padgett. Optical trapping and binding. *Reports on Progress in Physics*, 76:026401, 2013.

[18] J. Courtial and K. OHolleran. Experiments with twisted light. *Eur. Phys. J. Special Topics*, 145:35, 2007.

[19] J. Courtial, D. A. Robertson, K. Dholakia, L. Allen, and M. J. Padgett. Rotational frequency shift of a light beam. *Phys. Rev. Lett.*

[20] J. E. Curtis and D. G. Grier. Structure of optical vortices. 2003.

[21] Inc. Exelis Visual Information Solutions. Idl version 8.2.2. (C) 2012.

[22] D. C. Flanders. Submicrometer periodicity gratings as artificial anisotropic dielectrics. *Appl. Phys. Lett.*, 42:492, 1983.

[23] S. Franke-Arnold, L. Allen, and M. Padgett. Advances in optical angular momentum. *Laser Photon. Rev.*, 2:299–313, 2008.

[24] I. Freund. Critical point explosions in two-dimensional wave fields. *Optics Comm.*, 159:99–117, 1999.

[25] G. Gibson, J. Courtial, M. J. Padgett, M. Vasnetsov, V. Pas'ko, S. M. Barnett, and S. Franke-Arnold. Free-space information transfer using light beams carrying orbital angular momentum. *Optics Exp.*, 12:5448–5456, 2004.

[26] M. Harris, C.A. Hill, and J.M. Vaughan. Optical helices and spiral interference fringes. *Optics Communications*, 106(46):161 – 166, 1994.

[27] M. Harwit. Photon orbital angular momentum in astrophysics. *The Astrophysical Journal*, 597:1266–1270, 2003.

[28] H. He, M. E. J. Friese, N. R. Heckenberg, and H. Rubinsztein-Dunlop. Direct observation of transfer of angular momentum to absorptive particles from a laser beam with a phase singularity. *Phys. Rev. Lett.*, 75:826–829, Jul 1995.

[29] N. R. Heckenberg, R. McDuff, C. P. Smith, and A. G. White. Generation of optical phase singularities by computer-generated holograms. *Optics Lett.*, 17:221–223, 1991.

[30] N.R. Heckenberg, R. McDuff, C.P. Smith, H. Rubinsztein-Dunlop, and M.J. Wegener. Laser beams with phase singularities. *Optical and Quantum Electronics*, 24(9):S951–S962, 1992.

[31] E. Karimi. Mode converter. *CC-BY-SA-3.0 (http://creativecommons.org/licenses/by-sa/3.0) via Wikimedia Commons.*

[32] A. Z. Khoury and P. Milman. Quantum teleportation in the spin-orbit variables of photon pairs. *Phys. Rev. A*, 83:060301, Jun 2011.

[33] Y. S. Kivshar. Optical vortices and vortex solitons. *Proc. SPIE*, 5508:16–31, 2004.

[34] P. Kurzynowski, M. Borwinska, and J. Masajada. Optical vortex sign determination using self-interference methods. *Optica Applicata*, XL:165–175, 2010.

[35] J. Leach, J. Courtial, K. Skeldon, S. M. Barnett, S. Franke-Arnold, and M. J. Padgett. Interferometric methods to measure orbital and spin, or the total angular momentum of a single photon. *Phys. Rev. Lett.*, 92:013601, Jan 2004.

[36] J. Leach, M. J. Padgett, S. M. Barnett, S. Franke-Arnold, and J. Courtial. Measuring the orbital angular momentum of a single photon. *Phys. Rev. Lett.*, 88:257901, Jun 2002.

[37] S. Maccalli, G. Pisano, S. Colafrancesco, B. Maffei, M. W. R. Ng, and M. Gray. q-plate for millimetre-wave orbital angular momentum manipulation. *Appl. Opt.*, 52(4):635, 2013.

[38] B. Maffei, E. Gleeson, J. A. Murphy, and G. PIsano. Study of corrugated winston horns. *Proc. SPIE 5498, Millimeter and Submillimeter Detectors for Astronomy II*, (812), 2004.

[39] A. Mair, A. Vaziri, G. Weihs, and A. Zeilinger. Entanglement of the orbital angular momentum states of photons. *Nature*, 412.

[40] E. Mari, F. Tamburini, G. A. Swartzlander, Jr., A. Bianchini, C. Barbieri, F. Romanato, and B. Thide. Sub-rayleigh optical vortex coronagraphy. *Optics Express*, 20:2445–2451, 2012.

[41] L. Marrucci, C. Manzo, and D. Paparo. Optical spin-to-orbital angular momentum conversion in inhomogeneous anisotropic media. *Phys. Rev. Lett.*, 96:163905, Apr 2006.

[42] M. Mirhosseini, M. Malik, Z. Shi, and R. W. Boyd. Efficient separation of the orbital angular momentum eigenstates of light. *Nat. Commun.*, 4, 2013.

[43] M. Mirhosseini, B. Rodenburg, M. Malik, and R. W. Boyd. Free-space communication through turbulence: a comparison of plane-wave and orbital-angular-momentum encodings. *Journal of Modern Optics*, 0(0):1–6, 0.

[44] G. Molina-Terriza, J. P. Torres, and L. Torner. Management of the angular momentum of light: Preparation of photons in multidimensional vector states of angular momentum. *Phys. Rev. Lett.*, 88:013601, 2001.

[45] G. Molina-Terriza, J. P. Torres, and L. Torner. Twisted photons. *Nature Phys.*, 3:305–310, 2007.

[46] G. Molina-Terriza, A. Vaziri, J. Rehacek, Z. Hradil, and A. Zeilinger. Triggered qutrits for quantum communication protocols. *Phys. Rev. Lett.*, 92:167903, 2004.

[47] E. Nagali, F. Sciarrino, and F. De Martini. Quantum information transfer from spin to orbital angular momentum of photons. *Phys. Rev. Lett.*, 103:013601, 2009.

[48] A. T. Neil and M. J. Padgett. Three-dimensional optical confinement of micron-sized metal particles and the decoupling of the spin and orbital angular momentum within an optical spanner. *Optics Communications*, 185(13):139 – 143, 2000.

[49] J. F. Nye and M. V. Berry. Dislocations in wave trains. *Proceedings of the Royal Society of London. Series A, Mathematical and Physical Sciences*, 336(1605):165–190, 1974.

[50] D. W. Oesch, D. J. Sanchez, and C. L. Matson. The aggregate behavior of branch points - measuring the number and velocity of atmospheric turbulence layers. *Reports on Progress in Physics*, 18:22377–22392, 2010.

[51] M. N. O'Sullivan, M. Mirhosseini, M. Malik, and R. W. Boyd. Near-perfect sorting of orbital angular momentum and angular position states of light. *Opt. Express*, 20(22):24444–24449, Oct 2012.

[52] M. Padgett, J. Courtial, and L. Allen. Light's orbital angular momentum. *Phys. Today*, 57:35–40, 2004.

[53] M. J. Padgett and L. Allen. The poynting vector in laguerre-gaussian laser modes. *Optics Communications*, 121:36 – 40, 1995.

[54] C. Paterson. Atmospheric turbulence and orbital angular momentum of single photons for optical communication. *Phys. Rev. Lett.*, 94:153901, 2005.

[55] B. Piccirillo and E. Santamato. Light angular momentum flux and forces in birefringent inhomogeneous media. *Phys. Rev. E*, 69:056613, 2004.

[56] D. J. Sanchez, D. W. Oesch, and Reynolds O. R. The creation of photonic orbital angular momentum in electromagnetic waves propagating through turbulence. *Astronomy Astrophysics*, 556:1–13, 2013.

[57] P. Schemmel, S. Maccalli, B. Maffei, F. Ozturk, G. Pisano, and M. W. Ng. A near field 3d scanner for millimetre wavelengths. *Conference Paper, Workshop on Antenna and Free Space RF Measurements, ESTEC, Noordwijk, The Netherlands*, 2013.

[58] P. Schemmel, S. Maccalli, G. Pisano, B. Maffei, and M. W. R. Ng. Three dimensional measurements of a millimetre wave orbital angular momentum vortex,. *Opt. Lett.*, 39(3):626, 2014.

[59] P. Schemmel, G. Pisano, and B. Maffei. Modular spiral phase plate design for orbital angular momentum generation at millimetre wavelengths. *Optics Express*, 22:14712–14726, 2014.

[60] N. B. Simpson, L. Allen, and M. J. Padgett. Optical tweezers and optical spanners with laguerregaussian modes. *Journal of Modern Optics*, 43(12):2485–2491, 1996.

[61] N. B. Simpson, K. Dholakia, L. Allen, and M. J. Padgett. Mechanical equivalence of spin and orbital angular momentum of light: an optical spanner. *Opt. Lett.*, 22(1):52–54, Jan 1997.

[62] S. Slussarenko, A. Murauski, T. Du, V. Chigrinov, L. Marrucci, and E. Santamato. Tunable liquid crystal q-plates with arbitrary topological charge. *Opt. Express*, 19(5):4085–4090, Feb 2011.

[63] Z. K. Su, F. Q. Wang, R. B. Jin, R. S. Liang, and S. H. Liu. A simple scheme for quantum networks based on orbital angular momentum states of photons. *Optics Communications*, 281(19):5063 – 5066, 2008.

[64] EM Software & Systems. Feko. Copyright 2000-2014.

[65] F. Tamburini, A. Sponselli, B. Thid, and J. T. Mendona. Photon orbital angular momentum and mass in a plasma vortex. *EPL*, 90:45001, 2010.

[66] F. Tamburini, B. Thide, G. Molina-Terriza, and G. Anzolin. Twisting of light around rotating black holes. *Nature Physics*, 7(3):195 – 197, 2011.

[67] B. Thidé, H. Then, J. Sjöholm, K. Palmer, J. Bergman, T. D. Carozzi, Ya. N. Istomin, N. H. Ibragimov, and R. Khamitova. Utilization of photon orbital angular momentum in the low-frequency radio domain. *Phys. Rev. Lett.*, 99:087701, Aug 2007.

[68] G. A. Turnbull, D. A. Robertson, G. M. Smith, L. Allen, and M. J. Padgett. The generation of free-space laguerre-gaussian modes at millimetre-wave frequencies by use of a spiral phase plate. *Optics Communications*, 127:183, 1996.

[69] A. Vaziri, J. W. Pan, T. Jennewein, G. Weihs, and A. Zeilinger. Concentration of higher dimensional entanglement: Qutrits of photon orbital angular momentum. *Phys. Rev. Lett.*, 91:227902, Nov 2003.

[70] H. Wei and X. Xue. *Quant-ph / 0208146*, 2002.

[71] H. Wei, X. Xue, J. Leach, M. J. Padgett, S. M. Barnett, S. Franke-Arnold, E. Yao, and J. Courtial. Simplified measurement of the orbital angular momentum of single photons. *Optics Communications*, 223(13):117 – 122, 2003.

[72] G. Whyte, J. Veitch, P. Ohberg, and J. Courtial. Vortex sorter for bose-einstein condensates. *Phys. Rev. A*, 70:011603, 2004.

IPSA SCIENTIA POTESTAS EST